Planetary Nebulae Associated with Galactic Star Clusters

Danilo González Díaz

A thesis presented for the degree of
Doctor en Física.

UNIVERSIDAD DE ANTIOQUIA
1 8 0 3

Instituto de Física
Universidad de Antioquia
Medellín

December 5, 2019

Planetary Nebulae Associated with Galactic Star Clusters

Danilo González Díaz

Abstract

Obtaining accurate distances to Galactic planetary nebulae (PNe) has proved to be a challenging task. Estimates of the uncertainties in the distances range on average between 30-50%. Association between PNe and stars clusters offers a reliable scenario to determine their fundamental parameters. Up to now, just four PNe have been associated to open clusters (OCs) and four more to Galactic globular cluster (GC). Confirmed associations enable parameters such as age, distance, internal reddening, physical size and progenitor mass of the PNe to be estimated. Furthermore, they allow theoretical models of the star evolution to be evaluated. In this work, we are interested in assessing potential association between five PNe and the same number of OCs, namely, the pairs PN/OC: Hen 2-133/Lynga 5 – Hf 69/Lynga 15 – Wray 17-31/Basel 20 – Wray 17-31, NGC 2899/IC 2488 and NGC 2452/NGC 2453. Intermediate-resolution spectra of 72 bright stars of the OCs were collected, as well as for each PN. In addition, new UBV, JHKs and G(BP-RP) photometry was extracted from VVV-2MASS and Gaia second data release (DR2), respectively. Spectra were used to determine radial velocity (RV) for both OC and PNe. If the RVs disagree, the membership is rejected. But, if they agree, other parameters as distance, reddening, and age need to be evaluated. Photometric and astrometric data were used to obtain new and more accurate cluster parameters. The most open clusters have been poorly studied, thus our first effort was directed to obtain their fundamental parameters. Eleven open clusters were finally studied, six of them lying in the complex vicinity of the OC Lynga 15, which is one of our target clusters. A constraint to the distance of $d > 7$ kpc for the remote cluster candidate LS 007 was obtained using VVV data. Moreover, the longstanding discrepancy in the distance of the OC NGC 2453 was resolved, as well as the real nature of the OCs Lynga 15, Loden 465, Loden 467, Bica 5 and Basel 20. The latter are not real clusters but probable field stars fluctuations. We finally conclude that the PNe NGC 2452, Hf 69, Hen 2-133 and Wray 17-31 are not members of the OCs NGC 2453, Lynga 15, Lynga 5 and Basel 20/IC 2488, respectively. In contrast, PN Hf 69 shares roughly the same parameters as OC Stock 14 but the youth of the cluster and the angular separation make membership unlikely. Finally, PN NGC 2899 seems to be a strong candidate for being a member of IC 2488 despite the large angular separation ($\sim 54'$).

Supervisors: Esteban Silva Villa and Christian Moni Bidin

Acknowledgements

First of all, I would like to express my sincere gratitude to my thesis supervisors A/Prof Esteban Silva Villa of the Instituto de Física, Universidad de Antioquia (UdeA), Colombia, and A/Prof Christian Moni Bidín of the Instituto de Astronomía, Universidad Católica del Norte (UCN), Chile. I am particularly grateful to Dr Christian Moni for his continuous encouragement, guidance and friendship over the time taken to complete this thesis, also for my first observational astronomy experience, the long conversations with a cup of coffee and his beautiful family. Thanks are also given to Dr Francesco Mauro of UCN for their valuable contributions in the management of VVV data, and both the A/prof Giovanni Carraro from Dipartimento di Fisica e Astronomia, Universitá di Padova and Dr Daniel Majaess from Mount Saint Vincent University, Canada, for their gentle advice.

This work was supported mainly by the call N^{o} 785 of 2017 of the colombian Departamento Administrativo de Ciencia, Tecnología e Innovación, COLCIENCIAS and operated by COLFUTURO. I thank all the staff of the University of Antioquia who facilitated communication with Colciencias and the management of resources, as well as to the postgraduate director A/Prof Juan Carlos Muñoz for his help in the different administrative issues. I also extend my thanks to Plataforma de Movilidad studiantil y Académica of Alianza del Pacífico and its chilean headquarters in the Agencia Chilena de Cooperación Internacional para el Desarrollo - AGCID, for supporting my first internship at the UCN. I thank all the staff of the UCN for hosting me during the two internship periods, and Natalia Peréz Hernandez for helping us develop this and other inter-institutional projects.

This work has made use of data from the European Space Agency (ESA) mission Gaia (https://www.cosmos.esa.int/gaia), processed by the Gaia Data Processing and Analysis Consortium (DPAC, `https://www.cosmos.esa.int/web/gaia/dpac/consortium`); data from the HASH PN database at hashpn.space (`http:`

//202.189.117.101:8999/gpne/index.php); data from the Two Micron All Sky Survey, which is a joint project of the University of Massachusetts and the Infrared Processing and Analysis Center/California Institute of Technology, funded by the National Aeronautics and Space Administration and the National Science Foundation; data collected at the 2.5 m du Pont telescope located at Las Campanas Observatory, Chile (program ID CHILE-2013A-157); and the SIMBAD and Vizier databases, operated at the CDS, Strasbourg, France.

I must thank Natalia Castro also for her advice on English corrections; she made this dissertation more presentable.

Finally I leave my biggest and most special thanks to both my mother and my girlfriend Luisa, for their unwavering encouragement and support throughout the four years I spent completing this work. I would like to dedicate this thesis to my mother, who despite adversities and her humble origin, always supported me unconditionally in my studies even if she did not understand very well what they were about.

Contents

Declaration

The work in this thesis is based on research carried out at the Instituto de Física, Universidad de Antioquia, Colombia. No part of this thesis has been submitted elsewhere for any other degree or qualification, and it is the sole work of the author unless referenced to the contrary in the text.

Some of the work presented in this thesis has been published in journals and conference proceedings - the relevant publications are listed below.

Publications

González-Díaz, D., Bidin, C. M., Silva-Villa, E., Carraro, G., Majaess, D., Moitinho, A., ... & Morales-Campaña, E. (2019). Solving the distance discrepancy for the open cluster NGC 2453-The planetary nebula NGC 2452 is not a cluster member. Astronomy & Astrophysics, 626, A10.

List of Figures

List of Tables

Acronyms

AGB asymptotic giant branch

CMD color-magnitude diagram

CC cross-correlated

CCF cross-correlation function

DR2 second data release

DSS2 second data release of the Digital Sky Survey

E-AGB early AGB

FOV field of view

GC globular cluster

HB horizontal branch

HBB hot bottom burning

HR Hertzsprung-Russell

HST Hubble space telescope

MLM most likely member

MS main sequence

OCs open clusters

PNe planetary nebulae

PPN preplanetary nebulae

RDPs Radial density profiles

RGB red giant branch

RV radial velocity

TCD Two-color diagram

TP-AGB thermal-pulse asymptotic giant branch

WD white dwarf

Chapter 1

Introduction

Obtaining accurate distances to Galactic planetary nebulae PNe has proved to be a troublesome task. This has perhaps been the major difficulty in the study of these objects in our Galaxy. Zhang (1995a) estimated the uncertainties in the distances ranging on average between 30-50%, while Giammanco et al. (2011) confirmed this results finding uncertainties in about 35% via the IPHAS extinction distances for PNe along with existing estimates. Our knowledge about intrinsic properties of the PNe in the Galaxy depends on the reliable measures in the distance. Indeed, properties such as the luminosity, age, physical size and mass of the central star can only be determined with high accuracy if the distances are well calibrated. Many calibrators have been used thus far, being the most reliable the ones whose distances can be measured from trigonometric parallaxes (Harris et al., 2007; Smith Jr, 2015; Chornay and Walton, 2020b; Chornay et al., 2021), spectroscopic parallaxes (Ciardullo et al., 1999), extragalactic membership (Stanghellini et al., 2008; Bhattacharya et al., 2019) and cluster membership(Majaess et al., 2007; Parker et al., 2011; Moni Bidin et al., 2014). PNe are thought to be one of the last stages in the life of stars of about 1-8 solar masses ($M_{\odot}$). These fascinating objects consist of two interacting parts: a shell of gas of different shapes, which is the origin of the various morphologies of the PNe, and a white dwarf central star, which has expelled the gas shell during the late stages of its evolution. The central star is a really hot star of small diameter, radiating mainly in the ultraviolet spectrum, exciting the gas which reemits most of the energy through a number of highly excited emission lines. Because the gas and dust form the diffuse nebular part, accurate identification of the center stars is not always possible, so in addition to their low luminosities, parallax estimates are only available for a few and close PNe (Kimeswenger and Barría, 2018; Benedict et al., 2009). Moreover, the masses and compositions of the progenitor stars for most of those PNe are unknown; at best, they have been hardly inferred via statistical methods of the underlying stel-

lar population (Badenes et al., 2015). In contrast, association between PNe and stars clusters offer a reliable scenario to determine their fundamental properties. Distances for well studied open cluster (OCs) can be established with uncertainties lower than 10% (Turner and Burke, 2002; Majaess et al., 2012b; Chené et al., 2012). Once the membership is proved, the PNe inherit some properties of the cluster, such as age, distance, reddening and cluster kinematic. But other parameters can also be deduced, such as luminosity, physical size, kinematical age, and a constraint for the mass and metallicity of the progenitor stars through the turn-off of the main sequence (MS) and metal content, respectively. Besides, PNe being members of star clusters can be used as distance calibrators for statistical methods (Stanghellini et al., 2008; Frew et al., 2016). No wonder astronomers strive to find such associations. Unfortunately, most of the pairs PNe/OCs end up being just coincidences in the line of sight. Majaess et al. (2007) discussed the possible cluster membership of thirteen PNe that are located in close proximity to open clusters lying in their lines of sight. Seven out of thirteen cases considered are likely line-of-sight coincidences, but there were six cases where the evidence suggested the possibility that the PNe belonged to a star cluster. Seventeen more cases where the membership may be suspected were listed in Majaess et al. (2007, in their Table 5). Frew (2008) and Frew et al. (2016) roughly studied the membership of 38 potential associations in order to calibrate his statistical distance indicator. Just two of them were used as calibrators. Moni Bidin et al. (2014) assessed four pairs of PNe/OCs from the list of Majaess et al., using RVs in order to reject or confirm the associations. The authors concluded that two out of the four pairs were just coincidences, one pair was a true association and the fourth one could be associated but the results were not conclusive. Table 1.1 summarizes the potential associations and the state between PNe and star cluster drawn for literature. Most of them were listed by Frew (2008), who compiled previous lists from Kohoutek (2001); Majaess et al. (2007); Bonatto et al. (2008). We have added two poorly studied PNe lying in the line of sight of OC IC 2488 whose membership is unknown, and one interesting extragalactic PN likely associated to a cluster in M31 galaxy (Davis et al., 2019). Only four pairs seem to be really associated, that is, the PHR 1315-6555/ESO 96-4, BMP J1613-5406/NGC 6067, NGC 2818 /NGC 2818 and He 2-86/NGC 4463. Four well known additional PNe in globular cluster have been added, namely, Ps 1/NGC 7078 (M15), GJJC 1 (IRAS 18333)/NGC 6531 (M22), JaFu 1/Pal 6, and JaFu 2/NGC 6441.

Many of the open clusters in Table 1.1 have been poorly studied or their parameters disputed. In this work, we are interested in studying the potential association between five PNe and five OCs that have been proposed in literature. We have acquired new photometry and spectrocopy data in order to compute accurate fundamental parameters to OCs and to assess PNe membership using Radial Velo-

cities. The pairs PN/OC are: Hen 2-133 / Lynga 5, Hf 69 / Lynga 15, Wray 17-31 / Basel 20, Wray 17-31 - NGC 2899 / IC 2488, and NGC 2452 / NGC 2453 (highlighted lines in Table 1.1).

1.1 From MS to PN

Planetary Nebulae is one of the last stages in the stars evolution of low and intermediate mass ($0.8\,M_\odot$-$8\,M_\odot$). More massive stars are thought to evolve as Type II supernovae. The path of formation of a planetary nebula begins when the hydrogen-burning starts to stop in the core of the main-sequence stars. The core begins to contract by effect of the gravity, while a hydrogen-burning shell is formed around the core. The outer layers expand, the star's effective temperature decreases and its luminosity increases. The star is moving to a redder and more luminous part of the Hertzsprung-Russell (HR) diagram occupying the red giant branch (RGB). As result of the expansion of the star and the subsequent decrease of the effective temperature, the hydrogen opacity increases and a convective zone is developed in the star's interior. As the star rises through the RGB, the convection zone deepens up to reach the nuclear burning zone. In this zone, the chemical abundances ratios of the various species in the CNO cycle have been altered by nuclear processes and the mass fraction of $^3_2$He has increased. So when the convective zone dips into this chemically modified region, the material is mixed and carried to the outer layers. The convection drags $^{14}_{7}$N upwards and at the same time pulls $^{12}_{6}$C inwards, modifying the composition of the photosphere. This process is know as first *dredge-up*.

When a star with masses $<2M_\odot$ climbs up to the red giant tip, the He core has contracted so much that the central temperature and density allows the triple alpha process. The He core is electron-degenerated, thus the energy released in the process increases the temperature, but cannot expand the core. This increases the helium-burning rate, which in turn increases the temperature, until ending up with a thermonuclear runaway. The energy released is enormous and the core reaches a luminosity of $10^{11}L_\odot$. This is termed as Helium Core Flash. However, the process takes a very short time. Most of the energy released is absorbed by the layer of the envelope and it does not reach the surface, although it can cause mass loss. The energy released by the flash removes the core degeneracy. After that the core can expand, decreasing the temperature and allowing a steady He burning. The star decreases its luminosity rapidly, moving to bluer zones in the HR diagram, in the so called horizontal branch (HB). The Helium Core Flash does not happen in stars with masses $>2M_\odot$. Instead, the star begins to ignite helium gradually.

Table 1.1: Possible associations and coincidences between Planetary-Nebula/Star-Cluster. (Taken from Majaess et al. 2007; Moni Bidin et al. 2014; Jacoby et al. 1997; Frew et al. 2016; Davis et al. 2019). P=Probable association, C=Membership confirmed, R=Rule out association, U=Unknown.

Planetary Nebula	PN Identifier	Open Cluster	Membership
A 69	G076.3+01.1	Anon (Turner)	P
Bl 2-1	G104.1+01.0	NGC 7261	P
FP0739-2709	G242.3-02.4	ESO 493-03	P
Hf 4	G283.9-01.8	van den Bergh-Hagen 91	P
Hf 69	**G324.8-01.1**	**Lynga 15**	**P**
Hen 2-133	G324.8-01.1	Lynga 5	P
K 3-57	G072.1+00.1	Berkeley 51	P
K4 4-41	G068.7+01.9	NGC 6846	P
KLW 6	G070.9+02.4	Berkeley 49	P
M 1-80	G107.7-02.2	Berkeley 57	P
NeVe 3-1	G275.9-01.0	NGC 2925	P
NGC 2452	**G243.3-01.0**	**NGC 2453**	**P**
NGC 2899	**G277.1-03.8**	**IC 2488**	**P**
Pe 2-4	G275.5-01.3	van den Bergh-Hagen 72	P
		NGC 2910	P
PHR 0840-3801	G258.4+02.3	Ruprecht 66	P
PHR 0905-5548	G274.8-05.7	ESO 165-09	P
PHR 1429-6043	G314.6-00.1	NGC 5617	P
Sa 2-4	G 225.1-01.9	Berkeley 76	P
Wray-17-31	**G277.7-03.5**	**IC 2488**	**P**
		Basel 20	**P**
PHR J0930-5716	G278.3-04.3	IC 2488	U
WRAY 16-49	G278.5-04.5	IC 2488	U
A66 9	G172.1+00.8	NGC 1912 (M38)	R
ESO 177-10	G324.8-01.1	Lynga 5	R
HeFa 1	G329.5-02.2	NGC 6067	R
KoRe 1	G327.7-05.4	NGC 6087	R
M 3-20	G002.1-02.2	Trumpler 31	R
M 3-45	G359.7-01.8	Basel 5	R
NGC 2438	G231.8+04.1	NGC 2437 (M46)	R
NGC 6741	G033.8-02.6	Berkeley 81	R
Sa 2-167	G347.7+02.0	NGC 6281	R
VBe 3	G326.1-01.9	NGC 5999	R
BMP J1613-5406	G329.8-02.1	NGC 6067	C
He 2-86	G300.7-02.0	NGC 4463	C
NGC 2818	G261.9+08.5	NGC 2818	C
PHR 1315-6555	G305.3-03.1	ESO 96-4	C
GJJC 1	G009.8-07.5	NGC 6656 (M22)	C
JaFu 1	G002.1+01.7	Pal 6	C
JaFu 2	G353.5-05.0	NGC 6441	C
Ps 1	G065.0-27.3	NGC 7078 (M15)	C
M31 B477-1	—	B477-D075 (in M31)	P

This stage of helium-burning is similar to the stage of hydrogen-burning in the main-sequence phase but much shorter (≈200Myr for a star of $2M_\odot$). When the helium-burning core is exhausted, the core composed mainly by oxygen and carbon begins to contract, yielding an expansion and cooling of the star's envelope. In this stage, some stars suffer structural instabilities in the outer layers, represented as periodic variations in the luminosity, temperature and radial velocities. RR-Lyrae variables are example of this type of stars.

Because the CO core is contracting, the inner temperature increases and a thick shell of helium-burning is formed around it. The star has now two energy sources (the other one being the hydrogen-burning shell formed during earlier stages). The envelope again increases in luminosity and cools, moving the star to more redward and more luminosity zones in the HR diagram along the asymptotic giant branch (AGB). For stars with masses $>4M_\odot$, in the middle of the two layers of burning material, an intershell zone is formed. This intershell zone is rich in He and N (produced by the conversion of carbon and oxygen into nitrogen). Because the effective temperature is decreasing, the convective zone deepens again. When the convective zone dips into the intershell, helium and nitrogen emerge to the envelope. This process is known as the second dredge up. This dredge up happens in the early AGB (E-AGB) stage.

The hydrogen-burning shell is yet active and throws down helium, which is added to helium layers. The mass of this layer increases and becomes a former thin layer slightly degenerated. As the He core contracts, it becomes hotter and denser. The temperature increases via triple alpha process, without expanding the helium layer due to the degeneration state, until a helium flash occurs in the shell. This shell's helium flash is however much less energetic than the one occurred in the core of less massive stars in the RGB stage. The flash causes the hydrogen shell to expand and cool, eliminating the state of degeneration, and consequently turn off. The helium shell eventually will exhaust its fuel, the hydrogen shell will contract and reignite, repeating the process again. This is translated as periodic variations ($\sim 10^5$ years) in the luminosity at the surface. This stage is called the thermal-pulse asymptotic giant branch (TP-AGB). If the star is massive enough ($\sim$2-4$M_\odot$), the convective zone after each flash event can penetrate to deeper parts of the helium burning shell where the carbon is being synthesized and dredge the material into the photosphere (third dredge-up), making the star carbon-rich. For higher masses ($\sim$4-8$M_\odot$) the lower regions at the convective envelope are exposed to such high temperatures that the CNO can be processed in the so called hot bottom burning (HBB). The C is converted to N, and this causes the ratio C/O to decrease, making the star oxygen-rich and increasing the nitrogen in the outer layers. These stars are the

precursors of the Type-I PNe*.

The late AGB phase is known for the high mass-loss rates, which can reach up to $10^{-4}\,M_\odot\,yr^{-1}$ Delfosse et al. (1997). This implies that, if the rate of mass loss were constant, in just 10000 yr, an AGB star could lose a tremendous amount of mass (the *superwind*). The mechanism that drives the mass-loss is still under study. Some authors propose that when the pulsations in the AGB phase happens, brings material farther for the star, where dust can form, and radiation pressure on the grain will then push them away, carrying with them the gas (Kwok, 2007b; Decin, 2021). In fact, oxygen-rich stars tend to form silicates, while the carbon-rich ones form graphite grains. The gas and dust are thrown into the interstellar medium and they are the source of the maser emissions OH/infrared (OH depicts the emission of hydroxyl molecules) (Zijlstra et al., 1989; Cohen et al., 2005). Those envelopes are the precursors of the preplanetary nebulae (PPN)†, which are strong sources of infrared radiation, acting as reflection nebulae. These objects have not yet been ionized by the strong radiation from the star's exposed core.

The gas and dust envelope continues to expand until the central star is exposed. During this phase, the star moves through the bluer zones in the HR diagram keeping almost the same luminosity. When the mass loss rate of the star drops to about $10^{-8}\,M_\odot\,yr^{-1}$, a rapid wind reaching up to $2000\,km\,s^{-1}$ sweeps the envelope blown off in the superwind phase (velocities in the superwind are about $20\,km\,s^{-1}$) (Iben Jr, 1995; Wachter et al., 2002), exposing the hot core of the post-AGB star. Temperature of the central star, a white dwarf (WD), reaches $\sim 30000\,K$, so the radiation emitted (mainly ultraviolet) begins to ionize the resulting circumstellar gas distribution. Emission lines of H and N, as well as forbidden lines of [OIII], [OII] and [NeIII] are commonly observed. This is the PN phase.

PNe display a wide variety of shapes, and they have been classified in morphological groups by several authors: round, elliptical, bipolar (butterfly), stellar, irregular, quadrupolar, among others (Curtis, 1918; Greig, 1971; Stanghellini et al., 1993; Manchado et al., 1996), being most of them not spherical. This has open a wide discussion about the loss of symmetry in the envelope expansion in AGB stars. García-Segura et al. (1999) and García-Segura et al. (2005) attribute the formation of those shapes to effects of the stellar rotation and magnetic field driving out the mass-loss in the post AGB stars. The authors claim that during the thermal pulses, stars with masses $>1.3\,M_\odot$ transport angular momentum from the core

*Type-I PNe are considered as those whose progenitor are massive enough to the C to N conversion has occurred in the surface of the star via the dredge-up (Kingsburgh and Barlow, 1994). Peimbert (1978) classified the Type-I PNe as having He/H≥0.125 and log(N/O)≥-0.3, while Kaler et al. (1990) used He/H≥0.15 and log(N/O)≥-0.1.

†another widely used term to refer to these objects in literature is protoplanetary nebulae

to the envelope increasing the rotation in the superwind phase at the tip of the AGB. This mechanism can form bipolar PNe. On the other hand, magnetic fields can increase their energy from the stellar rotation, which in turn causes a rapid spin-down in the core of the evolved star, and can produce a short and powerful outburst able to drive out the stellar wind. Stronger fields can produce jets, while weaker fields account for elliptical nebulae. However, these models are not shared by the whole community. As an example, Soker (2006) and Nordhaus et al. (2007) argue that the magnetic field in single AGB stars takes the angular moment of the star in short time scales, affecting the magnetic field itself until mitigating it. In contrast, a binary companion, even a sub-stellar one, could be the source of the angular momentum able to shape espherical PNe. This is called the Binary Hypothesis, contrary to the former known as Single Star Paradigm (For a wide discussion, see for example De Marco, 2009; Jones and Boffin, 2017; Boffin and Jones, 2019). Thus, the majority of PNe may be the outcome of binary interaction and not the single star scenario. PNe found in globular clusters seem to agree with the binary origin. In fact, globular clusters present turnoff mass smaller than $0.55M_{\odot}$. For such lower masses, the post AGB stars are unable to ionize the oxygen and hydrogen because it would take a longer time than the dispersion time of the envelope, making it undetectable (Schönberner, 1983; Kalirai et al., 2009). Scenarios with stellar mergers, binary mass transfer and post-common envelope primary (McCrea, 1964; Sandquist et al., 1998; Ciardullo et al., 2005; Passy et al., 2011b) could be the mechanism of PNe formation in GC.

1.2 The number of PNe in a cluster

PNe in star clusters have shown to be a rare phenomenon. Just four PNe have been found to be members of Galactic OCs, and the same number for Galactic GCs. It is expected that ∼96% of Galactic stars in the main sequence will evolve to WDs, of which only 40% will go through their PNe stage first (Kwok, 2007b; Schönberner and Drilling, 1985). The remaining will not be massive enough ($<0.5M_{\odot}$) to climb the AGB track, and therefore will evolve to WD from the horizontal branch or they will not be able to ionize the nebula before the expanding gas is dispersed in the interstellar medium. One parameter that plays an important role in establishing the potential association with star clusters is the lifetime of the PNe. The lifetime of the PNe depends heavily on the initial mass of the progenitor star and the mass-loss in the AGB stage, and it is estimated between 10^3 to 10^5 yr (Schönberner and Blöcker, 1996; Köppen and Acker, 2000). Majaess et al. (2007) showed that the age of the nearby Galactic open clusters present a normal distribution with a peak

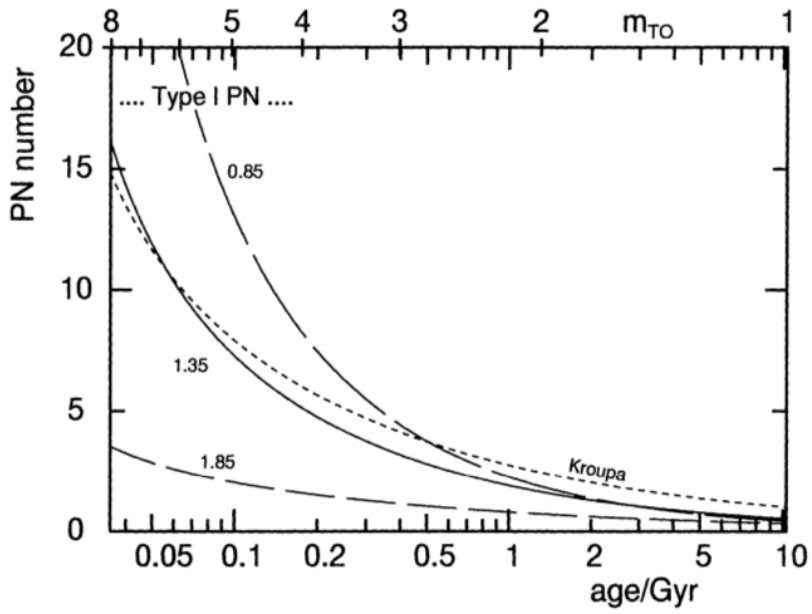

Figure 1.1: Number of PNe expected as a function of the cluster age, extracted from Köppen and Acker (2000). The PNe lifetime has been set at 100 kyr, and the total mass of the clusters at $10^6\,M_\odot$. The curves depict several IMFs.

in 100 Myr, corresponding to a turnoff mass of $4\,M_\odot$. For such progenitor mass, the lifetime of a PNe formed in the cluster is $\sim 10^3$ yr. This is virtually a blink in a lifetime of the cluster.

Köppen and Acker (2000) computed the expected number of the PNe present in clusters of $10^6 M_\odot$ as a function of the age. The results are shown in Fig. 1.1. The lifetime of the PNe was generously assumed to be 10^5yr. The figure was built using power-law initial mass function (IMF) with different slopes (0.85, 1.35, 1.85) as well as the Kroupa's IMF (Kroupa, 1995). In general terms, younger clusters will host more PNe than older ones with the same mass, even by a factor of 10. For lifetimes of 10^4yr (10% of the previous value), the number of PNe expected in clusters of 50 Myr with $10^6\,M_\odot$ will be of 1 PN per cluster, and this number drops up to 0.1 PNe per cluster of 1Gyr (Köppen and Acker, 2000). The number of PNe scales directly with the cluster mass. Masses of the OCs can have values of $10^4\,M_\odot$ or less, i.e, two orders of magnitude less than previous estimates. This imply that the number of PNe expected in OCs is $<<1$ PNe per cluster of 50 Myr.

1.3 How to establish potential associations

Majaess et al. (2007) defined a series of criteria in order to qualitatively assess the physical associations. We summarize the criteria in Table 1.2. The first criterion to

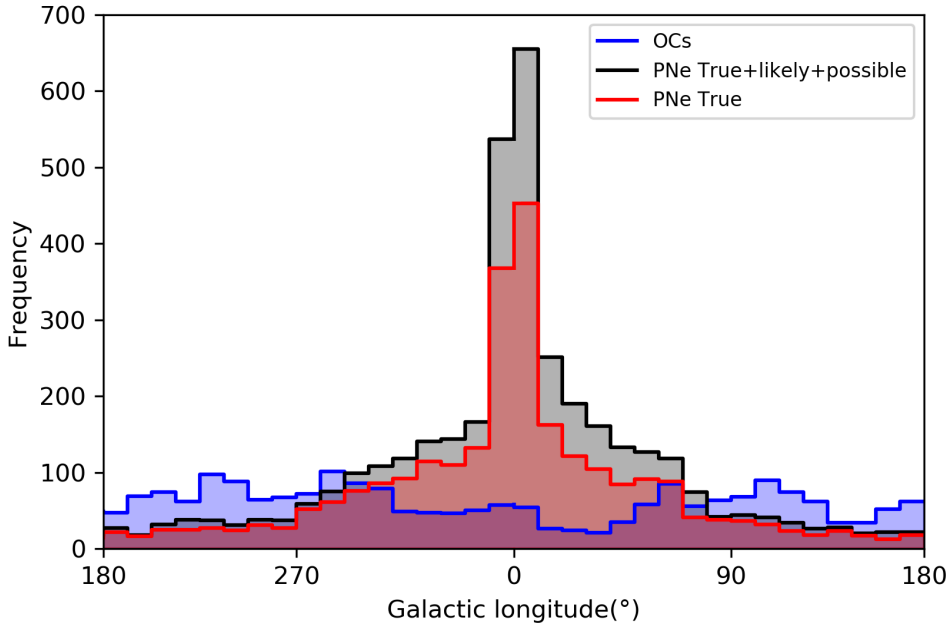

Figure 1.2: Distribution of the PNe and OCs with respect to the Galactic longitude. Bins run on steps of 10°. Gray zone represents the number of PNe with status of True + likely + possible as defined in HASH PN database, red zone the number of true PNe, while the blue one depicts the number of OCs. Updated figure from Majaess et al. (2007).

suspect potential PNe/star-clusters associations is the spatial proximity. However, taking into account only the criterion of angular distance can be weak because, as was said before, the object could be projected in the same line of sight, yet completely uncorrelated. This is especially true in dense fields as can happen in the Galactic disk or the bulge. Fig. 1.2 shows that the number of PNe (both true and potential) increases towards the Galactic bulge, and decreases towards the towards the Galactic anti-center (i.e., towards l=180^o). The figure is an update of Figure 1 in Majaess et al. (2007). PNe data were obtained from HASH: the Hong Kong/AAO/Strasbourg Hα planetary nebula database * (Parker et al., 2016), which includes a wide compilation of previous catalogues, as well as photometric and spectroscopic data. OCs data was drawn from Dias et al. (2002, updated to 2015)†. PNe that are bulge members have served to calibrate old statistical distance scales due to the fact that they are supposed to lie all in the same distance to the Galactic bulge. At about ±90° in the galactic plane, the number of PNe lies below the number of OCs, reducing the number of coincidences. In fact, the four PNe associated to OCs have been found in Galactic longitudes among 260°-330°.

*http://202.189.117.101:8999/gpne/dbMainPage.php
†Catalog B/ocl on Vizier database

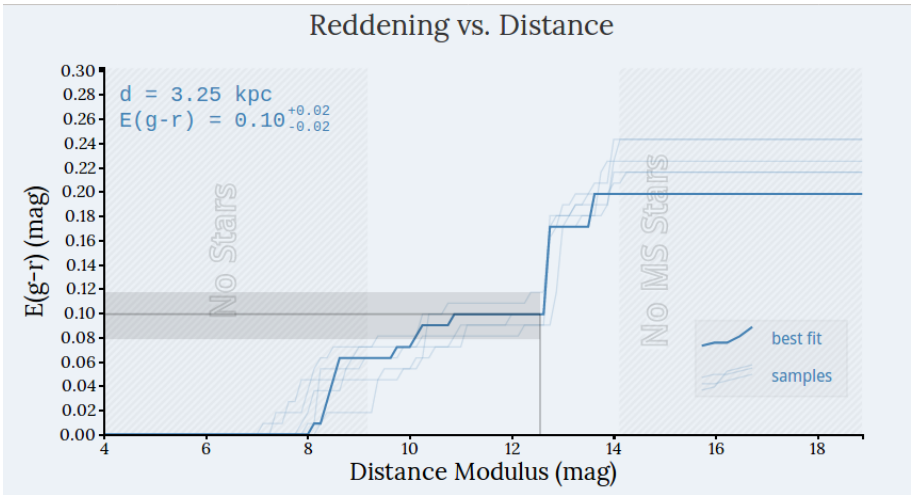

Figure 1.3: Distance reddening relationship along the line of sight l=235.322218°, b=+3.774190°. The plot shows the reddening E(g-r) as a function of distance modulus. The map is based on Pan-STARRS 1 and 2MASS photometry, as well as the parallaxes from Gaia. A value for the distance, d, is given in kpc for a reddening value in the line of sight in the region in which stars were observed. The relation conversion is E(B-V) = 0.981 E(g-r). The continuous blue line show the best fit (Taken from 3D Dust Mapping Green et al. 2018).

On the other hand, real size of the open cluster is diffuse. Relatively large angular separations do not mean rejecting the association immediately. The radii for OCs are often defined as the radius in which the star density varies as the star field density (r_{clu} in Table 1.2). Stars attached to cluster, having same proper motions and distances (Kholopov, 1969; Danilov et al., 2014), can be extended far beyond of the obvious star concentrations, in the so called cluster corona (r_{cor}), which can extend between 2.5 to 3 cluster radii, but it can reach up to 10 for richer clusters (Kholopov, 1969). Besides, Turner and Pedreros (1985) Majaess et al. (2008), Turner (1977) and Usenko et al. (2019), among others, showed that an important fraction of short-period Cepheids fall within the corona of the host cluster. That kind of Cepheids are potential progenitors of PNe. Crowded fields need more precise methods and measurements.

RVs and reddening are also required. If the pair PN/star-cluster are associated, the heliocentric radial velocity and reddening should be similar. RVs are actually one of the strongest criteria to support or reject associations, and they are always required. Indeed, RVs and proper motions. In contrast, reddening can be more discussed. Dust is not distributed uniformly in the Galactic plane or on the same line of sight as has been shown by Neckel and Klare (1980), Schlegel et al. (1998) and more recently by Meisner and Finkbeiner (2013), Green et al. (2014). Thus, stars with very different distances located in some lines of sight over the Galactic plane could present similar reddening. Fig. 1.3 shows how the reddening varies

Table 1.2: Criteria established by Majaess et al. (2007) to evaluate PNe/OCs association.

Criterion	**Likely member**	**potential member**	**Non-member**
Separation (arcmin)	$\leq r_{clu}$	r_{clu}-r_{cor}	$\geq r_{cor}$
$\Delta RV(km\,s^{-1})$	$\leq$5	5-10	$\geq$10
$\Delta E(B-V)$	$\leq$0.2	0.2-0.6	$\geq$0.6
D_{PN}/D_{clu}	$\sim$1	1-2	$\geq$2
Log(τ)	—	—	$<$7.4

with the distance in the Galactic direction l=235.322218°, b=+3.774190°. Plot was obtained from the 3D Dust Mapping with PanSTARRS 1, 2MASS and Gaia* (Green et al., 2018). Stars located in the horizontal shaded line are sharing the same reddening of E(g-r)≈0.1, but the corresponding distance is ranging between 1.5-3.3 kpc. In addition, PNe could present high internal reddening in comparison with their vicinity. An interesting discussion is presented by Moni Bidin et al. (2014) between the PNe He 2-86 and the OC NGC 4463 where, despite the similarities between the other parameters, the difference in reddening was $\Delta E(B-V) \approx 0.9$.

Fouth line in Table 1.2 depicts the ratio of the estimated distances of both objects. The previously commented uncertainties in the determination of the distances for PNe and also the discrepancies presented in literature for some OCs (see Chapter 4) make this criterion weak on its own.

Finally, although the age of the cluster is not a strong criterion for supporting membership, it is for rejecting it. Younger clusters with ages < 30 Myr ($\log(\tau) \approx 7.4$ dex) are thought to be housing stars which will probably end up as Type-II supernovae rather than PNe. Clusters with these ages are expected to present main-sequence turnoff masses $\sim 8\,M_\odot$. OCs with ages of about 100 Myr ($\log(\tau) \approx 8$ dex, turnoff mass of $\approx 4\,M_\odot$) are the most probable clusters to housing PNe (Majaess et al., 2007).

1.4 The true PNe/SCs associations

Table 1.1 shows four PNe classified as OC members. Two of them have shown to be undeniable members, compatible in most of its parameters with the cluster. The remaining two are compatible in their strongest criteria, but they present some inconsistencies, anyway justifiable. Additionally, four PNe have been found to belong to GC. Despite that, the number of the PNe in GC is lower than expected (Jacoby et al., 1997, 2017). Four more candidates have been proposed by Minniti et al.

*http://argonaut.skymaps.info/

(2019). If that was not enough, another four have been reported in extragalactic star clusters. Henceforth, the association will be discussed.

1.4.1 PHR 1315-6555 / ESO 96-4

PN PHR 1315-6555 was the first PNe physically associated to an OC, namely, ESO 96-4 (also known as Andrews-Lindsay 1). The PN was discovered as part of the Macquarie/AAO/Strasbourg Hα planetary nebula project (MASH), and first reported by Frew (2008) as a strong candidate to cluster membership. PHR 1315-6555 lies just $23''$ from the center of the cluster, which has a radius containing half the cluster members of $\sim 1.5'$ (Cantat-Gaudin et al., 2018a). Parker et al. (2011) obtained distance, heliocentric radial velocity and reddening for the PN of $\mathrm{d} = 10.5 \pm 3.4\,\mathrm{kpc}$, $\mathrm{HRV} = 58 \pm 2.5\,\mathrm{km\,s^{-1}}$ and $\mathrm{E(B\text{-}V)} = 0.83 \pm 0.08$, respectively. Distance was estimated from statistical Hα surface brightness-radius (SB-r) relation (Frew, 2008). In comparison, the author estimated the same set of parameters for the cluster in $\mathrm{d} = 10.4 \pm 1.8\,\mathrm{kpc}$, $\mathrm{HRV} = 57 \pm 5\,\mathrm{km\,s^{-1}}$ and $\mathrm{E(B\text{-}V)} = 0.72 \pm 0.02$. Those results mean differences of $\sim 1\,\mathrm{km\,s^{-1}}$ in the mean values of the RVs, 0.11 in reddening and a ratio of ~ 1 in the distances, besides the PN is located within the cluster radius, and the age of the cluster was estimated in 800 Myr ($\log(\tau) \approx 8.9$ dex). PHR 1315-6555 is a Type-I PN. Progenitors for this kind of PNe are thought to be high mass stars. Indeed, the turn-off mass for the cluster is $\sim 2.5\,\mathrm{M_\odot}$, in good agreement with what was expected.

However, Kharchenko et al. (2013) reported systematically lower values for the distance ($\sim$7.3 kpc), RV ($40\,\mathrm{km\,s^{-1}}$) and E(B-V) (0.625). One year later, the parameters of the cluster were refined by Majaess et al. (2014), who obtained a more accurate distance of $\mathrm{d} = 10.0 \pm 0.4\,\mathrm{kpc}$. The distance this established has been claimed by the authors as one of the most precise for a Galactic PN ($\sim 4\%$). On the other hand, Cantat-Gaudin et al. (2018a) reported a parallaxe of 0.045 mas for the cluster, equivalent to a distance of $\sim$13,5 kpc. Such long distances derived from GAIA are often accompanied by large uncertainties.

1.4.2 BMP J1613-5406 / NGC 6067

BMP J1613-5406 is a low-surface-brightness, bipolar PN listed in the HASH PN Catalogue, identified as elliptical with internal structure noted. BMP J1613-5406 is located $\sim 7'$ from the center of the cluster, and its diameter is estimated at $14''$ (Dias et al., 2002). The tidal radius of the cluster was averaged in $\approx 15'$ (Fragkou et al., 2019), that is, the PN lies within the cluster boundary. NGC 6067 is also known

to host another PN, namely, HeFa 1, which was suspected to be associated to the cluster, but the association was rejected by Moni Bidin et al. (2014) due to the discrepancy in their RVs (ΔRV$\approx$100 km s^{-1}). The cluster weighted average distance, reddening and RV have been established from literature in d = 1.88$\pm$0.10 kpc, E(B-V) = 0.35 $\pm$ 0.03, and HRV = -39.79 $\pm$ 0.57 km s^{-1} (Alonso-Santiago et al., 2017; Kharchenko et al., 2013; Piskunov et al., 2008). Besides, the cluster seems to be younger with an age of 90 $\pm$ 20 Myr (log(τ) $\approx$ 7.9 dex)) (Alonso-Santiago et al., 2017). Fragkou et al. (2019) found good agreement with the values for BMP J1613-5406. In fact, the authors obtained d = $1.71^{+0.29}_{-0.24}$ kpc, E(B-V) = 0.38 $\pm$ 1.1, and HRV = - 39.93 $\pm$ 1.44 km s^{-1}. PN distance was estimated using the Hα SB-r relation statistical method (Frew et al., 2016). Parameters for both objects are in excellent agreement, but the perfect match in RVs (ΔRV $<$ 1) suggest that BMP J1613-5406 is a physical member of NGC 6067. BMP J1613-5406 is a possible Type-I PN, which indicates a massive progenitor. The main-sequence turn-off mass for the cluster is expected to be of $\sim$5M$_{\odot}$. This agrees with the morphology of the PN. Fragkou et al. claim that the progenitor star mass of the PN BMP J1613-5406 approaches the theoretical lower limit of core-collapse supernova formation.

1.4.3 NGC 2818 / NGC 2818

The potential association of this pair PN/OC, which share the same name, has been heavily disputed in literature. For many years, the pair was thought to be a real association based on their proximity ($\sim$1.4$'$, with the cluster radius containing half the members of $\sim$6.7$'$), in early measures of distance (d$_{clu}$ = 2300 pc, d$_{pn}$ = 2660 $\pm$ 830 pc), reddening (E(B-V)$_{clu}$ = 0.18, E(B-V)$_{pn}$ = 0.28 $\pm$ 0.15) and RVs (RV$_{clu}$ = 3 $\pm$ 20 km s^{-1}, RV$_{pn}$ = 8 $\pm$ 13 km s^{-1}) (Pedreros, 1989; Zhang, 1995b; Tylenda et al., 1992; Tifft et al., 1972). RV for the cluster was estimated using two A-type stars. However, a more accurate velocity of 20.69 $\pm$ 0.29 km s^{-1} was later obtained by Mermilliod et al. (2001) from 12 red giant stars in the cluster, while Durand et al. (1998) and Meatheringham et al. (1988) obtained -0.9 $\pm$ 2.9 km s^{-1} and -1 $\pm$ 3 km s^{-1} for the planetary, respectively. The clear discrepancy in the RVs was strong enough to rule out the membership, suggesting only a line of sight coincidence. The discussion did not end there. Vázquez (2012) carried out a detailed study on the complex kinematics of the PN via high-resolution spectroscopy. The authors estimated a very different radial velocity of RV = 26 $\pm$ 2 km s^{-1}, and they claim that the previous determinations of the systemic velocity of PN NGC 2818 have been affected by low-resolution spectra. The latter result is in good agreement with the RV found by Mermilliod et al. for the cluster, and the membership was suspected again. Nevertheless, Vázquez resisted using the membership with

the OC as distance estimator for the PN, contrasting with Frew et al. (2016), who used the PN as calibrator of their statistical H_α SB-r relation, using the association, and adopting the distance found by Mermilliod et al. for the cluster (3 kpc) as the PN distance.

1.4.4 He 2-86 / NGC 4463

Potential association between the PN He 2-86 and the OC NGC 4463 was suspected by Majaess et al. (2007) due to the spatial separation of about 6′, and the angular radius of the cluster of $\sim 3.5'$ (Sampedro et al., 2017). Moni Bidin et al. (2014) measured RVs for both objects finding an important similarity within the 0.9σ in the measures of -15 ± 2 km s^{-1} for the cluster against -11 ± 4 km s^{-1} for the PN, suggesting a potential membership. The authors carried out a meticulous analysis of the cluster parameters, which until then had been very uncertain. They found a cluster distance of d=1.55 ± 0.10 kpc. In contrast, distances estimation for the PN have been really uncertain. They span a very wide range, from 1.3 to 5.1 kpc. On the other hand, the reddening to the PN of E(B-V) = 1.3-1.5, is much greater than the cluster value of E(B-V) = 0.42, suggesting the former is a background object but, as the authors claim, all the measurements of the RV to the PN in addition to RV-distance model for the Galactic rotation (Brand and Blitz, 1993) controvert this fact. Moni Bidin et al. (2014) conclude that He 2-86 is a real member of NGC 4463, but the PN is highly internally obscured.

1.4.5 PNe in Galactic globular clusters

Although the existence of PNe in globular clusters (GCs) was not expected, four pairs PNe/GCs are currently known (see Table 1.1). PS 1 (also know as K 648) was first discovered by Pease (1928), who also proposed the membership to the GC NGC 7078 (M15) based on both the proximity to the center of the cluster and their RVs. The membership was confirmed in later works (see, for example, Buell et al., 1997; Alves et al., 2000; Bianchi et al., 2001). A second association was established by Gillett et al. (1986) and Cohen and Gillett (1989) between the extremely H depleted (that is, it does not show evidence of Balmer lines in emission) PN GJJC 1, and the GC NGC 6656 (M22). Later, Jacoby et al. (1997) detected two additional PNe belonging to GCs through an extensive survey of about 133 GC, namely, JaFu 1 in Palomar 6 and JaFu 2 in NGC 6441. PN JaFu 1 is located far from the center of the GC Palomar 6, in $\sim 4'$, although still within the tidal radius. RVs of 176±15 km s^{-1} for the PN are in rough agreement with the cluster's, estimated in 200±20 km s^{-1} (Minniti, 1995). However, more recent works obtained the RV of

Table 1.3: New pairs PNe/GC candidates from Minniti et al. (2019) and Minniti, Dante et al. (2021).

PN ID	Cluster	Angular distance (arcmin)
PN SB 2	Minni 06	2.8
PN G354.9-02.8	Minni 11	2.4
PN G356.8-03.6	Minni 28	0.7
PN Pe 2-11	Minni 31	1.8
PN PHR J1806-1956	VVV-CL160	4.6
PN PM 1-209	VVV-CL160	4.9

cluster in an average of $178\pm3\,\mathrm{km\,s^{-1}}$ (Eadie and Harris, 2016; Baumgardt et al., 2019; Vásquez et al., 2018) in excellent agreement with the PN, making membership more likely. In contrast, the pair JaFu 2 / NGC 6441 presented a velocity difference of $21\pm5\,\mathrm{km\,s^{-1}}$. This result seems to rule out membership, but on the contrary, it is very consistent with the velocity dispersion of the cluster of $18\,\mathrm{km\,s^{-1}}$ (Jacoby et al., 1997). These associations pose a great challenge to understand the mechanisms that allow the formation of PNe in GCs. The stellar evolution models of single stars are not compatible with GCs hosting PNe. The lower mass limit for stars forming PNe should be in the range 1-1.5 $\mathrm{M_\odot}$ (Schönberner, 1983; Kwok, 2007b). Ages for GCs imply that the stars evolving to white dwarfs today should be $\approx0.55\,\mathrm{M_\odot}$ (Schönberner, 1983). The core of these low mass stars is unable to ionize the oxygen and hydrogen shells before the gas ends up dispersing, making them virtually undetectable. Mechanisms to explain the PNe formation in GC have been discussed for several authors, from reviewing post-AGB time scales in which low-mass single stars are able to form PNe, passing by blue straggler stars as progenitors, to mass transfer through binarity (Jacoby et al., 1997; Bertolami, 2016; Ciardullo et al., 2005; McCrea, 1964; Passy et al., 2011a). Binary systems as progenitors of PNe is not a new topic (De Marco, 2009, 2006; Soker, 2006; Zijlstra, 2007); indeed, the great majority (over 80%) of PNe present complex morphologies which have resulted hard to explain from single stars, and a binary companion is required, possibly even a substellar one, in most of the cases (Douchin et al., 2015; Hillwig et al., 2016; Barker et al., 2018). This is an important issue to take into account for the PNe associated to open clusters, because the main sequence turn-off of the single stars are often used to constraint the progenitor mass.

Finally, Minniti et al. (2019) and Minniti, Dante et al. (2021) proposed six additional PNe candidates to belong to GC from VVV data. The candidates can be consulted in Table 1.3. This is an open topic, and future works will establish the final membership.

1.4.6 Planetary Nebulae in extragalactic star clusters

As has been shown in previous sections, associations between PNe and star clusters in our Galaxy has turned out to be a complex work. So finding PNe associated to extragalactic cluster seems like an impossible work. Nevertheless, some examples have been reported in literature. Based on spectroscopy with the Magellan I Baade 6.5 m telescope at Las Campanas Observatory, Minniti and Rejkuba (2002) discovered the first PN belonging to an extragalactic GC, namely, the NGC 5128 (Centarus A galaxy) globular cluster G169. The authors claimed the membership due to the emission lines in [OIII]λ5007,λ4959 emerging superposed on the continuum of the GC G169, along with the RV measured for the PNe of $\sim$702 km s^{-1} against the RV for the cluster $\sim$697 km s^{-1} from Sharples (1988). This PN showed a spectrum corresponding to a typical high-excitation PN with an apparent magnitude of 24.3 in [OIII]λ5007 line. On the other hand, Larsen and Richtler (2006) found three likely PNe candidates associated with younger extragalactic cluster (>30 Myr). The authors intend to assess stellar population models in several nearby galaxies. However, they noted [OIII] and [NeII] emission lines in the spectra, due to more likely PNe rather than HII region, which are common in star-forming galaxies. Based on the RVs agreement, two of them were associated to the cluster 487 and 254 in NGC 5236 (M83), and they are considered stronger candidates for belonging to an extragalactic young cluster, while the third one is unlikely a member of the cluster 1106 of NGC 3621 because the RV differs in $\sim$150 km s^{-1}.

Bond (2015) used narrow-band [O III] filters from the Hubble Space Telescope to study star clusters throughout the Local Group. The author identified the PN called M31 B477-1 lying 1$''$.2 from the center of the known B477-D075 open cluster. This PN had previously been identified as HII region by Veyette et al. (2014). More recently, Davis et al. (2019) measured the RV of the PN, finding the same value as that of the cluster in good agreement within the errors bar ($\sim$10 km s^{-1}), and computed a probability of superposition $\leq$2% between the OC and the PN. Through isochrone fitting, the authors estimated an initial mass of $\sim$3.38 M$_{\odot}$ for the PN. Because the PN seems to be a Type-I PN, the authors claim this association could test stellar evolution models according to which the hot-bottom burning is expected to occur in progenitors with masses grater than $\sim$4M$_{\odot}$.

Chapter 2

Introducing the potential associations

The position on the Galaxy of the set of PNe and OCs studied in this work is shown in Fig. 2.1, superposed to Aladin DSS2 color image. The clusters extend over the third and fourth Galactic quadrant, from $l \sim 240°$ to $l \sim 325°$, covering southeast part of Norma and Centaurus, along with the south of the Vela and the Carina OB association. The equatorial and the galactic coordinates of the OCs are listed in Table 2.1, ordered by decreasing right ascension α. Equatorial coordinates are referred to J2000.0 equinox. All clusters are found in the Galactic disks, with

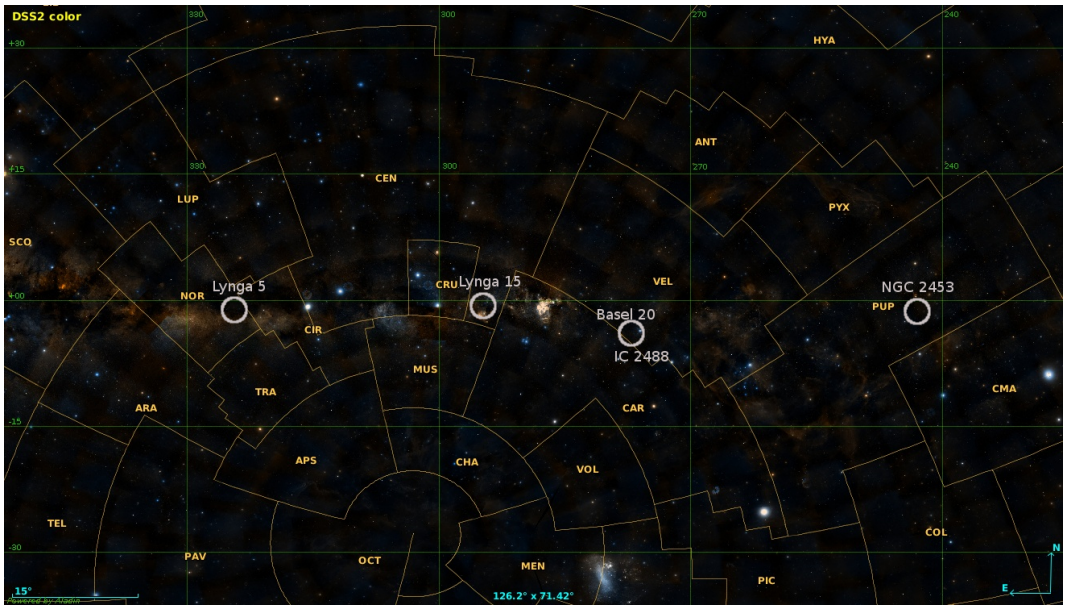

Figure 2.1: Aladin DSS2 color image showing the positions of the clusters studied here (white circles). The Galactic coordinates l and b are depicted as a green grid, and constellation limits are plotted as yellow lines.

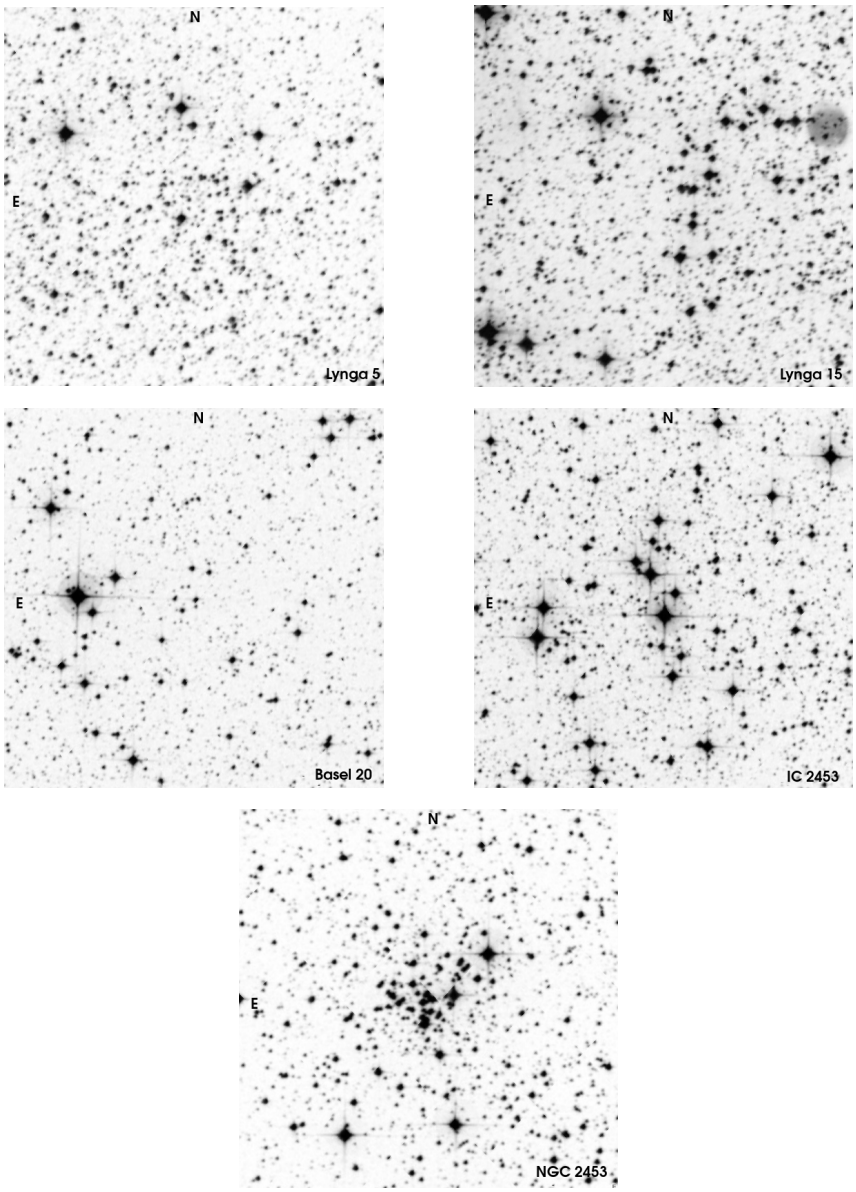

Figure 2.2: $10' \times 10'$ extracts from DSS2 data around the center of the clusters surveyed here. The cluster name as well as the north and east directions are shown.

Table 2.1: OCs coordinates

Cluster name	α_{2000} hh:mm:ss	δ_{2000} dd:mm:ss	l Degree	b Degree
Lynga 5	15:41:54.0	-56:39:00	324.7897	-01.1938
Lynga 15	11:42:14.4	-62:30:36	295.0419	-00.7030
Basel 20	09:30:59.5	-56:25:48	277.7711	-03.6886
IC 2488	09:27:38.0	-57:00:00	277.8298	-04.4192
NGC 2453	07:47:36.7	-27:11:35	243.2766	-00.9332

Basel 20 and IC 2488 showing the largest Galactic latitude. Extracts from each individual cluster within a field of view (FOV) of $10' \times 10'$ can be seen in Fig. 2.2. Most of them have been poorly studied and their nature is unknown. RGB color images for the PNe were extracted from HASH PN database* in order to describe their morphology, and they are shown in Fig. 2.3. Besides, each group PN/OC is suspected to be associated, so Fig. 2.4 shows the relative position of the PNe with respect to the OCs.

2.1 The pair NGC 2452/NGC 2453

The PN/OC pair NGC 2452 / NGC 2453 is located in the third Galactic quadrant ($180° \leq\ l\ \leq 270°$). Over the last few decades, an effort to better understand the galactic structure in this sector has been made (Carraro et al., 2005; Moitinho et al., 2006; Vazquez et al., 2008). Even so, this quadrant has not been fully examined yet. Fig. 2.2 shows a set of well defined clustered bright stars. This pair has been widely studied, and the membership of the PN to the stellar cluster heavily contested. An agreement in the literature about the measurements of both distance and age of the cluster ($\alpha_{2000} = 07^h47^m36^s.7$, $\delta_{2000} = -27°11'35''$) has not been reached. The early photometric study and MS fit of 21 cluster stars by Moffat and Fitzgerald (1974, hereafter MF) established a distance of $d \sim 2.9$ kpc and an age of $\tau \sim 40$ Myr. Other studies agreed to some extent, proposing cluster distances in the range of d ≈2.4-3.3 kpc (Glushkova et al., 1997; Hasan et al., 2008), while Gathier et al. (1986) obtained almost twice that value (5.0±0.6 kpc) via Walraven photometry on five stars previously reported as members by MF. Later, Mallik et al. (1995) revealed a deeper MS of the cluster by means of BVI photometry. These latter authors determined a distance of about $d \approx 5.9$ kpc, with a mean age of $\tau \approx 25$ Myr, but they also showed that the best fit depended on which stars were considered cluster members. In fact, the line of sight to the PN/OC pair is highly contaminated by field stars belonging to the Puppis OB associations and the Perseus arm (Peton-Jonas, 1981; Majaess et al., 2007). This complex mix of different stellar populations in the color-magnitude diagram (CMD) inevitably adds uncertainty to the results of an isochrone fit, which could be easily affected by field stars.

NGC 2452 (also identified as WRAY 15-85, V* V354 Pup, Hen 2-4, ESO 493-11) is a highly excited, elliptic PN, whose diameter reaches 18.3 arcsec, and it is defined as Emps in HASH database (see Fig. 2.3). In Fig. 2.5 it is possible to see an images of the Hubble space telescope (HST) of the PN showing a complex internal structure as well as the central star. NGC 2452 ($\alpha_{2000} = 07^h47^m26^s.26$, $\delta_{2000} =$

*http://202.189.117.101:8999/gpne/

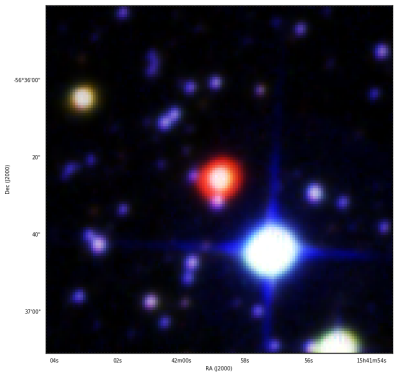

Hen 2-133

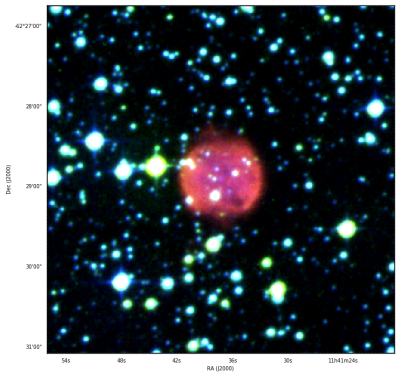

Hf 69

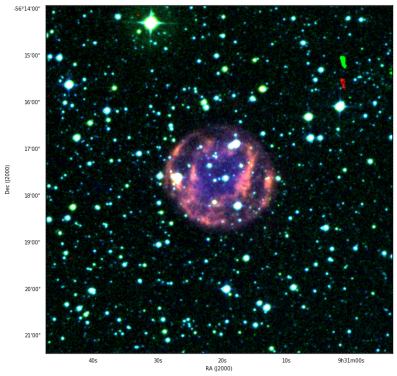

WRAY 17-31

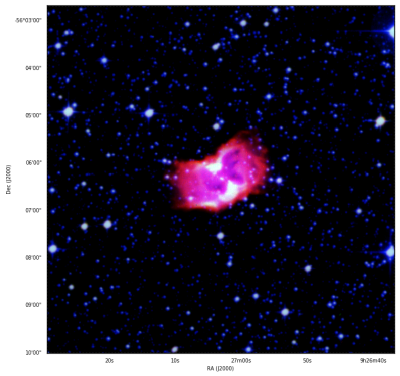

NGC 2899

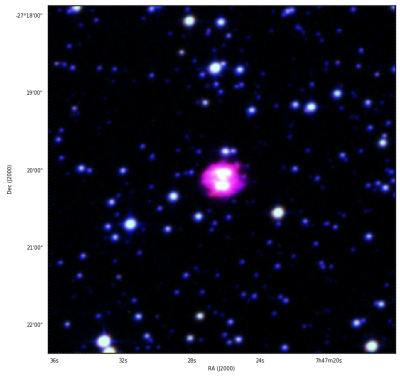

NGC 2452

Figure 2.3: SHS images from HASH PN database for the PNe studied in this work. Images are a composition of three color rgb in the bands Hα/SR/BJ.

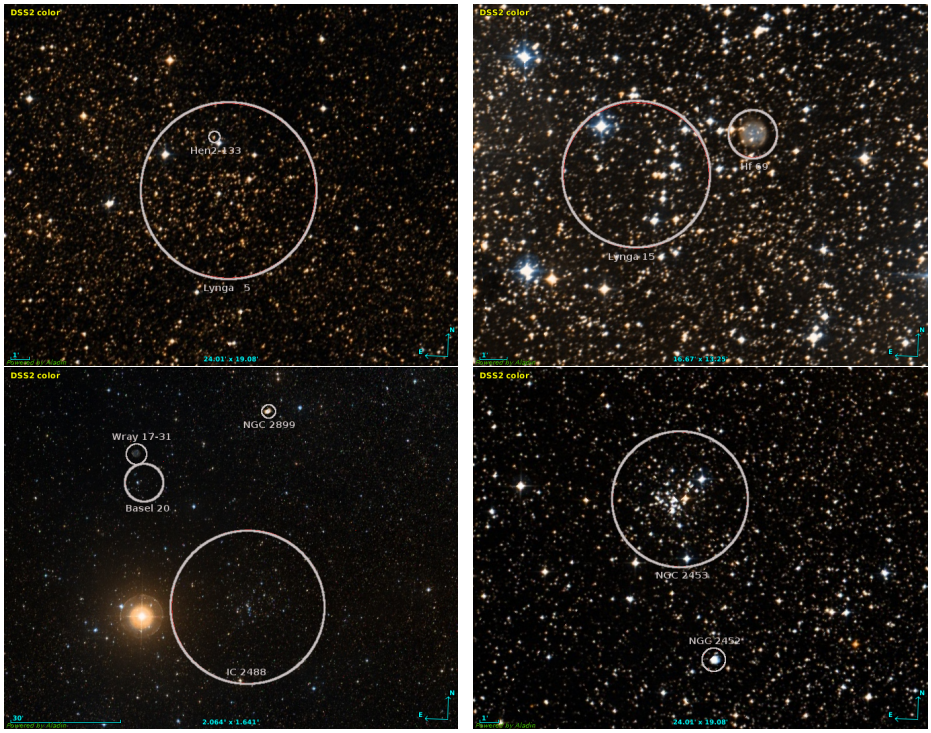

Figure 2.4: Aladin DSS2 color image showing the relative location of the pairs PNe/OCs (white circles) studied in this work. *Top-left:* Hen 2-133/Lynga 5. *Top-right:* Hf 69/Lynga 15, *Bottom-left:* WRAY 17-31,NGC 2899/IC 2488,Basel 20, *Bottom-right:* NGC 2452/NGC 2453.

$-27°20'06''.83$) is a massive PN (Cazetta and Maciel, 2000), whose progenitor must have been an intermediate-mass MS star close to the upper limit allowed for PN formation. This is consistent with the $\sim$ 40 Myr age of NGC 2453 proposed by MF and Moitinho et al. (2006), which implies a turnoff mass of $\approx$7 $M_{\odot}$. The cluster age is an important parameter to discard membership to young OCs (sec. 1.3) because evolved stars in clusters younger than $\sim$30 Myr are thought to end as type-II supernovae rather than forming a PN (see Majaess et al., 2007; Moni Bidin et al., 2014, hereafter MB14). Distance estimates for this PN can also be found in the literature, from 1.41 kpc, passing through 2.84 kpc, to 3.57 kpc (Khromov, 1979; Stanghellini et al., 2008; Gathier et al., 1986, respectively, among others). The value obtained by Gathier et al. (1986) ($d = 3.57 \pm 0.5$ kpc) from a reddening-distances diagram was very different from the cluster value derived from zero-age MS (ZAMS) fitting in the CMD and two-color diagram (TCD), $\sim$5 kpc. However, their estimate of the PN reddening ($E(B-V) = 0.43 \pm 0.5$) roughly matched the literature value for the cluster, which is in the range $\sim$0.47-0.49 (Moffat and Fitzgerald, 1974; Gathier et al., 1986; Mallik et al., 1995).

The association between NGC 2453 and NGC 2452 has been proposed and studied

by many authors, in light of their angular proximity in the sky (angular separation $\sim 8'.5$, see Fig. 2.4 and Table 2.2) and the data available (see, e.g., MF, Gathier et al. 1986, Mallik et al. 1995, MB14). Nevertheless, the results have not been conclusive. Moffat and Fitzgerald (1974) found coincidences between the RV of the PN measured by Campbell and Moore (1918), who measured 68 km s^{-1}, and that of an evolved blue giant star in the cluster (67±4 km s^{-1}). Subsequent measurements yielded consistent RVs for the PN in the range ∼62-68 km s^{-1} (Meatheringham et al., 1988; Wilson, 1953; Durand et al., 1998). Even so, Majaess et al. (2007) advocated additional observations needed to evaluate potential membership. MB14 recently studied the RV of ten stars in the cluster area, supporting the cluster membership of NGC 2452. However, they claimed that their result was not definitive, because the identification of cluster stars was problematic.

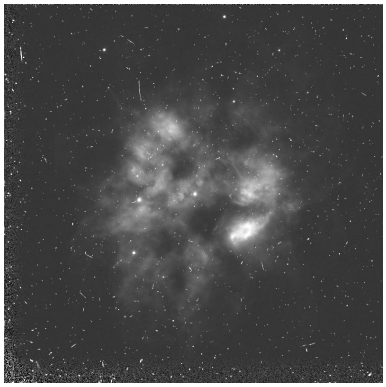

Figure 2.5: PN NGC 2452 from MAST, taken with the WFPC2/PC in filter F555W (Proposal ID: 6119).

2.2 The pair Hf 69/Lynga 15

Lynga 15 is an OC located in the Centaurus constellation about 1° northeast from the HII region IC 2494 and 11′ west from the dark nebula SDC G295.185-0.578. (see Fig. 2.1). Accurate location of the cluster center has been elusive. Kharchenko et al. (2013) and Joshi et al. (2016) placed the cluster at α_{J2000}=$11^h42^m14.4^s$ and δ_{J2000}=−62°30′36″, as reported on Simbad database*, while Sampedro et al. (2017) and Dias, W. S. et al. (2014) placed the cluster about 2 arcmin farther away as it is reported on Webda database†. This discrepancy could be not that important, except because in about 5 arcmin lies the PN Hf 69 (see Fig. 2.4). Fig. 2.2 does not show a handful of stars joined together, but an sparse set of bright stars with the PN visible northwest of the FOV.

*http://simbad.u-strasbg.fr/simbad/sim-fbasic
†https://webda.physics.muni.cz/navigation.html

Kharchenko et al. (2013) reported an angular radius for Lynga 15 of $r = 7'.5$, with an average age logarithm of $\log(\tau) = 7.4$ dex and a distance of $d = 1380$ pc. In contrast, Sampedro et al. (2017) found a closer and older cluster with parameters of $d = 932$ pc and $\log(\tau) = 8.43$ dex, while Dias, W. S. et al. (2014) found a smaller cluster with $r = 5'$. The age estimated by Kharchenko is in the limit of the OCs to form PNe (Majaess et al., 2007), while the distance by Sampedro is too close to be associated with Hf 69, whose distance was estimated at $d = 1.73 \pm 0.52$ kpc by Frew et al. (2016) using the Hα SB-r relation. The planetary is a poorly studied object, classified as an elliptic PN in HASH database (Emps), presenting multiple shells and internal structure (see Fig. 2.3). PN extends to a diameter of 65 arcsec, but our 2D spectrum reveals an ionized halo spread over at least a diameter of 3.5 arcmin around Hf 69. The most intense feature correspond to [OIII]λ 5007 line, while the opposite feature is [OII]λ 3727 line. Two bright stellar spectra crosses the inner zone of the PN, and one more the field outer (bottom continuum spectrum). It can be seen how emission lines extend along the entire spatial axis beyond the PN envelope in the features [OIII]λ 5007, [OIII]λ 4959, H_β, H_γ, H_δ and [OII]λ 3727. Halos around PNe are not rare at all, on the contrary, elliptic PN often are found to have spherical halos. This interesting topic is beyond the scope of this work. A complete description about this phenomenon can be reviewed in Kwok (2007a); Frew (2008).

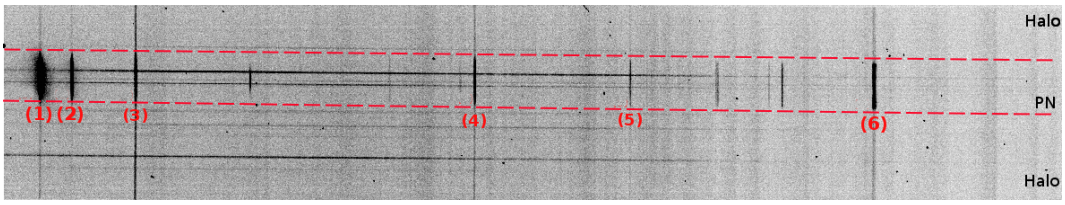

Figure 2.6: Raw 2D spectrum for Hf 69. Slit cover a field of ~ 3.5 arcmin, with a wavelength range 3750-5000 Å. Dashed red lines depict the PN boundaries and the beginning of the halo. (1): [OIII]λ 5007, (2): [OIII]λ 4959, (3): H_β, (4): H_γ, (5): H_δ and (6): [OII]λ 3727.

Recently, Perren et al. (2020) analyzed Lynga 15 using deep UBVI photometry and Gaia DR2. The authors claim Lynga 15 is not a real cluster but a field of stars contaminated by blue stars along the line of sight. Added to these contradictory results, the field of $12'$ around Lynga 15 seems to host four more open clusters, and one more $20'$ around it (see Fig. 5.1). OCs in the neighborhood are Bica 5, Loden 463, Loden 465, Loden 467 and Stock 14. The former lies only $3'.4$ from Hf 69, while the latter is the most prominent, younger cluster of them, whose logarithm of the average age is reported in the literature between 6.8 and 7.3 dex (Kharchenko et al., 2016; Sampedro et al., 2017). Loden 467 has the largest angular distance

from the PN, while Loden 463 and Loden 465 have been poorly studied, and their parameters are still uncertain.

In order to untangle the complex neighborhood of the OC Lynga 15, along with estimating the OCs parameters and assess potential membership with PN Hf 69, we used both the Gaia second data release (DR2) (Arenou et al., 2018b) and the VISTA Variables in the Vía Láctea (VVV) data. Gaia DR2 has shown to be very useful in determining astrometric parameters selecting stars in clusters over the field via proper motions and parallaxes with great precision (Cantat-Gaudin et al., 2018a; Dias et al., 2018; Bossini et al., 2019; Liu and Pang, 2019). Nonetheless, distance estimates for distant objects or regions with high interstellar absorption from Gaia parallaxes have shown to be problematic (Perren et al., 2020). Fields around Lynga 15 present high differential reddening, especially near to Stock 14. JHKs photometry from VVV has shown marked improvement in the reduction of uncertainties of the distances for open clusters (Majaess et al., 2012a). Besides, differential reddening in VVV photometry are less harmful than in the optical. By joining together the most likely cluster members obtained from Gaia DR2 and the deeper main sequences from VVV, we aim to obtain precise determination of the photometric parameters of the known clusters and investigate the nature of those that have still been little studied. In particular, we aim to assess the potential associations between those clusters with the PN Hf 69.

2.3 The pair Hen 2-133/Lynga 5

Lynga 5 is an OC placed at the Norma constellation in the Galaxy plane with optical coordinates $\alpha_{J2000} = 15^h41^m54.0^s$ and $\delta_{J2000} = -56°39'00''$ (Kharchenko et al., 2013) (see Fig. 2.1). Fig. 2.2 shows a crowded field of faint stars with some notable bright-stars, potentially members of the cluster. Majaess et al. (2007) suspected the possible pair association due to the angular proximity along with the similar distance and reddening between the cluster and the PN Hen 2-133 (also known as WRAY 15-1341,Sa 3-31, ESO 177-10). In fact, The PN lies just 2.6 arcsec from the cluster center (Table 2.2), i.e., in the inner zone of the OC, as can be seen in Fig.2.4. This poorly studied, compact star-like PN appears classified as an elliptic (E) PN in HASH catalog. Fig. 2.3 shows an unresolved structure of 1.8 arcsec, although in the images from HST it is possible to see more complex internal structures with an identifiable bright central star (see Fig. 2.7).

Preliminary isochrone fitting for the cluster by Majaess et al. (2007) yielded a distance of $d = 1950 \pm 350$ pc, with a reddening of $E(B\text{-}V) = 1.18 \pm 0.11$ and a $\log(\tau) = 7.7$ dex, using 2MASS photometry. This distance roughly agrees with the one derived

Table 2.2: PNe and their possible associated OCs.

PN name	PN identifier	Cluster	Angular distance (arcmin)
Hen 2-133	G324.8-01.1	Lynga 5	2.6
Hf 69	G294.9-00.6	Lynga 15	4.5
WRAY 17-31	G277.7-03.5	Basel 20	8.6
		IC 2488	53
NGC 2899	G277.1-03.8	IC 2488	54
NGC 2452	G243.3-01.0	NGC 2453	8.8

by Zhang (1995a) for the PN (2550 ± 670 pc), but the OC reddening is lower than the reddening derived by Tylenda et al. (1992) and Cahn et al. (1992) for the planetary (2.46 ± 0.07). Such high difference in the color excess could imply a difference in the distance of about 2 kpc as can be seen in Neckel and Klare (1980), placing the PN in the background. On the other hand, Frew (2008) computed a PN distance of 5.0 ± 1.5 kpc, using the SB-r relation. This result almost doubles the previous one. Subsequent attempts to compute distances for the PN have shown contradictory results (see, for intance, Maciel, 1984; Phillips, 2004b; Stanghellini and Haywood, 2010), leaving the distance to the PN undefined. Majaess et al. (2007) claim their results are only preliminary, and recommend RV measurements to confirm the pair association. We have acquired new JHKs photometry from VVV, as well as new RVs for nine cluster stars and the PN. Methodology to study this pair is the same as for Lynga 15.

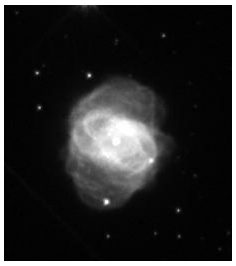

Figure 2.7: PN Hen 2-133 from MAST, taken with the WFC3/UVIS, filter F200LP (Proposal ID: 11657).

2.4 The quadruplet group WRAY 17-31,NGC 2899/IC 2488,Basel 20

This pair of clusters is located in the Vela constellation, lying near the end of the third Galactic quadrant and the beginning of the fourth one (Fig. 2.1). IC 2488 is an extended cluster whose cluster radius can reach $\sim 20'$. Contrary to the previous

clusters, IC 2488 has been well studied. Fig. 2.2 shows an outstanding group of bright stars in the center of the FOV, which contrasts with the spreaded stars on the FOV of Basel 20. The latter is a small and inconspicuous cluster located $\sim 44'$ from IC 2488.

Wray 17-31 (VBRC 2, ESO 166-21, Sa 3-10) is an elliptical PN that presents multiple shells with internal structure dominated by a ring (Fig. 2.3), and it is classified in HASH as Emprs. Its angular diameter is about 150 arcsec. Pena et al. (1997) obtained an expansion velocity of $28\,\mathrm{km\,s^{-1}}$ with a kinematical age of 16100 ± 2800 yr. A very faint and blue central star is visible between two blue brighter stars in the center of the image. Visual magnitude of the central star of the PN along with the distance indicate that the central star is in an evolutionary stage very near the white dwarf cooling sequence, with a relatively massive progenitor (Pena et al., 1997).

On the other hand, NGC 2899 (WRAY 16-47, Sa 2-45, Hen 2-30, ESO 166-13) is an asymmetric bipolar PN, which shows multiple shells with internal complex structure (Fig. 2.3). The PN extends in about 68 arcsec. Lopez et al. (1991) found multiple complex kinematical structures with mean expansion velocities of $43\,\mathrm{km\,s^{-1}}$ in H_α and $56\,\mathrm{km\,s^{-1}}$ in [NII]. From analysis of multiband photometry and echelle spectra, the authors concluded that NGC 2899 is an evolved PN with a massive core.

This interesting quartet (see Fig. 2.4) has been in the sight of researchers for a long time (Pedreros, 1987). Truth be told, the association has been suspected mainly between the pair of PNe WRAY 17-31 and NGC 2899 and the extended OC IC 2488. Distance cluster was established in a mean of $d = 1347 \pm 120$ pc (Clariá et al., 2003; Pedreros, 1987) with a reddening of $E(B\text{-}V) = 0.24 \pm 0.04$. The values are consistent with the parameters found to PN WRAY 17-31 by Pena et al. (1997), who estimated a distance of $d = 1200 \pm 200$ pc and a reddening $E(B\text{-}V) = 0.38$. Moreover, distances estimated to the PN NGC 2899 of $d = 1400 \pm 400$ pc Frew (2008) are also in good agreement with the cluster distance, as well as the published reddening of $E(B\text{-}V) = 0.32 \pm 0.24$ as reported in Majaess et al. (2007). In addition, RV measured for the NGC 2899 by Durand et al. (1998) yielded a value of $3.4 \pm 2.8\,\mathrm{km\,s^{-1}}$ in rough agreement with the value found for the cluster by Clariá et al. (2003) of $-2.63 \pm 0.06\,\mathrm{km\,s^{-1}}$, within $1sigma$ from the former despite the large uncertainty. The potential associations have often been dismissed due to the large angular separation between the PNe and the OC in about 53 arcmin (see Table 2.2). Nevertheless, Majaess et al. (2007) claim the PNe could be lying in the cluster corona, which has been found to host an important fraction of the progenitors of PNe. Frew (2008) also obtained a RV for WRAY 17-31 of $61 \pm 8\,\mathrm{km\,s^{-1}}$. This result could mean

that the cluster and WRAY 17-31 are not associated. However, OC Basel 20 lies just 8.6 arcsec from this PN, but the cluster has been poorly studied. In order to solve the questions we have obtained new RVs for eight stars in IC 2488, and eighteen stars in Basel 20, as well as for both of the PNe.

Chapter 3

Sample and methodology

3.1 Spectroscopic data

The intermediate-resolution spectra of 72 bright stars of the OCs were collected on April 18 and 19, 2013, during two nights of observations at the du Pont telescope at Las Campanas, Chile. The targets were selected on the IR CMD based on 2MASS data, prioritizing the brightest stars next to the cluster upper MS. The SIMBAD identifiers and 2MASS photometry of the targets are given in Table 3.1-3.5 and Fig. 3.1. The 1200 line/mm grating of the B&C spectrograph was used with a grating angle of 16°.67 and a 210μm slit width, to provide a resolution of 2 Å (R=2200) in the wavelength range 3750-5000 Å. Exposure times varied between 200s and 750s, according to the target's magnitude. A lamp frame for wavelength calibration was collected regularly every two science spectra during the night.

The spectra were reduced by means of standard IRAF routines. The frames were de-biased and flat-fielded using calibration frames acquired during daytime operations, and the one-dimensional spectra were subsequently extracted using Extract, an optimum algorithm (Horne, 1986). The sky background was estimated from two adjacent regions on both sides of the stellar spectrum and subtracted. The wavelength calibration was performed for each star on the lamp image collected immediately before or after the science frame. The lamp spectrum was extracted in the same pixels as the stellar one, to avoid the spectral curvature when introducing an offset. Fig. 3.2 shows some examples of the final reduced spectra. The resulting S/N for the selected targets was typically S/N=80–120. Non-target stars fell regularly in the slit in almost all exposures, because both the open cluster and the surrounding low-latitude Galactic field are very crowded. Their spectra were reduced and analyzed as those of our targets, but these stars were usually much fainter than our bright targets, and the resulting spectra were of much lower qual-

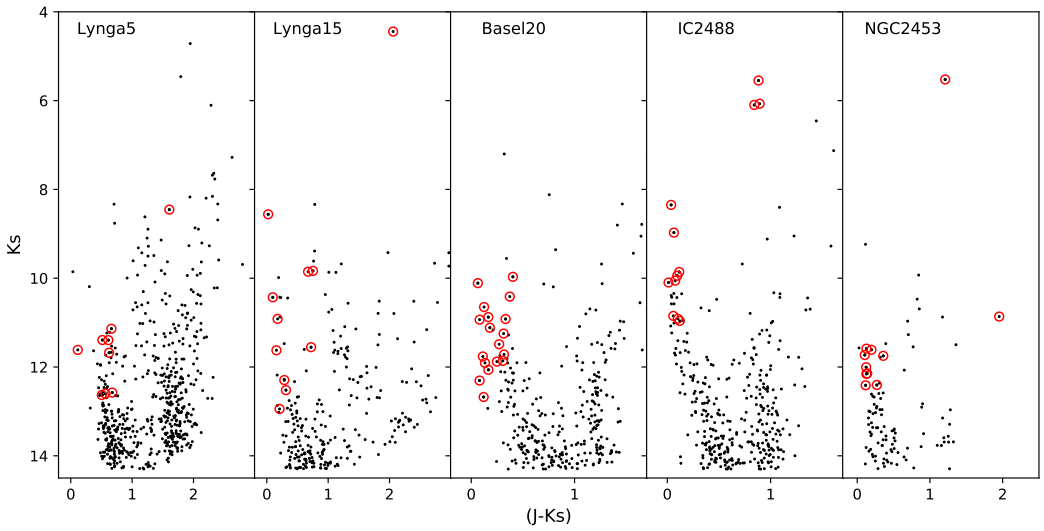

Figure 3.1: Color–magnitude diagrams of the program clusters. The 2MASS point sources within 3 arcmin from the cluster center are plotted as small dots. Unfilled red circles indicate the selected targets.

ity (S/N≈10–30). We will hereafter refer to "target" and "additional" stars, to distinguish between the selected objects and the stars that fell by chance in the spectrograph slit.

During the same run, we collected nine spectra of the the PNe. Three spectra were acquired for NGC 2452. One of them was obtained by centering the slit at the optical center of the nebula, where a bright spot was seen (see figures 2.3 and 2.5). The second and third spectra focused on the northern and southern regions, respectively. The reduction of these data proceeded as in the case of cluster stars, but the frames of a bright RV standard star were used during extraction in order to trace the curvature of the spectra on the CCD. The PN is an extended object, and its spectrum covered several pixels in the spatial direction. We performed both a narrow (8 pixels, $\sim 5''$) and a wide (20 pixels, $\sim 65''$) extraction for the Northern and central spectra, but only a narrow extraction for the southern one, because the flux was too faint outside ± 4 pixels from the center.

One spectrum was acquired for PN Hf 69, centering the slit at the optical center of the nebula with the slit placed parallel to two bright stars, slightly southern. The reduction of these data proceeded as in the case of cluster stars, but a bright star in the same field of the PN was used during extraction to trace the curvature of the spectra on the CCD. We performed two narrow extractions, one southern and the other one northern ($\sim 25''$ and $\sim 35''$, respectively) from the center, in order to avoid intruder stars.

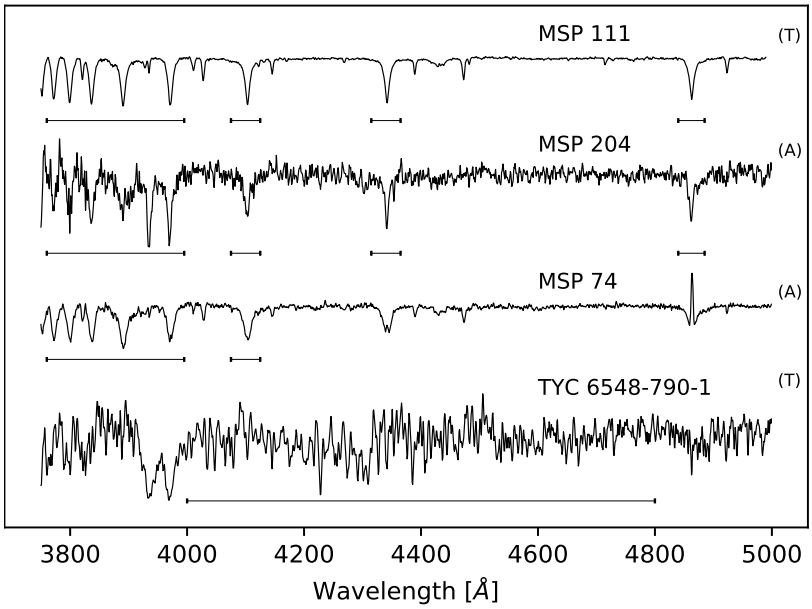

Figure 3.2: Examples of reduced spectra. The wavelength intervals used in RV measurements are shown as horizontal lines. The spectra are labeled as T and A for 'target' and 'additional stars', respectively. The spectra have been shifted vertically to avoid overlap.

One spectrum was acquired also for PN Hen 2-133. This planetary looks like a star through the telescope (recall Fig. 2.3) so only one extraction was performed. The reduction proceeded in the same way as the previous one.

Two spectra were obtained for NGC 2899. First slit was located by centering the optical center of the PN crossing east to west. The second slit was rotated to include the NE-SW brighter parts. We performed two narrow extractions for the first spectrum, and three additional extractions for the second one, including the brighter knots.

Only one spectrum was obtained to Wray 17-31, passing through the center in east to west direction. Three extractions were performed. The first one near to the bright star in the center, slightly shifted to east; the second one in the middle between the center and the brighter star in the eastern edge; and the third one between the center and the western edge.

3.2 Photometric data

3.2.1 UBV data

Our study of the fundamental parameters of the OC NGC 2452 is based on the optical $UBVRI$ photometric catalog presented by Moitinho (2001). The data were acquired in January 1998 at the CTIO 0.9m telescope, with a 2048×2048 Tek CCD, a resulting $0''.39$ pixel scale and a $13' \times 13'$ useful field of view. The typical seeing during the run was about $1.2''$. The frames were processed with standard IRAF routines, and the shutter effects were corrected applying a dedicated mask prepared during the reduction. The shutter mask was built and used to correct both flat field and object frames from shutter timing effects, prior to flat field division. We refer to Moitinho (2001) for a very detailed presentation of observations and data reduction.

3.2.2 JHKs data

The infrared (IR) JHKs photometry of both Lynga 15 and Lynga 5 was performed on the data collected by the Vista Variables in the Vía Láctea survey (Minniti et al., 2010; Saito et al., 2012; Hempel et al., 2014). The data were acquired between 2010 July 1 and 2011 September 11 with the VIRCAM camera mounted on the VISTA 4m telescope at the Paranal Observatory (Emerson and Sutherland, 2010), and reduced at the Cambridge Astronomical Survey Unit (CASU)* with the VIRCAM pipeline (Irwin et al., 2004)). During the observations, the weather conditions fell within the survey's constraints for seeing, airmass, and Moon distance (Minniti et al., 2010), and the quality of the data was satisfactory. Weidmann et al. (2013) have shown that the VVV photometry is also useful to study some properties of the PNe and to uncover new object in obscured regions.

Stellar photometry was performed around a wide field up to $\sim 1°$x$1°$ centered in the Lynga 15 center, and $\sim 10'$ from the Lynga 5, in the five YZJHKs bands of the VVV survey, employing the VVV-SkZ pipelines (Mauro et al., 2013) automated software based on ALLFRAME (Stetson et al., 1990), optimized for VISTA point-spread function photometry. The results were calibrated in the 2MASS astrometric and photometric system (Skrutskie et al., 2006), as detailed in Bidin et al. (2011) and Chené et al. (2012). The VVV frames saturate a Ks$\approx$12, but Mauro et al. (2013) showed that the PSF fit can recover correct magnitudes up to about two magnitudes above saturation. Fig 3.3 and 3.4 show the CDMs for the FOVs of

*http://casu.ast.cam.ac.uk

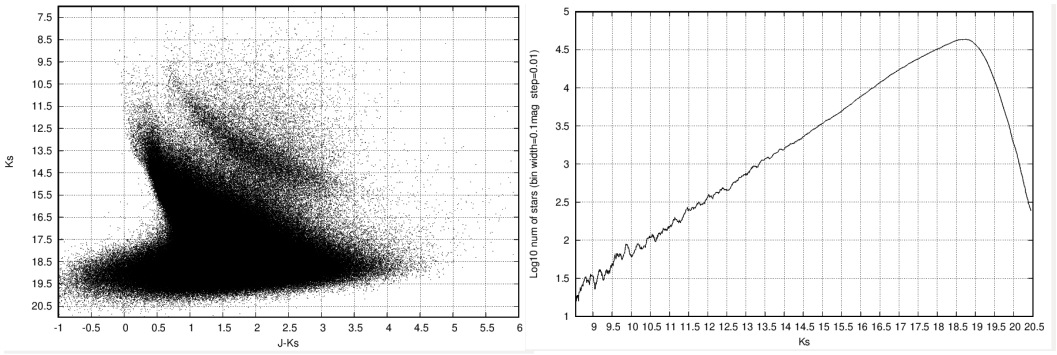

a b

Figure 3.3: Left panel: Color-Magnitude Diagram Ks vs J-Ks from the VVV Data for the FOV in Lynga 15. Right panel: number of star as a function of the Ks magnitude for the FOV in Lynga 15.

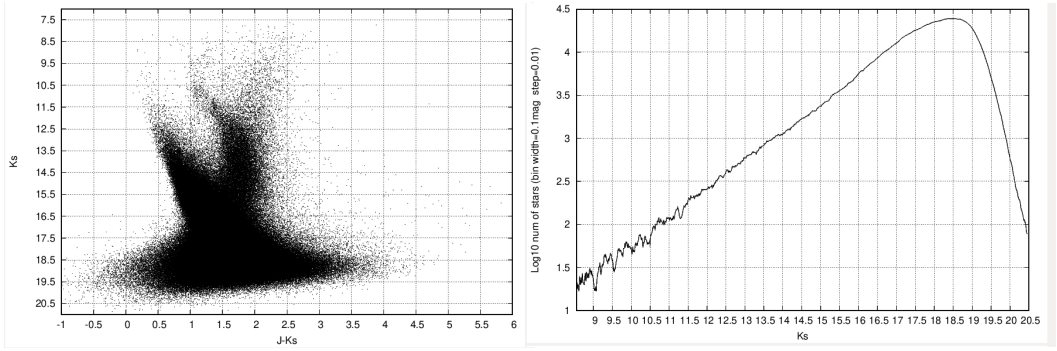

a b

Figure 3.4: Same as in Fig. 3.3 but for Lynga 5

Lynga 15 and Lynga 5 respectively, as well as the frequency curve of the number of stars in the Ks magnitude. In our analysis we selected stars 1 magnitude below the maximum frequency in each band as our limit of completeness.

On the other hand, in order to establish the fundamental parameters for both IC 2488 and Basel 20 we extracted photometric data from 2MASS database of a FOV of 3°×3°, around the center of the OC IC 2488. Data were restricted to stars with $J \leq 15.8$ mag, $H \leq 15.1$ mag, and $Ks \leq 14.3$ mag. These limits correspond to the 99% completeness limit of the 2MASS catalogue.

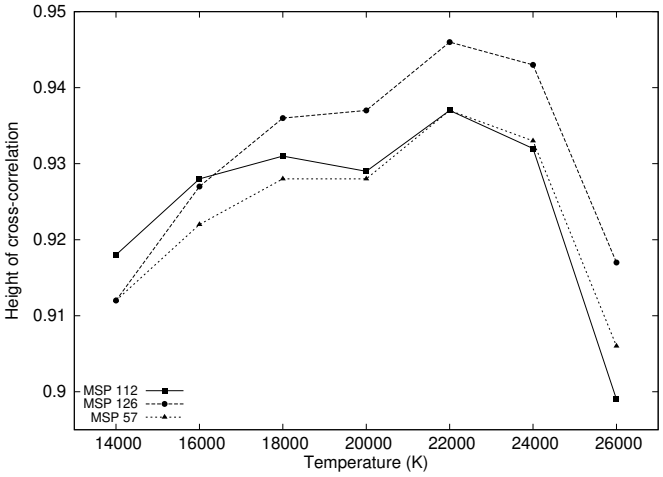

Figure 3.5: The height of the peak of the cross-correlation function as a function of the template temperature, for three Target stars.

3.3 Measurements

3.3.1 OCs: radial velocities

Radial velocities of program stars were measured using Fourier cross-correlation technique (Tonry and Davis, 1979) via *fxcor* IRAF task. The center of the correlation peak was fitted with a Gaussian profile. A grid of templates was prepared with synthetic spectra of solar metallicity drawn from the Coelho (2014)* library. The grid spanned the range from 375 to 500 nm in step of 0.02 Å, covering $3000 \leq T_{\rm eff} \leq 26000$ K and $2.5 \leq \log g \leq 4.5$, in step of 2000 K and 0.5 dex, respectively. Each target spectrum was first cross-correlated (CC) with the models of the grid, to study the variation of the correlation height with model temperature, as shown in Fig. 3.5. This first CC was performed in the range $3750 - 5000$ Å, comparing mainly the Balmer blue-UV lines and the continuum. The synthetic spectrum which provided the highest value was eventually adopted as template for the final measurement. Bidin et al. (2011) and Morse et al. (1991) showed that the exact choice of the template does not introduce relevant systematics, although a mismatch between the target and the template spectral type can increase the resulting uncertainties.

The radial velocity of hot stars was eventually measured with a CC restricted to the dominant Balmer lines (see MSP 111 in Fig. 3.2), i.e. in the intervals $4840-4885$ Å (H_β), $4315-4365$ Å (H_γ), $4075-4125$ Å (H_δ), and $3760-3995$ Å (H_ϵ to H_{12}). The lines with hints of core emissions, namely H_β and H_γ in MSP 74 were excluded from

*http://specmodels.iag.usp.br/

the CC. Spectral features analysis for cold stars demanded more care. While they were bright stars, the low resolution blended the closest features (see TYC 6548-790-1 spectrum), although the noise was not the dominant source of uncertainties in the optical range. Nevertheless, these stars were faint in the blue-UV edge of out spectra, where the camera was less efficient also (QE of 55% at 3500 Å against 80% at 4000 Å). In order to avoid possible sources of systematics at the CCD borders, we measured the radial velocities using the wavelength interval $4000 - 4800$ Å. The central peak of the cross-correlation function (CCF) was higher than 0.95 for the target stars, indicating a high degree of similarity with the adopted template, except for the cooler ones, for which they reached 0.82 only.

All RVs were measured relative to the solar system barycenter. Zero point corrections were made using six standard stars (three per night) of spectral type K and G (Chubak et al., 2012) treated in the same way as the cold stars described above. The results are reported in Tables 3.1 to 3.5.

RV measurements were performed on both targets and additional stars for the OC NGC 2453. However, the results for the latter are not reliable, because the random location of their PSF centroid in the spectrograph slit could easily have introduced a large systematic on their RV. In fact, the target stars MSP 132 and MSP 85 showed a very different RV when they fell as additional objects in other frames, and the two measurements of the additional star 2MASS J07473034-2711464 differ noticeably (see Table 3.1). Hence, we report the results for all measurements only for NGC 2453, but for the other clusters we will exclude the additional stars from RV analysis.

3.3.2 *Star temperatures and gravities*

The fundamental parameters (temperature, gravity, and rotation velocity) of the most likely member (MLM) of the clusters were measured as in Moni Bidin et al. (2017), by means of the routines developed by Bergeron et al. (1992) and Saffer et al. (1994), as modified by Napiwotzki et al. (1999). Briefly, the available Balmer and He lines were fitted simultaneously with a grid of synthetic spectra obtained from model atmospheres of solar metallicity, computed with ATLAS9 (Kurucz, 1993). The stellar rotation projected along the line of sight, $v \sin i$, is not a fit parameter but an input quantity of the routines. It was therefore varied manually until finding the value which returned the solution with the lowest χ^2. The results for the NGC 2453 are given in Chap. 4 (Table 4.2) and for Lynga 5 in Chap. 6 (Table 6.1), along with the photometric data of the targets from our optical photometry. The algorithm does not take into account possible sources of systematic error,

such as the flat fielding procedure, the continuum definition, and the spectrum normalization. Hence, the errors returned by the routine were multiplied by a factor of three to derive a more realistic estimate of the uncertainties (see, e.g., (Moni Bidin et al., 2017)).

The stellar temperature is mainly derived from the relative intensity of the Balmer lines, which is well measured in our spectra. On the contrary, surface gravity is estimated from the width of these features, but the method was insufficient to properly resolve its effects. In fact, we found a general underestimate of $\log g$ by about 0.2 dex when compared to expectations for MS objects ($\log g \approx 4.2$), possibly due to the combination of a low spectral resolution and unresolved effects of stellar rotation. However, Zhang et al. (2017) suggested that the method might be underestimating the surface gravity of MS stars by $\sim$0.1 dex even at very high spectral resolution.

3.3.3 *PNe: radial velocites*

The spectrum of PNe are shown in Fig. 3.6. Bright emission lines of [OII] (3727 Å), [NeIII] (3967 Å, 3869 Å), HeII (4686 Å), and the Balmer lines H_β (4861 Å), H_γ (4340 Å) and H_δ (4102 Å) can be easily identified.

The RVs of the PNs were measured by CC with a synthetic spectra. These were built adding up Gaussian curves with equal widths and heights to the observed features, but centered at the laboratory wavelengths taken from NIST Atomic Spectra Database Lines Form*. The reduction returned seventeen spectra in total: five for NGC 2452, namely a wide and narrow extraction for both the northern and the central regions, and a narrow extraction for the southern one; six for NGC 2899; three for Wray 17-31; two for Hf 69; and one more for Hen 2-133. The measurements were repeated independently for the seventeen spectra, to verify if the results could be affected by the internal kinematics of the nebula. We did not detect any systematic error between the spectra beyond fluctuations compatible with observational errors. The final estimate was obtained from the average of these measurements. They can be seen in Table 3.6.

3.3.4 *Gaia* distances

Parallaxes and proper motions for program stars were obtained from the Gaia Second Data Release (DR2)† catalog. It provides a 5-parameter astrometric solu-

*https://www.nist.gov/pml/atomic-spectra-database
†Gaia Archive: https://gea.esac.esa.int/archive/

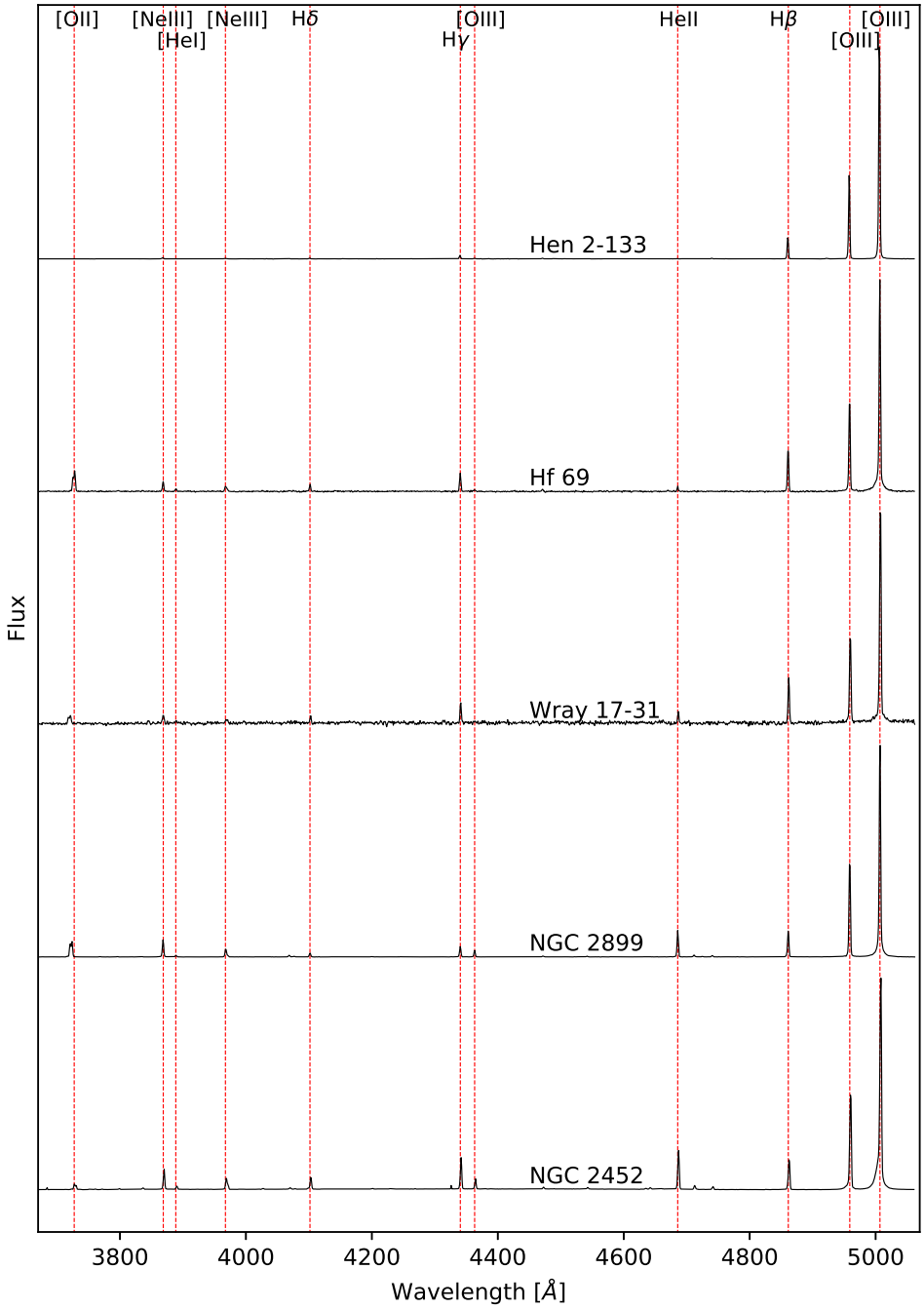

Figure 3.6: Reduced spectrum of the PNe. The flux was normalized to the height of the [OIII]λ 5007 line. The spectra have been shifted vertically to avoid overlap.

Table 3.1: Photometric data, radial velocities, and distances of the program objects of the OC NGC 2453.

Name	Type	J (mag)	J-H (mag)	$\mu^{\dagger}_{\alpha^*}$ (mas yr^{-1})	$\mu^{\dagger}_{\delta}$ (mas yr^{-1})	RV (km/s)	Distance (kpc)	Note‡
TYC 6548-790-1	T	6.73 ± 0.02	0.85 ± 0.06	−2.33 ± 0.04	3.40 ± 0.05	80 ± 10	$5.2\,^{6.2}_{4.4}$	MLM
MSP 111	T	11.81 ± 0.02	0.10 ± 0.05	−2.35 ± 0.04	3.41 ± 0.05	69 ± 4	$5.4\,^{6.5}_{4.6}$	MLM
MSP 112	T	12.28 ± 0.03	0.12 ± 0.06	−2.38 ± 0.04	3.39 ± 0.04	89 ± 6	$4.6\,^{5.4}_{4.0}$	MLM
MSP 126	T	12.28 ± 0.02	0.09 ± 0.05	−2.18 ± 0.04	3.64 ± 0.04	89 ± 7	$4.2\,^{4.7}_{3.7}$	MLM
MSP 159	T	12.13 ± 0.03	0.09 ± 0.06	−2.41 ± 0.05	3.48 ± 0.05	88 ± 8	$4.4\,^{5.3}_{3.8}$	MLM
MSP 85	T	12.53 ± 0.02	0.08 ± 0.05	−2.29 ± 0.04	3.45 ± 0.04	87 ± 7	$4.6\,^{5.3}_{4.1}$	MLM
	A					117 ± 7		
MSP 132	T	11.83 ± 0.02	0.10 ± 0.05	−2.13 ± 0.06	3.46 ± 0.06	72 ± 4	$4.7\,^{5.8}_{3.9}$	MLM
	A					28 ± 4		
NGC 2453 55	T	12.82 ± 0.05	0.15 ± 0.10	−1.64 ± 0.10	5.08 ± 0.20	64 ± 6	$11.0\,^{14.4}_{8.4}$	NM, $\varpi < 0$
MSP 57	T	11.71 ± 0.02	0.09 ± 0.05	−2.47 ± 0.06	3.59 ± 0.06	103± 5	$1.2\,^{1.2}_{1.1}$	NM
NGC 2453 16	T	12.11 ± 0.04	0.15 ± 0.09	−4.91 ± 0.04	4.10 ± 0.05	16 ± 2	$1.3\,^{1.3}_{1.2}$	NM
MSP 211	T	12.68 ± 0.03	0.15 ± 0.06	−2.35 ± 0.03	3.48 ± 0.04	18 ± 8	$4.4\,^{4.8}_{4.0}$	NM
2MASS J07473821-2710479	A	15.23 ± 0.06	0.25 ± 0.10	−2.39 ± 0.07	3.51 ± 0.08	72 ± 6	$2.8\,^{3.4}_{2.4}$	
2MASS J07473390-2710060	A	15.36 ± 0.05	0.37 ± 0.10	−3.08 ± 0.09	2.98 ± 0.10	66 ± 15	$3.4\,^{4.5}_{2.7}$	
MSP 52	A	14.24 ± 0.08	0.17 ± 0.20	−2.36 ± 0.04	3.35 ± 0.05	−11 ± 4	$4.2\,^{4.9}_{3.7}$	
MSP 272	A	12.89 ± 0.03	0.25 ± 0.05	−1.08 ± 0.20	4.40 ± 0.20	−50 ± 9	$0.9\,^{1.0}_{0.8}$	
MSP 76	A	12.91 ± 0.02	0.16 ± 0.04	−2.40 ± 0.03	3.48 ± 0.03	18 ± 3	$4.1\,^{4.4}_{3.7}$	
MSP 141	A	—	—	−2.36 ± 0.04	3.49 ± 0.05	44 ± 4	$4.2\,^{4.9}_{3.8}$	
MSP 74	A	11.87 ± 0.03	0.21 ± 0.06	−2.36 ± 0.03	3.42 ± 0.05	103± 6	$3.5\,^{3.9}_{3.2}$	
2MASS J07473034-2711464	A	14.68 ± 0.03	0.05 ± 0.05	−2.34 ± 0.09	3.83 ± 0.10	97 ± 5	$2.0^{2.3}_{1.8}$	
	A					70 ± 4		
2MASS J07473176-2710057	A	14.58 ± 0.07	0.36 ± 0.20	−2.11 ± 0.06	3.50 ± 0.07	66 ± 6	$3.6^{4.3}_{3.1}$	
MSP 204	A	14.18 ± 0.07	0.24 ± 0.20	−2.20 ± 0.05	3.38 ± 0.05	101 ± 5	$4.2^{4.9}_{3.7}$	
MSP 223	A	14.06 ± 0.04	0.16 ± 0.08	−2.32 ± 0.04	3.36 ± 0.04	64 ± 4	$3.7^{4.1}_{3.3}$	
MF54	-	10.44 ± 0.03	0.17 ± 0.06	−2.24 ± 0.20	3.47 ± 0.40	67 ± 14††	$4.2^{6.5}_{2.9}$	ϖ/σ_{ω}=0.96

† Data from *Gaia* DR2.
‡ MLM: Most Likely Member; NM: Non Member.
†† Data from Moffat and Fitzgerald (1974)

Table 3.2: Photometric and astrometric data for target stars of Lynga 15.

ID	**J** (mag)	**H** (mag)	**K** (mag)	μ_{α^*} (mas yr^{-1})	μ_δ (mas yr^{-1})	ϖ (mas)	**RV** (km/s)
2MASS 11421522-6227168	10.53±0.02	9.95±0.02	9.85±0.02	-8.74±0.05	0.93±0.05	0.54±0.03	-54±10
IRASİ1399-6210	6.50±0.02	5.08±0.08	4.44±0.03	-5.6±0.2	1.4±0.2	-0.002±0.100	-15±14
2MASS 11421581-6227306	11.09±0.02	10.95±0.02	10.92±0.03	-8.72±0.05	1.21±0.05	1.40±0.03	-60±4
2MASS 11421449-6227306	11.78±0.02	11.63±0.02	11.62±0.03	-6.70±0.05	0.61±0.05	0.38±0.03	-51±3
V* V916 Cen	8.58±0.02	8.58±0.04	8.56±0.02	-6.65±0.08	1.22±0.07	0.35±0.05	-58±7
2MASS 11422640-6228106	12.83±0.03	12.63±0.02	12.52±0.04	-8.54±0.04	1.86±0.03	0.38±0.02	-40±6
2MASS 11422776-6227378	13.15±0.05	13.04±0.05	12.94±0.04	-5.29±0.03	0.28±0.03	0.34±0.02	-40±3
2MASS 11422728-6229443	12.58±0.03	12.40±0.03	12.29±0.03	-5.39±0.03	1.63±0.03	0.343±0.02	-66±2
2MASS 11422634-6230125	12.27±0.03	11.74±0.03	11.55±0.03	-23.55±0.08	2.22±0.07	2.02±0.05	-35±8
HD 308888	10.53±0.05	10.48±0.09	10.43±0.02	-6.49±0.05	0.97±0.04	0.51±0.03	-57±3
2MASS 11420842-6230225	10.59±0.05	9.99±0.07	9.83±0.02	2.67±0.05	-0.45±0.05	0.52±0.04	16±7

Table 3.3: Photometric and astrometric data for target stars of Lynga 5.

ID	Ks (mag)	J-Ks (mag)	μ_{α^*} (mas yr^{-1})	μ_δ (mas yr^{-1})	ϖ (mas)	RV (km s^{-1})	Likelihood (%)
TYC 8704-1650-1	8.45±0.05	1.60±0.10	-20.60±0.10	-13.66±0.10	4.24±0.07	-51±8	<50
Gaia DR2 5882742183394557312	11.14±0.05	0.66±0.08	-3.79±0.05	-3.50±0.05	0.36±0.03	-36±4	97
Gaia DR2 5882742011595850496	11.39±0.03	0.51±0.05	-3.48±0.04	-3.43±0.04	0.29±0.03	-50±6	98
Gaia DR2 5882736033000609536	11.40±0.05	0.61±0.09	-2.93±0.04	-2.12±0.04	0.61±0.03	15±7	63
Gaia DR2 5882742144709393792	11.62±0.04	0.11±0.04	-5.00±0.50	-5.27±0.50	-0.96±0.30	32±11	<50
Gaia DR2 5882741942876372096	11.68±0.05	0.60±0.10	-3.62±0.05	-4.00±0.05	0.17±0.03	-48±3	88
Gaia DR2 5882730191844742016	12.58±0.05	0.68±0.09	-4.22±0.06	-6.47±0.06	0.73±0.04	-22±19	<50
Gaia DR2 5882741942849715072	12.60±0.03	0.56±0.06	-3.54±0.07	-3.65±0.07	0.33±0.04	-110±9	98
Gaia DR2 5882741942876369152	12.63±0.02	0.506±0.04	-3.75±0.06	-3.57 ±0.06	0.23±0.04	-83±3	95

Table 3.4: Photometric and astrometric data for the target stars of IC 2488.

ID	Ks (mag)	J-Ks (mag)	μ_{α^*} (mas yr^{-1})	μ_δ (mas yr^{-1})	ϖ (mas)	RV (km s^{-1})	Likelihood (%)
HD 302214	5.55±0.02	0.88±0.04	-7.91±0.06	5.59±0.06	0.74±0.03	-1±11	96
HD 302212	6.07±0.02	0.89±0.05	-7.52±0.07	5.93±0.07	0.67±0.03	-6±11	86
HD 302215	6.10±0.02	0.84±0.05	-7.66±0.06	5.30±0.05	0.67±0.03	-2±12	51
HD 302225	8.35±0.04	0.04±0.07	-7.67±0.07	5.46±0.06	0.60±0.04	-1±3	84
HD 302213	8.97±0.03	0.06±0.05	-4.87±0.07	3.91±0.07	0.80±0.04	0±3	<50
HD 302222	9.86±0.02	0.12±0.04	-7.76±0.07	5.67±0.07	0.59±0.04	0±3	73
HD 302226	9.94±0.02	0.10±0.04	-7.79±0.08	5.55±0.08	0.67±0.04	-15±3	86
HD 302220	10.06±0.02	0.08±0.04	-7.79±0.06	5.59±0.06	0.72±0.03	-1±2	97
HD 302216	10.10±0.02	0.01±0.04	-7.81±0.06	5.74±0.06	0.62±0.03	-8±3	86
TYC 8592-448-1	10.85±0.02	0.06±0.05	-8.00±0.05	5.43±0.05	0.70±0.03	7±3	97
HD 302211	10.91±0.02	0.10±0.05	-7.78±0.06	5.80±0.06	0.67±0.03	-1±3	86
HD 302210	10.96±0.02	0.12±0.04	-8.24±0.06	5.60±0.06	0.69±0.03	-4±2	83

Table 3.5: Photometric and astrometric data for the target stars of Basel20.

ID	Ks (mag)	J-Ks (mag)	μ_{α^*} (mas yr^{-1})	μ_δ (mas yr^{-1})	ϖ (mas)	RV (km s^{-1})
TYC8592-1737-1	9.97±0.02	0.40±0.05	35.31±0.05	-26.18±0.05	2.86±0.03	20±12
HD300143	10.11±0.02	0.06±0.04	-7.92±0.09	5.70±0.07	1.02±0.04	20±2
TYC8592-2216-1	10.41±0.03	0.37±0.05	-7.05±2.11	14.73±2.15	2.34±1.07	-4±9
TYC8592-1772-1	10.65±0.02	0.12±0.04	-5.63±0.05	4.40±0.05	0.39±0.03	-1±3
TYC8592-730-1	10.88±0.03	0.17±0.05	-5.97±0.42	1.17±0.39	1.21±0.20	21±3
TYC8592-2142-1	10.92±0.02	0.33±0.05	-18.98±0.05	30.46±0.04	1.41±0.02	-28±10
HD300145	10.93±0.03	0.08±0.05	-7.92±0.14	4.68±0.12	1.18±0.06	1±2
TYC8592-1879-1	11.12±0.03	0.18±0.05	-10.22±0.05	8.26±0.04	1.30±0.02	26±13
2MASS09301982-5624117	11.25±0.02	0.31±0.05	-27.60±0.05	23.37±0.04	2.25±0.03	-15±14
2MASS09302836-5629307	11.49±0.03	0.27±0.05	0.96±0.05	4.02±0.05	1.49±0.03	-17±9
2MASS09301532-5622432	11.72±0.02	0.32±0.05	-9.22±1.03	2.50±0.99	0.91±0.58	-10±6
2MASS09301520-5622568	11.76±0.02	0.11±0.04	-10.98±0.05	4.84±0.05	0.99±0.03	-20±3
2MASS09302754-5621494	11.86±0.04	0.31±0.07	-6.27±0.03	5.99±0.03	1.51±0.02	12±9
2MASS09311938-5620008	11.88±0.03	0.25±0.06	-6.53±0.04	3.33±0.03	1.09±0.02	2±7
2MASS09302262-5628176	11.91±0.02	0.13±0.04	-5.62±0.05	3.96±0.04	0.66±0.03	-18±26
2MASS09311637-5629016	12.06±0.03	0.17±0.05	-6.32±0.05	5.90±0.05	0.53±0.03	-13±2
2MASS09310472-5626451	12.31±0.02	0.08±0.05	-7.80±0.05	5.71±0.05	0.78±0.03	-30±3
2MASS09311779-5621460	12.68±0.04	0.12±0.10	-8.35±0.04	4.63±0.03	0.63±0.02	-15±5

Table 3.6: RVs for the PNe.

PN name	PN identifier	RV (km s^{-1})
NGC 2452	G243.3-01.0	62±2
Hf 69	G294.9-00.6	-15±2
Hen 2-133	G324.8-01.1	-23±2
NGC 2899	G277.1-03.8	-6±3
WRAY 17-31	G277.7-03.5	35±1

tion (coordinates, proper motions, parallax ϖ) for more than 1.3 billion sources (Brown et al., 2018). We added +0.029 mas to all Gaia parallaxes, as advised by Lindegren et al. (2018), to account for the zero-point offset reported by Lindegren et al. (2018) and Arenou et al. (2018a). Recent discussions have shown that the traditional method of estimating distances inverting the parallax value, and computing its formal error as the first order Taylor expansion, is not appropriate when the error on the relative error on the parallax is larger than 20% (Bailer-Jones, 2015; Astraatmadja and Bailer-Jones, 2016). The reasoning is based on the expected distribution of the measured parallax ϖ that follows:

$$P(\varpi|r,\sigma_\varpi) = \frac{1}{\sqrt{2\pi}\sigma_\varpi} exp\left[-\frac{1}{2\sigma_\varpi^2}\left(\varpi - \frac{1}{r}\right)\right] \tag{3.1}$$

where $\sigma_\varpi \geq 0$, is a gaussian distribution in ϖ, but not in the true distance r. Actually, σ_ϖ is an stochastic variable with a noisy measurement of the true parallax (1/r).

Following the guidelines of Luri et al. (2018), we employed a Bayesian method to infer distances from parallaxes through a model error and a priori assumption. In the case of Gaia parallaxes, the model error behaves approximately as a Gaussian distribution of mean $1/r$ and standard deviation σ equal to the parallax error. Because the fractional errors on parallax are $f_\omega = \sigma/\varpi \leq 0.24$ for most program stars, we used the Exponentially Decreasing Space Density function (EDSD) as a prior, as described by Bailer-Jones (2015):

$$P_{EDSD}(r) = \begin{cases} \frac{1}{2L^3} r^2 e^{-r/L} & \text{for} \quad r > 0 \\ 0 & \text{otherwise} \end{cases} \tag{3.2}$$

where L > 0 is a length scale. This prior assumes a spherical star distribution where the probability of finding a star decreases exponentially with the distance. The mode of this distribution represents the distance value of maximum probability, and in the case of EDSD, it shows better performance than other estimators as, for instance, the median. Modes for larger fractional errors ($f_\omega \sim 1.00$) can reach small global biases, but they can underestimate the distance, and the related statistical errors are very large. On the other hand, EDSD admits negative parallaxes besides the huge error intervals and the fact that EDSD always underestimates the true distance. Both large fractional errors and negative parallaxes are not suitable for computing distances. A complete Bayesian analysis tutorial is available as Python and R notebooks and source code from the tutorial section on the Gaia archive*.

*https://github.com/agabrown/astrometry-inference-tutorials/

We reported here the modal distances, d, computed through the parallaxes from Gaia DR2 as $d^{d_{max}}_{d_{min}}$, where the upper and lower indices correspond to minimum and maximum distances in the error interval of the 5% and 95% quantile, respectively.

3.4 Method

3.4.1 Density profiles

To identify accurate location of each cluster studied in this article, we first construct density contour maps on small regions around the center coordinates of the OCs reported in literature. Because density contour maps use Gaussian KDE, large FOVs allow only the largest structures to be seen, while the small ones remain hidden. Circular areas with radii between 5-10 arcmin were selected to visually inspect the field around each cluster, except around IC 2488 due to its large cluster size which required a radius > 20 arcmin. Radial density profiles (RDPs) were then computed on a grid of points in the most stand out areas of the density maps. In regions where an over-density is not clearly identified, the grid covered a square of $6' \times 6'$ in steps of $20''$ for a total of 324 RDPs plots. One visual inspection was done in order to identify the higher over-densities of the RDP. Then, a second squared grid was run around those points covering $1' \times 1'$ in steps of $\sim 6''$. On the contrary, in regions with a clear density identification only finer grids were run. All RDPs were constructed spanning circular areas to the edge of the VVV data FOV. That means that, for example, OC Lynga 15 (those FOV is $1° \times 1°$) RDPs radii reach up to $\sim 20'$, while for other cluster, namely, Loden 467 they reach only $\sim 3'$. Variable width rings were used, counting the number of stars inside each ring and then dividing by the area. Variable width rings fit both inner (narrower rings) and outer (wider rings) cluster regions (Maia et al., 2010; Angelo et al., 2019).

The highest densities in RDPs were evaluated to assure that they were statistically significant compared to the field densities. The algorithm is based on the instructions given by Pavani et al. (2011). It consists, in summary, of comparing the number of stars within a given area centered in the overdensity point (N_{over}) with the number of stars from a set of 100 random samples each having the same area, but in the surrounding field (N_{field}). Figure 3.7 shows an example of the procedure. The percentile of $N_{over}/\langle N_{field}\rangle$ in $N_{field}/\langle N_{field}\rangle$ distribution was evaluated, where $\langle N_{field}\rangle$ is the average value taken on the total sample in the surrounding field. The area is increased, allowing us to estimate the percentile for a set of radius. Shorter areas were compared with a set of 1000 random samples. The algorithm is repeated ten times to take into account fluctuations in the number of

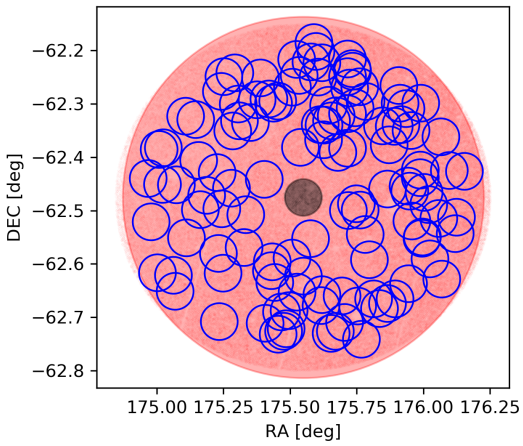

Figure 3.7: 20′ FOV centered at Lynga 15 from VVV data. Gray zone illustrates stars within an area of 2′ around the cluster. Red zone represents the field. Blue circles are the set of 100 circles centered randomly in the field with radius of 2′.

stars for each radius. A significant contrast with the field is revealed when at least one percentile is above the 95%. Maximum percentiles were reached at small radii.

We did the procedure for the largest over-densities. The final coordinates for the clusters were identified at the point on the grid that showed the maximum percentile difference from the star field counts.

3.4.2 Star cluster membership

Overdensities in the star crowded fields are barely an indicative of the presence of a star cluster. Nevertheless, statistically speaking, a star cluster should share besides same area in the sky, both the same distance and proper motions. It is possible to assign a membership likelihood to tighter stars in the parameter space of parallax and proper motions ($\mu_\alpha \cos\delta$, μ_δ, ϖ) (Cantat-Gaudin et al., 2018a; Liu and Pang, 2019; Angelo et al., 2019; Perren et al., 2020). Data for stars in circular areas centered on the final overdensity points were extracted from Gaia DR2 for a radius $R > 5 \times R_{over}$, where R_{over} is the radius in which the star density profile makes equal the field variations. Photometric and astrometric quality of the data were verified selecting data as recommended by Arenou et al. (2018a) to filter spurious solutions. In addition, a correction of +0.029 mas to all *Gaia* parallaxes was done, as advised by Lindegren et al. (2018).

We followed a procedure analogous to Angelo et al. (2019), using the same notation as in Dias et al. (2018) and Angelo et al. (2019), in order to determine the most

likely members of the cluster. The procedure is discussed in detail by the authors, so we will just make a summary here. The sample of the stars is extracted in both the cluster and field area. The first one is defined in a circular region centered in the point of overdensity ($R \leq R_{over}$), while the field region is defined in a ring with the same area as the cluster but with the inner annulus $R > 3 \times R_{over}$. The procedure consists of dividing the astrometric space into cells with widths of ($10 \times \langle \Delta\mu_{\alpha^*} \rangle$, $10 \times \langle \Delta\mu_{\delta} \rangle$, $\langle \Delta\varpi \rangle$), where the expression in angle brackets means the average of the natural uncertainties of the total sample. For each cluster star in a 3D cell a membership likelihood $l_{\rm star}$ is computed by:

$$l_{\rm star} = n \frac{\exp\left[-\frac{1}{2}\left(\mathbf{X}-\mu\right)^T \mathbf{\Sigma}^{-1}\left(\mathbf{X}-\mu\right)\right]}{\sqrt{(2\pi)^3\left|\mathbf{\Sigma}\right|}}\,, \tag{3.3}$$

where n is a dimensionless constant added by us, which takes the value $n = 1$ for fields with low star density (we will return to the value of n below); $\mathbf{X}$ is the column vector ($\mu_\alpha \cos\delta$, μ_δ, ϖ), $\boldsymbol{\mu}$ is the mean of the column vector for the cluster stars in the cell, and $\mathbf{\Sigma}$ is the full covariance matrix, which takes into account the uncertainties (σ) and their correlations (ρ) as follows:

$$\sum = \begin{bmatrix} \sigma^2_{\mu_{\alpha^*}} & \sigma_{\mu_{\alpha^*}}\sigma_{\mu_\delta}\rho_{\mu_{\alpha^*}\mu_\delta} & \sigma_{\mu_{\alpha^*}}\sigma_{\varpi}\rho_{\mu_{\alpha^*}\varpi} \\ \sigma_{\mu_{\alpha^*}}\sigma_{\mu_\delta}\rho_{\mu_{\alpha^*}\mu_\delta} & \sigma^2_{\mu_\delta} & \sigma_{\mu_\delta}\sigma_{\varpi}\rho_{\mu_\delta\varpi} \\ \sigma_{\mu_{\alpha^*}}\sigma_{\varpi}\rho_{\mu_{\alpha^*}\varpi} & \sigma_{\mu_\delta}\sigma_{\varpi}\rho_{\mu_\delta\varpi} & \sigma^2_{\varpi} \end{bmatrix}. \tag{3.4}$$

The total likelihood for the stars in the cell will be given by the product of the individual likelihoods, $\mathcal{L} = \Pi_i l_i$. Same procedure is also computed for the field stars within the same 3D cell. The presence of possible clustering stars will be indicated when the degree of spreadness of the cluster data will be less than that of the field. This is assessed using -log($\mathcal{L}$), an analogous expression to the entropy in the parameter space. We refer the reader to Angelo et al. (2019, their section 3.2) to more details. The final membership likelihood for each star that meets the condition above is given by the expression:

$$L_{star} \propto \exp\left(-\frac{\langle N_{clu}\rangle}{N_{clu}}\right)\,, \tag{3.5}$$

where $\langle N_{clu}\rangle$ is the average number of stars over the whole set of cells for a given grid. The procedure is repeated for 27 different grid configurations increasing and decreasing the cell sizes in one-third of the mean sizes. However, we have checked that when the number of stars of the sample is small, the results are very sensitive to both the cell sizes and the selection of the initial values of the grids. As a new

feature, we also considered running additional grid sets to sweep wider and finer cell sizes. This was achieved by multiplying the initial set by factors of 2 and 0.5, and repeating the procedure. When all the different sets of cell widths were applied, the algorithm took into account 729 independent combination of grids.

Equation 3.3 is used to find grids containing stars which are more clustered than the field, but it is not the final probability of the membership. The algorithm was developed to study fields that have a low density of stars. When a field has a very high density of stars hosting a cluster, it can happen that $\mathcal{L} \longrightarrow 0$, and then -log($\mathcal{L}$) is undefined. As result, the cluster might not be identified. With the purpose of using the algorithm with crowded fields, we added the constant n in Eq. 3.3. Value for n must be carefully chosen. It can be increased as a power of 10 (such as 10, 100, 1000, etc) until the indefiniteness is avoided, but always keeping $l_{star}<1$.

Finally, the most likely members (MLM) found from Gaia DR2 are cross-matched with VVV data, and an isochrone of solar metallicity is fitted at almost all Ks vs (J-Ks) diagrams in this work, in order to obtain the photometric distance, reddening and age. We employed the extinction law by Rieke and Lebofsky (1985) for infrared bands related to E(B-V) according to $A_{\rm V} = 3.09E(B-V)$, $A_{Ks} = 0.112A_{\rm V}$ and $A_{(J-Ks)} = 0.17A_{\rm V}$. Weighted average parallax for MLM is used as a first guess to fit the isochrone. We used the EDSD as a prior in all cases to compute the distance from the parallax.

3.4.2.1 Verifying the method

Method described in section 3.4.2 was verified for the OCs NGC 4349 and van den Bergh-Hagen 85 (vdBH 85) using *Gaia* DR2. These clusters were selected because they have different features. NGC 4349 is a bright cluster clearly noticeable from the background, while vdBH 85 is an old and faint cluster, barely distinguishable from the background. Both open clusters were studied by Perren et al. (2020) using the same parameter space of proper motions and parallax from Gaia DR2, but the authors used a different algorithm. The procedure used here returns likelihoods for each star where spreadness is less than the field's in a cell given, but just the tighter star groups in the parameter space get higher likelihoods (see Angelo et al., 2019, their section 3.2). Figure 3.8 shows the result of applying the algorithm to both clusters. Plots on the left column correspond to NGC 4349, and the ones on the right correspond to vdBH 85. Diagrams of parallax vs G magnitude (top panels) and proper motions (middle panels) show the stars with maximum likelihood values (red points) forming clumps. Bottom panels show CMD with G vs (BP-RP).

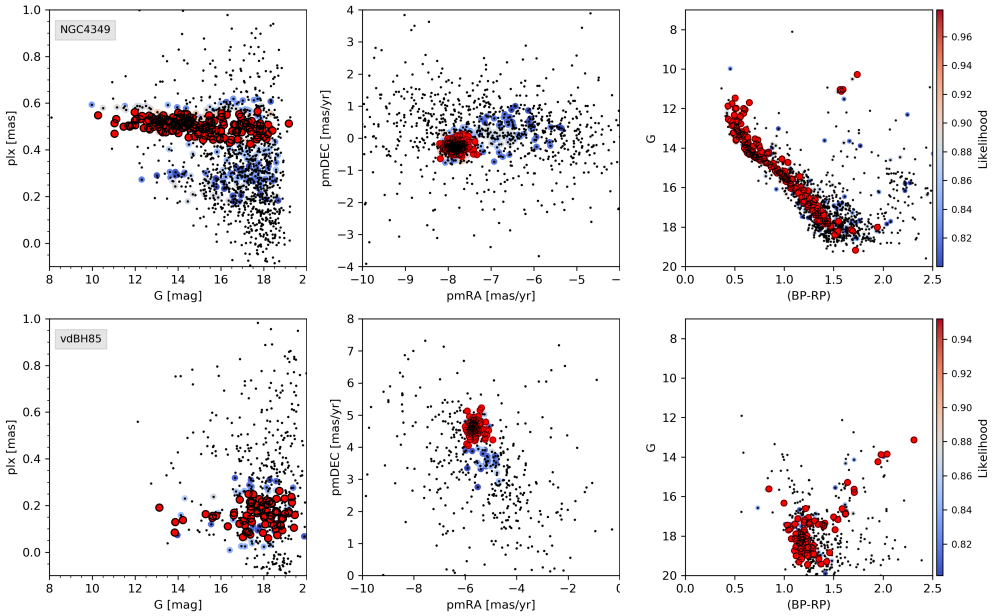

Figure 3.8: From left to right: parallax vs apparent magnitude G, Proper motions, and G vs (BP-RP) diagrams for stars of the open clusters NGC 4349 (top panel) and van den Bergh-Hagen 85 (bottom panel). Black dots represent stars within the cluster radius from Gaia DR2. Colored circles depict the membership probability of the stars at the clusters.

Qualitative results are similar as in Perren et al. (2020, their figures 10 and 6, respectively). The stars with the highest probabilities show a narrow main sequence in NGC 4349 with a turn-off point at G≈12 and a few stars in the red giant zone. The weighted average of the parallaxes is 0.498 ± 0.0297 mas compared with mean value of 0.487 mas from Perren et al. (2020). On the other hand, vdBH 85 presents more scattered parallaxes in high G magnitudes, but proper motions are very tight. This is not rare at all, uncertainties in parallaxes from GAIA DR2 increase with the distances of the stars and with their faintness. CDM shows a cluster turn-off at G≈17 with a width main sequence. The weighted average of the parallaxes is 0.164 ± 0.050 mas, while the mean value given by Perren et al. (2020) for vdBH 85 is 0.148, in good agreement with ours ($\sim 0.3\sigma$).

Chapter 4

Solving the distance discrepancy for the open cluster NGC 2453

The OC NGC 2453 is of particular importance since it has been considered to host the PN NGC 2452, however their distances and radial velocities are strongly contested. A complete discussion about this pair can be seen in sec. 2.1. In order to obtain a complete picture of the fundamental parameters of the OC NGC 2453, eleven potential members were studied. The results allowed us to resolve the PN NGC 2452 membership debate. RVs for the 11 stars in NGC 2453 and the PN were measured and matched with *Gaia* DR2 to estimate the cluster distance (sec. 3.3.1 and 3.3.4). In addition, we used deep multi-band UBVRI photometry (sec. 3.2.1) to get fundamental parameters of the cluster via isochrone fitting on the most likely cluster members, reducing inaccuracies due to field stars.

4.1 Results

The RV distribution of our program stars is shown in Fig. 4.1, while the proper motions drawn from the *Gaia* DR2 catalog are plotted in Fig. 4.2. Almost half of the RVs are comprised between 60 and 90 km s^{-1}, where previous estimates of the cluster RV are found (MF; MB14), while most of the program stars in the proper motion diagram cluster around $(\mu_\alpha \cos\delta, \mu_\delta) \approx (3.5, -2.5)$ mas yr^{-1}. The distances derived from *Gaia* parallaxes are also listed in Table 3.1, and they are in the range 4.2-5.4 kpc for most of the targets.

The very high RV (103±5 km s^{-1}) and small distance ($1.2^{1.2}_{1.1}$ kpc) of the star MSP 57 indicate that this is probably not a cluster member. The targets NGC 2453 16 and MSP 211 are also suspected to be field stars due to their low RV (RV=16±2 and 18±8 km s^{-1}, respectively), and for the former this conclusion is reinforced even by

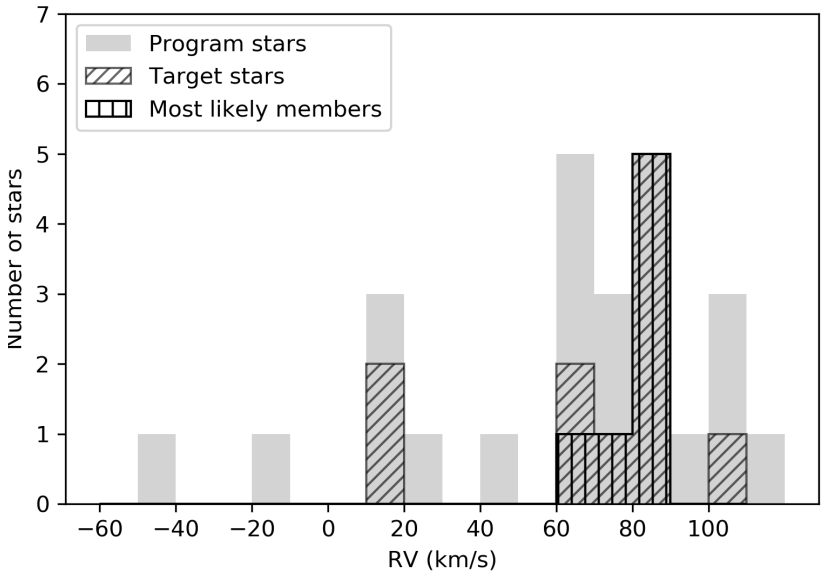

Figure 4.1: Radial velocity distribution for program and target stars of NGC 2453.

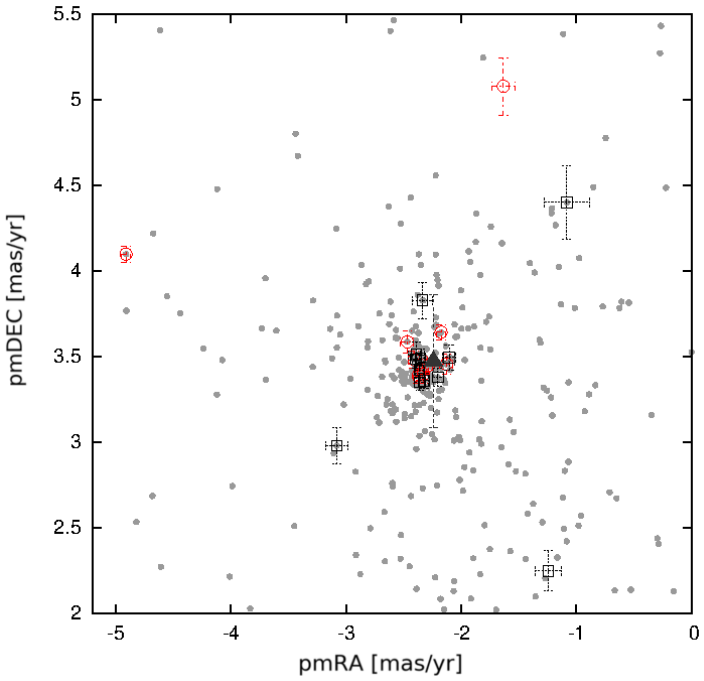

Figure 4.2: Proper motion of stars within 2′.5 of the NGC 2453 center (gray points), from the *Gaia* DR2 catalog. The open red circles and black squares show the position of the target and additional stars, respectively. The triangle indicates the MF54 star.

a discrepant distance and proper motion. In addition, NGC 2453 55 lies far from the bulk of our sample in the proper motion plot, although its RV is compatible with it, and its uncertain distance does not provide additional information. These four stars were therefore labeled as "non-member" (NM) in Table 3.1, and excluded from further analysis. We are thus left with seven stars whose RVs, distances, and proper motions are very consistent, and these are considered "Most Likely Members" (MLM). The velocities for MLM range from 69 ± 4 km s^{-1} to 89 ± 7 km s^{-1}. Their RV distribution is shown with a vertically striped area in Fig. 4.1.

The RVs of stars in the field of NGC 2453 were previously measured by MB14 using CCF from the H_α line. The authors estimated RV=73±5 and 66±8 km s^{-1} for TYC 6548-790-1 and MSP 111, respectively, in agreement with this work despite the large uncertainties. On the other hand, their result for MSP 57 (RV=70±9 km s^{-1}) disagrees with ours. The authors considered this star as a probable cluster member, but new data from *Gaia* DR2 locate it at about 1.2 kpc, too close for an association with the cluster, and its membership is not supported. On the other hand, MB14 classified the star MSP 159 as a nonmember, because its proper motion from the PPMXL catalog (Roeser et al., 2010) was clearly offset from the bulk of their sample. However, the accurate measurements from the *Gaia* DR2 catalog indicate a proper motion consistent with MLM stars, along with compatible RV and distance. Regarding the red giant star TYC 6548-790-1, Mermilliod et al. (2001) and *Gaia* DR2 obtained RVs of 85.2 ± 0.3 km s^{-1} and 85.5 ± 0.3 km s^{-1}, respectively, in good agreement with ours. We added the star NGC 2453 54 (hereafter MF 54) to our sample both in Table 3.1 and Fig. 4.2, although its RV was measured by Moffat and Fitzgerald (1974) but not by us. We return to this object in Sect. 4.2.

Finally, the RV of NGC 2453 was computed using target stars labeled as MLM. We found a weighted mean of RV=78 ± 3 $km\,s^{-1}$, where the uncertainty is the statistical error on the mean. Table 4.1 compares our result with those available in the literature and reveals that our estimate differs from previous ones. These latter however were obtained from only one or two stars, whose cluster membership was inevitably uncertain. Our result, on the contrary, is based on a sample of seven stars with consistent RVs, proper motions, and parallax-based distances.

From the *Gaia* measurements for our program stars, the cluster distance and proper motion can also be estimated. Despite the large errors on distances, the modal values of all MLM stars are close to each other and they differ less than their respective uncertainties, suggesting that the latter could have been overestimated. We adopted the weighted means of MLM stars and the respective errors-on-the-mean as best estimates of the cluster value and their uncertainties, respectively, obtaining $d = 4.7 \pm 0.2$ kpc, $\mu_{\alpha^*} = -2.30 \pm 0.04$ mas yr^{-1}, and $\mu_\delta = 3.47 \pm$

Table 4.1: Literature results for the RV of the PN NGC 2452 and the OC NGC 2453.

PN NGC 2452

Literature	RV (km s^{-1})
Wilson (1953)	68.0 ± 2.5
Meatheringham et al. (1988)	62.0 ± 2.8
Durand et al. (1998)	65 ± 3
Literature Average	65 ± 2
This Work	62 ± 2

OC NGC 2453

Literature	RV (km s^{-1})	Number of stars
Moffat and Fitzgerald (1974)	67 ± 14	1
Moni Bidin et al. (2014)	68 ± 4	2
This Work	78 ± 3	7

0.03 mas yr^{-1}.

4.1.1 Fundamental parameters

NGC 2453 has a great record of observations, but its fundamental parameters have proven difficult to establish, in part because of the complex mix of stars at different distances and reddening lying along the line of sight.

In this work, we overcame the problems of field contamination estimating the cluster distance from the parallax-based *Gaia* distances of spectroscopically confirmed members. With this information, we can thus determine the age and reddening of the system from isochrone fitting of our $UBVRI$ photometry, relying again on the constraints provided by the *Gaia* database and our spectroscopic results. PARSEC + COLIBRI isochrones (Marigo et al., 2017), with solar metallicity ($Z_{\odot}$=0.0152) were used in this process.

The upper panels of Fig. 4.3 show the $V-(B-V)$ CMD and the $(U-B)-(B-V)$ Two-color diagram (TCD) of the cluster area. MLM stars have been depicted as black circles. The TCD (top-right panel) reveals the presence of at least two groups of stars with very different reddening. To identify the cluster sequence, we selected stars with *Gaia* proper motion within 2σ of the cluster value (identified as the mean of the MLM stars in Table 3.1), with proper motion error lower than 0.1 mas yr^{-1}, and *Gaia* distance close to $d = 4.7 \pm 0.2$ kpc. These stars are depicted in Fig. 4.3 as open circles. To identify foreground stars, we also selected those whose distance confidence interval had an upper edge (upper index in Table 1) lower than 3.5 kpc, and we indicated them with black dots in the diagrams. Indeed, most of these

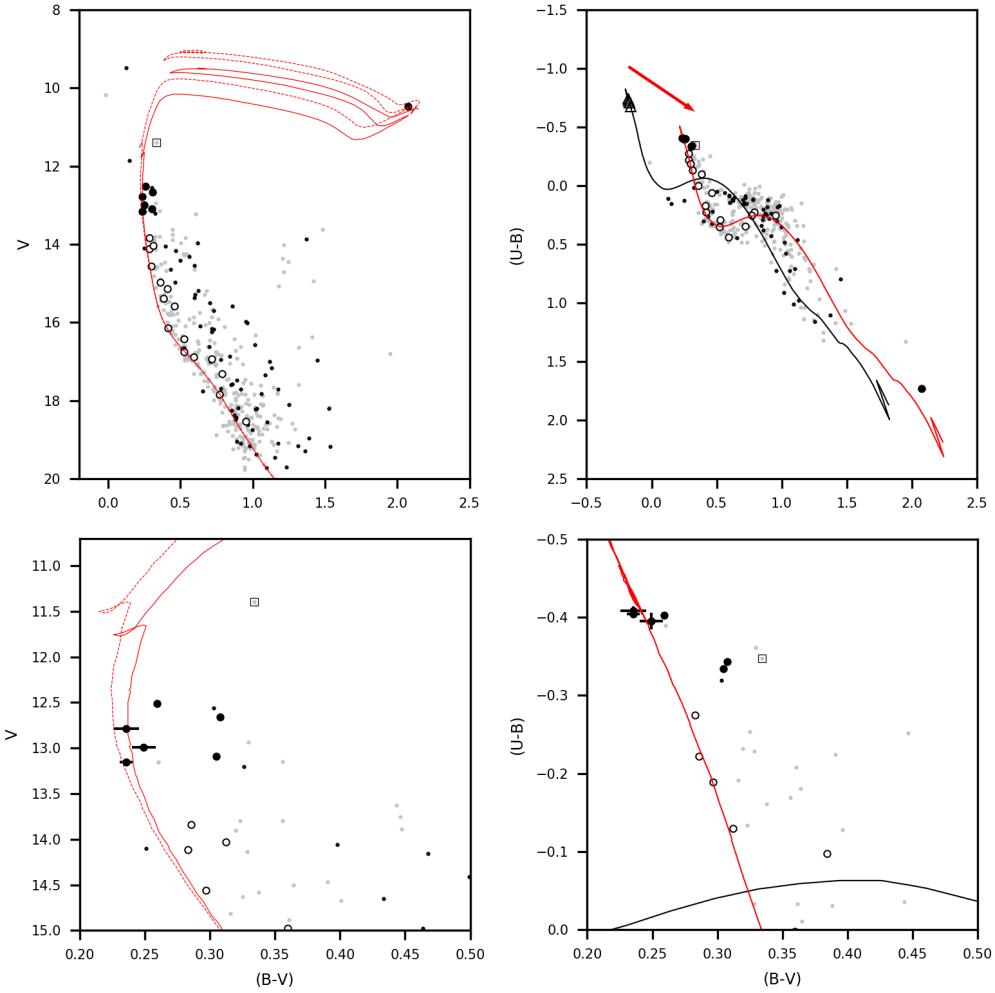

Figure 4.3: CMDs and TCDs of NGC 2453. *Left panels*: The V-$(B-V)$ CMD. Dashed and solid lines depict isochrones of solar metallicity of 40 Myr and 50 Myr, respectively, shifted in magnitude for a distance of 4.7 kpc. *Right panels*: $(U-B)$-$(B-V)$ TCDs. Black and red lines depict intrinsic and reddened isochrones (E_{B-V} = 0.42), with solar metallicity, respectively, and the arrow shows the reddening direction. *Bottom panels*: Zoomed region of the upper panels around the MLM stars. Light gray dots indicate the stars in the field along the line of sight of the cluster, black filled circles show the MLM stars, and open circles indicate stars with proper motions within 2σ of the cluster. Black empty dots are stars with upper distance errors $\leq$3.5 kpc from *Gaia* DR2, and the star in the square is MF54. PARSEC + COLIBRI isochrones from Marigo et al. (2017) have been fitted to MLM stars.

stars are better described by a less reddened sequence than the bona-fide cluster members (open circles), although a few field stars might still be contaminating the latter sample. The brighter MLM stars and the additional open circles thus identify the cluster loci in the TCD.

The intrinsic theoretical isochrone is shown in the TCD of Fig. 4.3 as a black solid curve, while the red one indicates the same model after applying the final reddening solution. The triangles on the intrinsic isochrone correspond to the points at the same temperature range as our spectroscopic estimates for MLM stars (see Table 4.2), that is, $\log(T_{\rm eff}) = [4.23, 4.25]$.

We determined the color excesses E_{U-B} and E_{B-V} from the difference of the average color index for MLM stars (black circles), and for isochrone points at the same temperature (black triangles). We thus derived the slope E_{U-B}/E_{B-V} of the reddening vector in the TCD. The bottom-right panel of Fig. 4.3 shows a zoomed region of the TCD, focused on the MLM stars, where it appears clear that three MLM stars (namely MSP 111, MSP 112 and MSP 132) are found at redder colors than the others, possibly due to stellar rotation effects (Bastian and De Mink, 2009) or the presence of a cooler companion (Yang et al., 2011). Table 4.2 shows that these stars as indeed fast rotators. As a consequence, only the slow-rotating MLM stars were used in the process. We obtained a slope of $E_{U-B}/E_{B-V} = 0.78 \pm 0.09$, with $E_{B-V} = 0.42 \pm 0.01$. This result agrees well with Turner (2012), who established localized reddening laws described by $\mathrm{E}_{U-B}/\mathrm{E}_{B-V} = 0.77$ and $R_V = 2.9$ for the third galactic quadrant (Turner et al. 2014; Carraro et al. 2015), which is adopted here. The resulting extinction is $A_V = 1.22 \pm 0.03$ mag. This result, together with the distance derived in this work, fits the general Galactic extinction pattern determined by Neckel and Klare (1980) very well, even though the authors did not study the NGC 2453 region (l=343°, b=−1°). According to their work, the Galactic region near the cluster line-of-sight (l=342°, b=0°) has an extinction $A_V \approx 1$ up to ∼5 kpc, and it increases at a further distance to $A_V \approx 2$ at about 6 kpc and beyond. In contrast, the next region closest to the cluster area (l = 345°, b = 0°) shows an extinction $A_V \approx 1.5$ between 2 and 6 kpc, with slight variations at both ∼3.5 and ∼5.0 kpc. These results seem to be confirmed using the 3D map of interstellar dust reddening* describe by Green et al. (2018). The map shows a distance of $d = 5.0$ kpc for a reddening of $\mathrm{E}_{B-V} = 0.42 \pm 0.03$ in the same line of view of the cluster, in great agreement with our results.

Eventually, with the distance and reddening found so far, we fitted slow rotator MLM and bona-fide cluster stars in the CMD, with age as the only free parameter.

*http://argonaut.skymaps.info/

Table 4.2: Derived parameters of temperature, gravity and rotational velocity for the MLM stars of the OC NGC 2453.

Star	V	$(B-V)$	$(U-B)$	$T_{\rm eff}$ K	$\log g$ dex	$v \cdot \sin i$ km s^{-1}
TYC 6548-790-1	10.47	2.08	1.73	—	—	—
MSP85	13.15	0.24	−0.40	17700 ± 200	3.92 ± 0.03	30
MSP111	12.66	0.31	−0.34	16700 ± 300	3.63 ± 0.06	90
MSP112	13.09	0.30	−0.33	16600 ± 300	3.79 ± 0.06	150
MSP126	12.99	0.25	−0.40	17800 ± 300	3.95 ± 0.06	20
MSP132	12.51	0.26	−0.40	16600 ± 200	3.90 ± 0.03	160
MSP159	12.79	0.24	−0.41	17700 ± 300	3.86 ± 0.06	40

Table 4.3: Parameters estimated for NGC 2453

Reference	$E_{(B-V)}$	τ (Myr)	d (kpc)
Seggewiss (1971)	0.48	–	1.5
Moffat and Fitzgerald (1974)	0.47 ± 0.04	40	2.9 ± 0.5
Gathier et al. (1986)	0.49 ± 0.01	–	5.0 ± 0.6
Mallik et al. (1995)	0.47	25	5.9 ± 0.5
Moitinho et al. (2006)	–	40	5.25
Hasan et al. (2008)	0.47	200	3.3
Cantat-Gaudin et al. (2018a)			4.3
González-Díaz et al. (2019) (This Work)	0.42 ± 0.01	40-50	4.7 ± 0.2

We find that an age in the range $\tau \approx 40 - 50$ Myr is the best solution, which accurately reproduces the observed sequence of stars (see left panel of Fig. 4.3).

4.2 Discussion

4.2.1 Cluster parameters

Our estimates of reddening, distance, and age for NGC 2453 are compared with literature results in Table 4.3. All previous studies were purely photometric, with the exception of Cantat-Gaudin et al. (2018a), who used Gaia parallaxes, while we joined information from optical spectroscopy, UBV photometry, and data from the *Gaia* mission.

The distance and age derived here are roughly compatible with those found by Moitinho et al. (2006, 5.23 kpc and 40 Myr), but the former is closer to the result of Gathier et al. (1986, $d = 5.0 \pm 0.6$ kpc). However, the reddening derived by Gathier et al. (and in general, all estimates in the literature) is ∼15% larger than ours. These authors based their results on five stars previously classified as cluster members by MF, namely NGC 2453 7, 8, 28, 30 and 45 (Gathier, 1985). However,

Gaia distances for the stars 28 and 30 ($1.1^{1.2}_{1.1}$ kpc and $7.8^{9.5}_{6.4}$ kpc, respectively) disagree with the estimates of Gathier et al. (∼3.9 and 4.4 kpc, respectively), and they are much larger than the average value for our MLM stars. This suggests that some stars used in previous works to constrain the cluster parameters may not have been cluster members. Gathier found that the color excess E_{B-V} of these two stars is the same (∼ 0.51), in spite of the huge distance discrepancy reported by *Gaia*. On the other hand, Mallik et al. (1995) showed that a reddening of 0.47, as proposed by MF, produces reasonably good isochrone fits on the CMD. However, our analysis shows that such high values accurately fit the color of a group of stars that are displaced to redder colors than the rest of the MS, possibly due to their fast rotation or to the presence of a cool companion. However, our distance only agrees with Cantat-Gaudin et al. (2018a) within 2σ, being this at a distance closer than ours.

We indicated the evolved giant star MF54 observed by MF as an empty square in Fig. 4.3, and as a black triangle in Fig. 4.2. These authors classified MF54 as a cluster member based on its spectral class (B5V:k) and a RV of 67 ± 14 km s^{-1}. Its *Gaia* DR2 proper motion and distance agree with the mean values obtained for the cluster (see Table 3.1), despite the large error bars. However, the fractional parallax error is extremely large (∼ 118%), and it contrasts with the typical errors for MLM stars ($\lesssim 25\%$), which produce less reliable distance measurements (Bailer-Jones, 2015). Due to the high uncertainties in the measurements, the membership of MF54 is not completely clear, and therefore we did not take it into account during the isochrone fit procedure. Indeed, the fact that the error on the parallax is much larger for this star despite it being so bright, implies that it must be farther away. Similarly, the red giant star TYC 6548-790-1 was also excluded from the fit. This star could be variable (see MB14), and as a consequence its photometric data may not be completely reliable. Mallik et al. (1995) showed that the inclusion of one or both of these two stars during the isochrone fitting procedure can change the cluster age from 15 to 40 Myr.

In Fig. 4.4 we analyze the radial density profile of the OC. Only stars with proper motion within 3σ of the cluster value were selected. It is clear that the cluster population dominates the background up to approximately r∼ $8' - 10'.5$. The angular distance between PN NGC 2452 and the center of the OC NGC 2453 is $8'.5$, that is, within the coronal extent of the OC.

4.2.2 Planetary nebula membership

Gathier et al. (1986) derived the reddening of the PN NGC 2452 as $E_{B-V} = 0.43 \pm$

0.05, which is virtually the same found by us for the cluster. Nevertheless, the reddening-distance method used by Gathier et al. (1986) for the PN leads to a distance of $d_{PN} = 3.57 \pm 0.47$ kpc, which is confirmed with the more modern dust map by Green et al. (2018) ($d_{PN} = 3.70$ kpc). Other authors adopted different methods, and found even smaller values (see, e.g., Acker, 1978; Maciel and Pottasch, 1980; Daub, 1982; Stanghellini et al., 2008).

Distance and proper motions from *Gaia* DR2 to PN NGC 2452 are not particularly reliable ($d_{PN} = 2.4^{3.4}_{1.8}$ kpc, μ_α=-2.5±0.2 mas yr^{-1} and μ_δ=3.5±0.2 mas yr^{-1}). Even though the central star for NGC 2452 was a target of various photometric studies (e.g., Ciardullo and Bond, 1996; Silvotti et al., 1995), and its coordinates match those from *Gaia* very well, Kimeswenger and Barría (2018) restrict the identification to PNe with photometric colors in the range $-0.65 \leq (BP - RP) \leq -0.25$. Outside this interval, *Gaia* DR2 cannot identify the central star correctly due to contamination of the H$_\alpha$+[NII] emission line of the PN envelope. The color index for NGC 2452 is $(BP - RP) = 0.07$, which is highly reddened. Therefore, any identification would most likely be incorrect. In contrast, recently Chornay and Walton (2020a) reported the identification of the central star via *Gaia* DR2 with a parallax of 0.40 ± 0.11 mas equivalent to a Bailer-Jones distance of $2.5^{5.3}_{1.9}$ kpc.

Figure 4.5 shows that the RV of PN NGC 2452, along with the distance proposed by Gathier et al. (1986), closely match the distance–RV profile of the Galaxy arm in the Puppis direction. The profile was obtained assuming the rotation curve of Brand and Blitz (1993), the solar peculiar motion of Schönrich et al. (2010), $R_\odot = 8.0 \pm 0.3$ kpc, and $V_{\rm LSR} = 220 \pm 20$ km s^{-1}. In contrast, the cluster NGC 2453 is consistent in both RV and distance computed here to be just behind NGC 2452, and possibly a member of the Perseus arm, as can be seen in Fig. 2 of Moitinho et al. (2006).

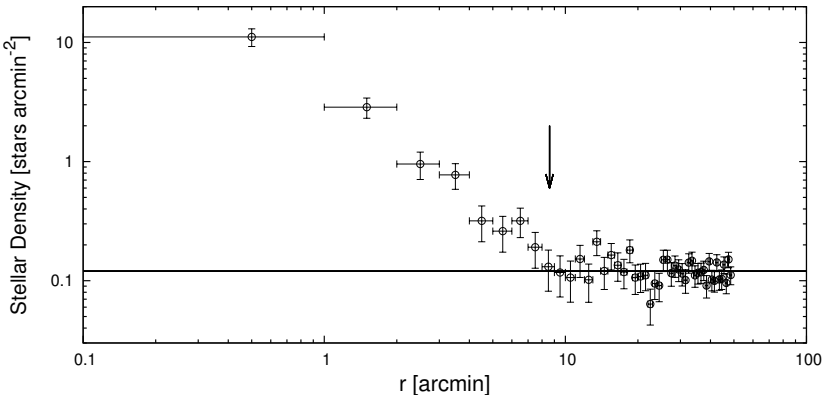

Figure 4.4: Radial density profile constructed for NGC 2453 using proper motions from *Gaia* DR2. The angular distance of NGC 2452 is indicated with an arrow. The f $'$.

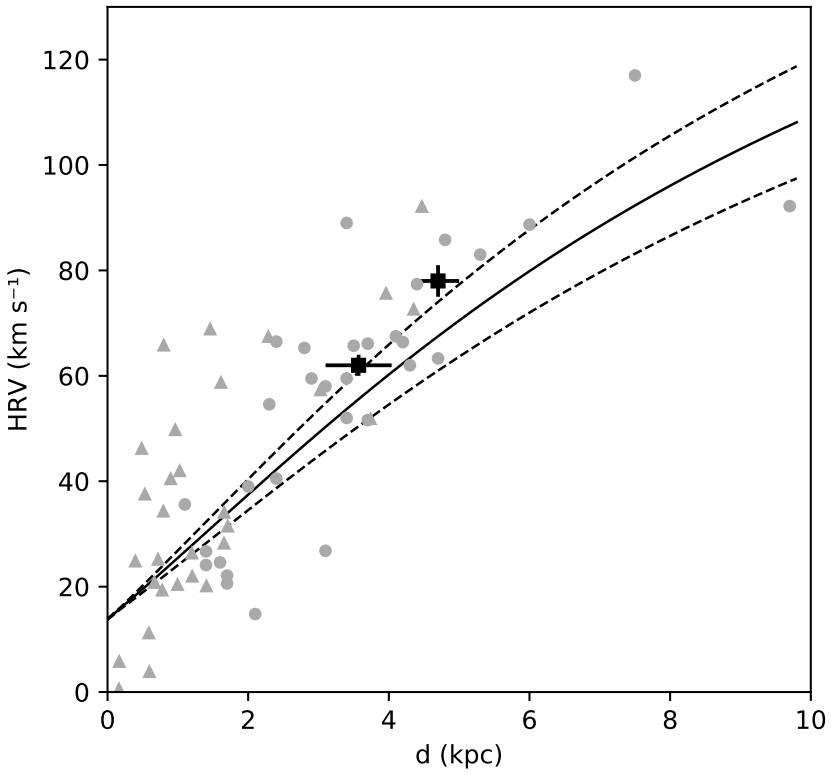

Figure 4.5: Distance–RV plot in the direction of Puppis. The solid curve shows our theoretical model based on Galactic rotation, with the dashed curves used to indicate the 1σ propagation errors. Gray circles are classical Galactic Cepheids from Mel'nik et al. (2015) in the third quadrant with Galatic latitudes $-2° < b < 2°$, while triangles are bright stars with available RVs from *Gaia* DR2 with $242.5° < l < 243.5°$ and $-1° < b < 1°$. Squares with error bars show the position of NGC 2452 and NGC 2453.

Chapter 5

Untangling the neighborhood of the Open Cluster Lynga 15

Lynga 15 is an OC whose nature is disputed. In its vicinity lies the PN Hf 69, which could be a potential member of Lynga 15. However, five additional clusters appear to be located within just 20′ around: Loden 467, Loden 465, Stock 14, Loden 466 and Bica 5. A more complete discussion about this pair can be seen in sec. 2.2. A density contour map of the FOV along with the equatorial and Galactic coordinates are shown in Fig. 5.1 and Table 5.1, respectively. This chapter aims in two directions: 1) establishing the fundamental parameters and real nature of the open clusters in the neighborhood of Lynga 15 and 2) assessing the potential member-

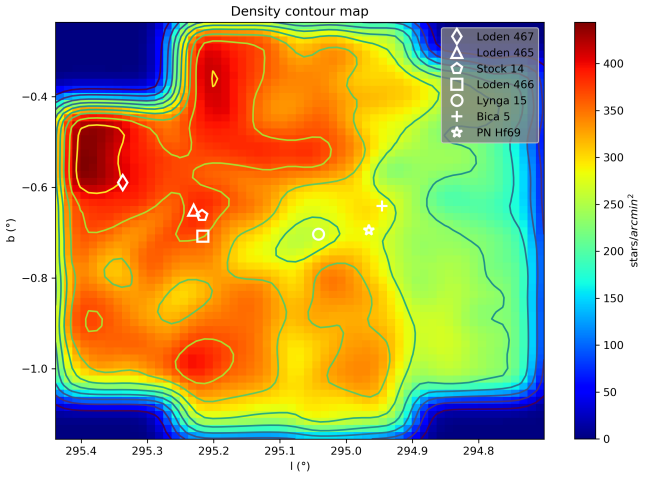

Figure 5.1: Density contour map for the field of view of the VVV data covering an area of $\sim 1° \times 1°$ centered in the OC Lynga 15. Symbols show six OCs locations as well as the PN Hf 69.

Table 5.1: Coordinates of the objects.

ID	RA_{J2000} (hh:mm:ss)	DEC_{J2000} (dd:mm:ss)	l (deg)	b (deg)
Loden 467	11:44:57.9	-62:28:38	295.3372	-0.5898
Loden 465	11:43:55.5	-62:30:32	295.2293	-0.6511
Stock 14	11:43:48.0	-62:31:00	295.2173	-0.6624
Loden 466	11:43:41.4	-62:33:38	295.2165	-0.7080
Lynga 15	11:42:14.4	-62:30:36	295.0419	-0.7030
Bica 5	11:41:34.8	-62:25:30	294.9457	-00.6414
PN Hf 69	11:41:37.4	-62:28:54.4	294.96571	-00.69478

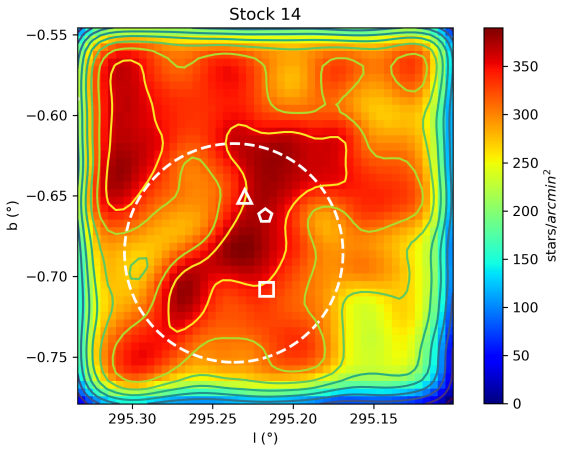

Figure 5.2: Density contour map for Stock 14. Symbols are the same as in Fig. 5.1, but centered within a radius of 7′ around the cluster. The dashed circle marks the selected area for the study of the cluster.

ship of the Hf 69 to the clusters. JHKs photometry from VVV was drawn at the FOV of $\approx 1\,^{\circ} \times 1^{\circ}$ around Lynga 15 (see sec. 3.2.2). Additional data was obtained from Gaia DR2 in the same FOV. Gaia data were analyzed using an algorithm that assigns higher likelihood to tighter stars in the parameter space in order to obtain proper motions and parallaxes for each cluster (sec. 3.4.2). Photometric distances, reddening and $\log(\tau)$ were fitted using VVV data. Radial velocity (RV) measurements were carried out for 11 stars in Lynga 15 and the PN Hf 69 in order to assess potential membership.

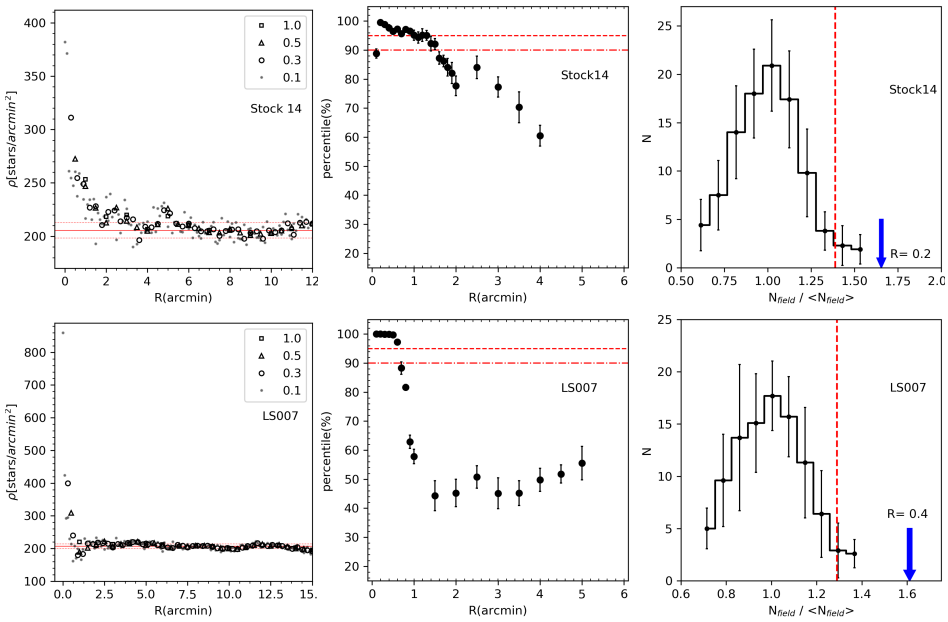

Figure 5.3: *Left panels*: Radial density profiles for the OC Stock 14 (top panels) and LS 007 (bottom panels). The symbols represent different ring apertures. Solid and dashed lines show the background density and its correspond 1σ uncertainties, respectively. *Middle panels*: Average percentiles of $N_{over}/\langle N_{field}\rangle$ in $N_{field}/\langle N_{field}\rangle$ distributions against radius. Error bars show uncertainties after ten runs. Dashed and dash-dot lines represent the 95% and 90% percentile, respectively. *Right panels*: Distribution of $N_{field}/\langle N_{field}\rangle$ for the field stars compared to the center cluster area (blue arrow). Vertical dash-dot line marks the 95^{th} percentile locus. The radius value in arcmins that maximizes the percentile is shown.

5.1 Stock 14, Loden 465 and Loden 466

OCs Stock 14, Loden 465 and Loden 466 are an interesting group located at about $10'$ west from Lynga 15. A density contour map can be seen in Fig. 5.2. The most prominent of the group is the well studied OC Stock 14 (pentagon symbol). Stock 14 is known to be a loose grouping of blue stars whose brightest member is HD 101947, a long-period Cepheid variable. At approx $1'$ from Stock 14, OC Loden 465 (triangle symbol) has been identified, and a little further south, Loden 466 (square symbol). An extended and irregular density zone is easily visible in the center of the field, widening from north to south. The figure shows that Stock 14 lies at the center of the dense irregular zone, while locations for the Loden's clusters appear to be on the edges. However, a density lump lying near the south of Stock 14 at b ≈-0.68° and another one at b ≈-0.71°can also be seen. These lumps could indicate the location of two different clusters or simply be the shapeless cluster Stock 14. The grid of RDPs showed the dense zone at b ≈-0.68° as the most prominent, and we chose

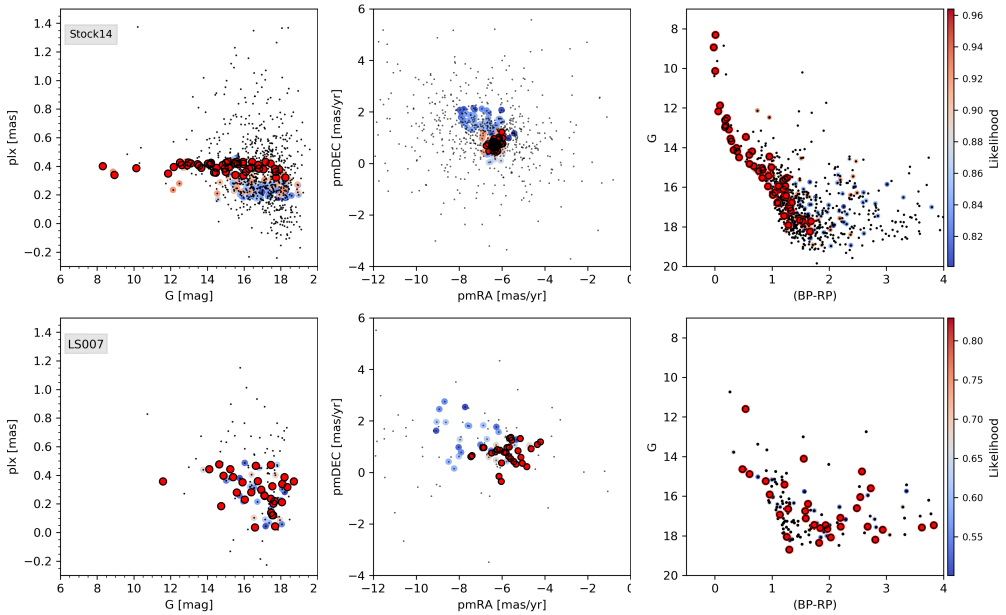

Figure 5.4: From left to right: parallax vs apparent magnitude G, Proper motions, and G vs (BP-RP) diagrams for stars of the open clusters Stock 14 (top row) and LS 007 (bottom row). Black dots represent stars within the cluster radius from Gaia DR2. Color circles depict the membership probability of the stars at the clusters.

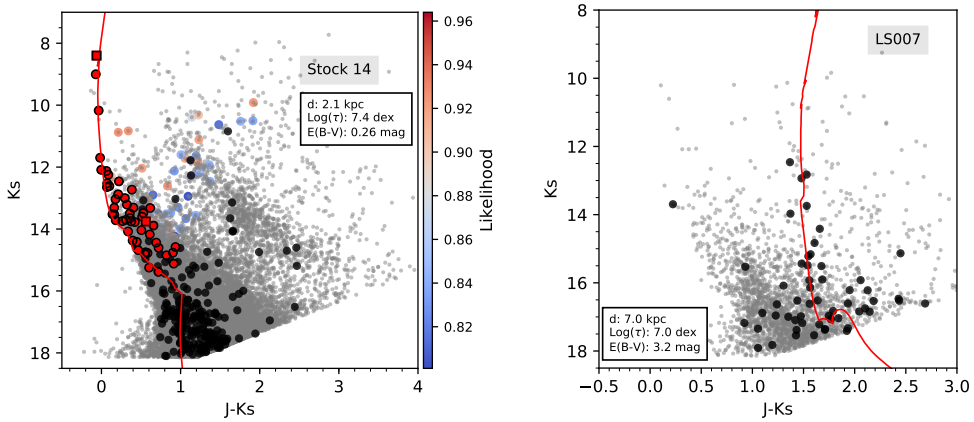

Figure 5.5: Ks against J-Ks CMD from VVV data within the cluster area (gray dots). Color circles depict cross-matched stars for most likely members from Gaia DR2 data. Black circles show stars in an inner cluster area. PARSEC+COLIBRI isochrones from Marigo et al. (2017) have been fit (solid red line). *Left panel*: Stock 14, black dots within r $\leq 30''$, and isochrone $log(\tau)$=7.4 dex. *Right panel*: LS 007, black dots within r $\leq 10''$, and isochrone $log(\tau)$=7.0 dex.

it as the center of Stock 14. Northeast of Stock 14 (at l=295.17°, b=-0.57°) lies the cluster candidate LS 007. The cluster was observed for the first time by Barbá et al. (2015), and it is barely noticeable on the density map due the small angular size.

Figure 5.3 shows the result of density analysis of Stock 14 and LS 007. Left panel contains the final RDPs for each object. The innermost density for Stock 14 rises beyond 350 stars per square arcmin, while for LS 007 it exceeds 800. Stock 14 reaches $5'$ before fluctuating as the field. The cluster area is illustrated as a dashed circle in Fig. 5.3. In contrast, density for LS 007 is noticeable but it falls rapidly until it reaches the field in about $1'$. In order to evaluate the statistical significance of the number of stars as a function of the overdensity radius (R_{over}), we show in the middle panel of Fig. 5.3 the distribution of the percentile of $N_{over}/\langle N_{field}\rangle$ in $N_{field}/\langle N_{field}\rangle$ against radius, as was described in section 3.4.1. A density exceeding at least once the 95^{th} percentile of the distribution can indicate presence of a real cluster. Below that value, it could indicate a probable fluctuation of the density field. In fact, Stock 14 shows, within the error bars, that the overdensity stays above the 95% of the distribution until reaching a radius of $1'.5$; then, it decreases constantly until 78% at $2'$ and then increases until 85% at $2'.5$. After that, it decreases slowly until reaching 60% at $4'$. On the other hand, distribution for LS 007 stays close to the 100% until $0'.6$, and then decreases rapidly until reaching 44% at $1'.5$. Results agree with the RDPs in the left panels. In addition, the right panel in Fig. 5.3 represents the position of $N_{over}/\langle N_{field}\rangle$ with respect to the distribution of $N_{field}/\langle N_{field}\rangle$ for the radius with the maximum percentile. Density of LS 0007 in radii $\leq 0'.4$, is as significant as the density of the OC Stock 14 at a radius of $0'.2$ with respect to the field.

The results of applying the procedure described in sec. 3.4.2 for the data drawn from Gaia DR2 on Stock 14 and LS 007 can be seen in Fig. 5.4. Top panels belong to OC Stock 14. The color circles represent the MLM of the cluster with likelihoods greater than 92%. Parallax against G-magnitude (left panel) and proper motions diagrams (middle panel) show a very tight set of stars in the parameter space with a weighted average parallax of $\varpi = 0.386 \pm 0.031$ mas, and proper motion of $\mu_{\alpha^*} = -6.290 \pm 0.162\,\mathrm{mas{\cdot}yr^{-1}}$ and $\mu_\delta = 0.761 \pm 0.148\,\mathrm{mas{\cdot}yr^{-1}}$ for the right ascension and declination respectively, where uncertainties are the statistical error on the mean. Right panel in Fig. 5.4 shows how MLMs follow a well defined main sequence. Results are in good agreement with Cantat-Gaudin et al. (2018b) and Liu and Pang (2019). In fact, the authors found a set of (ϖ, μ_{α^*}, μ_δ) values for Stock 14 of (0.385 mas, $-6.388\,\mathrm{mas{\cdot}yr^{-1}}$, $0.714\,\mathrm{mas{\cdot}yr^{-1}}$) and ($0.379 \pm 0.020$ mas, $-6.375 \pm 0.252\,\mathrm{mas{\cdot}yr^{-1}}$, $0.788 \pm 0.308\,\mathrm{mas{\cdot}yr^{-1}}$), respectively.

PARSEC+COLIBRI isochrone of solar metallicity for Stock 14 was fit in the Ks against (J-Ks) diagram in Fig. 5.5 (left panel). Isochrone was fitted using the weighted average value of the parallax as first guess for the distance using the Bailer-Jones method ($2.6^{3.0}_{2.3}$ kpc *), and then fitting reddening and age. Gaia data for MLM were cross-matched with VVV data within a radius of 0.3″. Three stars were not found in VVV data, one of them with G=8.3 and the other two with G $>$ 15. They were drawn from 2MASS and represented as red squares following the transformations given in Soto et al. (2013). One of these stars was not resolved in the H and Ks bands of 2MASS, thus, it was not taken into account. Left panel in Fig. 5.5 shows how MLM stars in main sequence appear to spread out below Ks≈13 mag. We fit the isochrone using less reddened stars with highest probabilities, namely, >93% (red circle). An isochrone with a photometric distance of d=2.1 kpc, E(V-B) = 0.26 mag and $\log(\tau) = 7.4$ dex was finally found. Kharchenko et al. (2016) reported a distance of d = 2454 pc, reddening E(B-V) = 0.312 mag and $\log(\tau) = 6.8$ dex, while Sampedro et al. (2017), d=2399 pc, E(B-V)=0.21 mag and $\log(\tau)$=7.3 dex. Our photometric distance is below those of the authors, while $\log(\tau)$ agrees with that for Sampedro et al. (2017). However, reddening lies in the middle of the values reported by these authors.

Dispersion observed at the main sequence in Fig. 5.5 (left panel) could be caused by differential reddening. Fig.5.6 shows the map of Galactic dust reddening and extinction for the set of clusters in the vicinity of Lynga 15, obtained through the interactive Spitzer Service Program†. Pixel intensity represents the value of total reddening in the line of sight estimated from Schlegel et al. (1998) and recalibrated by Schlafly and Finkbeiner (2011). The figure shows that the zone in which Stock 14 is located suffers from extremely high reddening in the line of sight. Moreover, the total reddening in the cluster direction is E(B-V) ≈ 10, implying $A_V \sim 31$ mag (we will return to this below). The reddening along this line of sight is expected to become larger than E(B-V)≈ 0.3 beyond ∼ 2.5 kpc (Neckel and Klare, 1980, their field 148), so our measurements to the cluster roughly agree with this result, indicating the cluster could be affected by high differential reddening.

Fig. 5.7 shows the distribution of stars within a radius of 30′ centered at Lynga 15, from the Gaia DR2 data. Light gray dots depict the distribution of stars sharing the same average proper motion found for the cluster, while the dark ones represent the stars sharing the same proper motion as before along with the parallax (within ±0.2 mas·yr^{-1} and ±0.1 mas, respectively). Black dots are expected to be

*We recall the notation defined at the end of sec. 3.3.4, where the lower and upper indices correspond to minimum and maximum distances in the error interval of the 5% and 95% quantile, respectively.

†https://irsa.ipac.caltech.edu/applications/DUST/

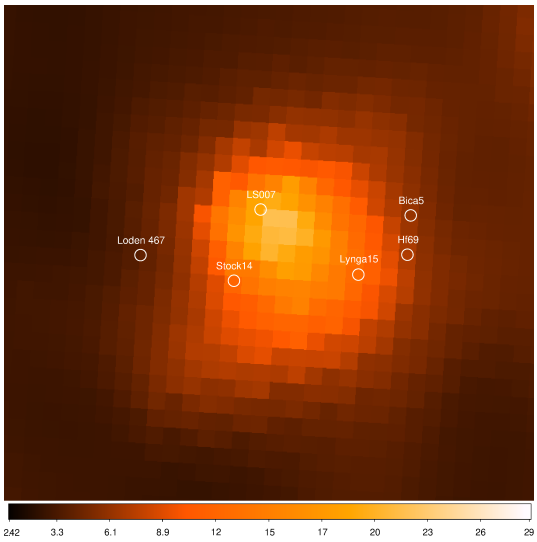

Figure 5.6: Galactic dust reddening for the line of sight of Stock 14. Color bar represents the estimates of E(B-V) from Schlegel et al. (1998). Lighter colors indicate higher extinction. FOV is $\sim 1° \times 1°$.

less contaminated by field stars. Both the gray and black dots show an expected distribution for a cluster, with a prominence in the cluster area (red marks).

Results for LS 007 were more elusive. Bottom panels in Fig. 5.4 did not show a clearly defined cluster in the parameter space. This is corroborated in the G against (BP-RP) diagram where MLM stars are spread across the star distribution. Nevertheless, a different conclusion can be drawn from the Ks vs (J-Ks) diagram in Fig. 5.5 (right panel). Black dots represent stars within a radius of r<10″, that is to say, in the innermost area of the cluster candidate. The dots rise in a vertical way until reaching Ks≈12 mag. Due to the fact that the center area corresponds to a very dense zone, this behavior might not be fortuitous. The black dots in the figure indicate that a young isochrone with $\log(\tau)$=7.0 dex and E(B-V)=3.2 mag can be fit. The distance fitting would correspond to distant cluster with an undefined range, being 7 kpc nearest. It roughly agrees with the interstellar extinction model described by Marshall et al. (2006) in the Galactic direction l=295.25°, b=-0.50°. In fact, a reddening of E(B-V) = 3.2 is equivalent to an extinction of A_{Ks}=1.1 mag, corresponding to a distance of ∼9 kpc. Fig. 5.6 shows that LS 007 is located very close to the highest reddening zone just 1′.3 from the supernova remnant SNR G295.2-00.6, and it is potentially associated with the dark nebula SDC G295.185-0.578 (Barbá et al., 2015). Values for reddening from the extinction map yield a Schlafly and Finkbeiner reddening of E(B-V) ≈ 16 and $A_V \approx 50$ mag. Such high value in extinction in the line of sight could be unreliable. The reddening map is constructed using the 100 μm dust temperature to

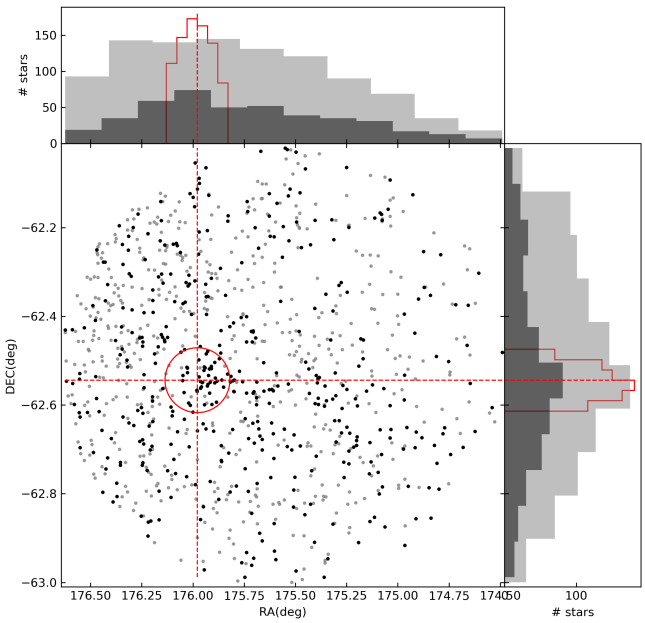

Figure 5.7: Spatial distribution of the stars of the OC Stock 14 from Gaia DR2. Field of view is within an area of 30′ centered in Lynga 15. Light and dark colors represent star distributions whose proper-motion (light), and proper motion along with parallax (dark) are constrained to the same average values as those found for Stock 14 at Fig. 5.4. The red circle and the red line show the area and the center of the cluster, respectively.

derive the extinction along the line of sight. Resolution of the temperature map is ∼1° although the 100-micron intensity map reaches a resolution of 6′.1. Because of this, the proximity of SNR G295.2-00.6 could be contaminating the measurements. As claimed by Schlegel et al. (1998), non-gray extinction due to the presence of a distant supernova would yield strong systematic errors.

Finally, in order to identify a second cluster in the FOV of the Fig. 5.2, we ran the procedure again, but this time removing those stars marked as black dots in Fig. 5.7, i.e., Stock 14 members stars. The procedure did not return any relevant result about stars forming a cluster in that area. But, surprisingly, they showed a group in the area near to Loden 467 (see sec. 5.2), indicating that no other cluster is present in the vicinity of Stock 14.

5.2 Loden 467

OC Loden 467 is a cluster located about 20′ east from Lynga 15 and 11′ east from Stock 14 (see Fig. 5.1). Fig. 5.8 shows the density contour map within a radius of

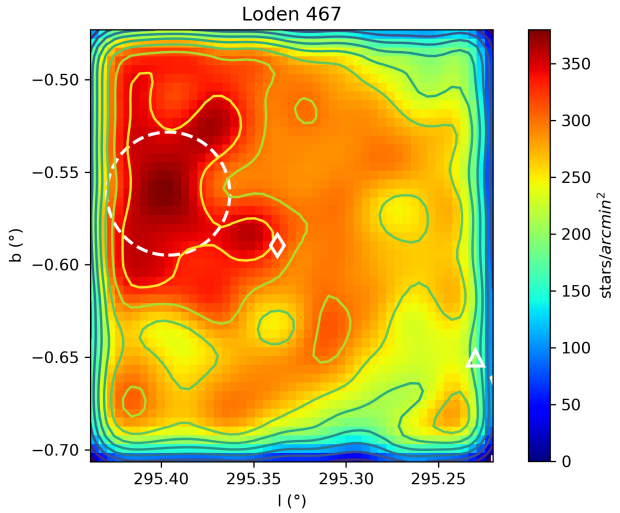

Figure 5.8: Same as in Fig. 5.2, but centered within a radius of 7′ around coordinates of OC Loden 467.

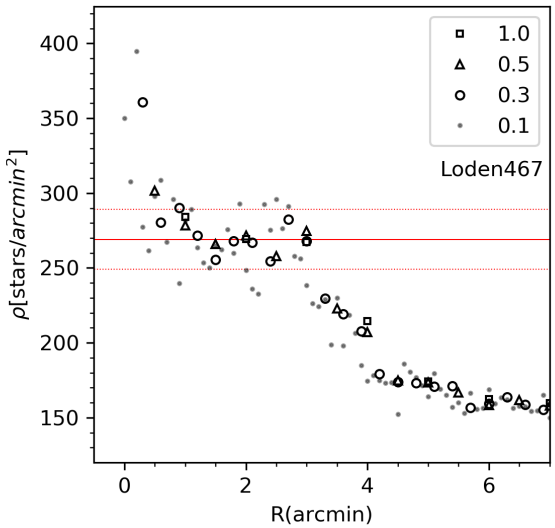

Figure 5.9: Radial density profile for the OC Loden 467, within a radius of 7′.

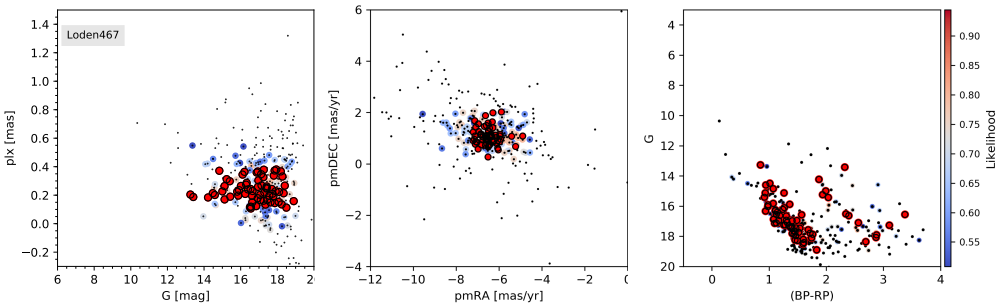

Figure 5.10: Same as in Fig. 5.4 for Loden 467.

7′, centered in the coordinates reported by Lodén (1973) (diamond symbol). The figure shows an overdensity zone east from the diamond symbol at l≈295.41° and b≈-0.56°, reaching about 350 stars·arcmin^{-2}. Fig. 5.1 shows that this zone lies in the area with the highest density of the whole FOV, so we selected the area enclosed within the dashed circle as the cluster area. Due to the fact that the cluster is located on the left edge of our data, it prevents us from knowing the complete structure of the cluster, and it does not allow us to analyse the statistical significance of the overdensity with respect to the surrounding field.

Fig. 5.9 corresponds to the RDP of Loden 467. The edge of the FOV is at 3′, which explains the drop in the density profile beyond that value. In Fig. 5.10 are shown the results of the procedure described in sec. 3.4.2. Left and middle panels show the distribution of MLM (red circles) in both the parallax against G-magnitude and the proper motion diagrams, while the right panel presents the CMD. Although the parallaxes and proper motions were well defined with likelihoods over 90%, the main sequence did not appear to be clear until values greater than 80%, indicating that Loden 467 could be a faint cluster. In fact, CMD shows a turn-off close to G≈16 mag. Qualitative results for Loden 467 look similar to vdBH85 in the right panels of Fig. 3.8. For that kind of cluster, distribution of the stars in parallax vs G diagram fluctuate around a mid value, and the main sequence looks spread. The procedure returned a weighted average parallax of $\varpi = 0.234 \pm 0.076$ mas, and weighted average proper motions of $\mu_{\alpha^*} = -6.457 \pm 0.444$ mas·yr^{-1} and $\mu_\delta = 1.069 \pm 0.332$ mas·yr^{-1}, where the uncertainties are the standard error on the mean. Our results disagree with the proper motion reported by Sampedro et al. (2017), who established values of -9.2 mas·yr^{-1} and -10.0 mas·yr^{-1} for the proper motions at right ascension and declination, respectively. The authors located Loden 467 about 2′.8 away from our coordinates. Nevertheless, we did not find any representative group in the parameter space at those values. On the other hand, Kharchenko et al. (2013) located Loden 476 about 1′.92 from our position, and they found values of -6.90 mas·yr^{-1} and -0.90 mas·yr^{-1} for proper motions at right ascension

and declination, respectively. These results are closer to ours, but proper motions diagrams also do not show any special features at that point. Finally, Liu and Pang (2019) located the cluster at about $4'.5$ from our center, but they found values of $\mu_{\alpha^*} = -6.213 \pm 0.619\,\mathrm{mas{\cdot}yr^{-1}}$ and $\mu_\delta = 1.044 \pm 0.450\,\mathrm{mas{\cdot}yr^{-1}}$ in good agreement with our results. Latter authors also estimated parallax for Loden 467 obtaining a value of $\varpi = 0.285 \pm 0.019$ mas, agreeing with ours only within 2.6σ.

Figure 5.11 shows the color-magnitude diagram Ks against (J-Ks) from VVV data of the stars within a radius of $2'$ from the cluster center (gray dots). MLM found with Gaia were cross-macthed with VVV within 1 arcsec, and they are displayed as color circles. In order to fit the best isochrone, we used the parallax to estimate the Bailer-Jones distance as first guess ($3.9^{7.5}_{2.9}$ kpc), and then we fitted reddening and age. Stars with $r \leq 30''$ from VVV data (black dots) showed a possible main sequence overlapping to MLM at the top. An isochrone with d=3.7 kpc, E(B-V)=0.9 mag and $log(\tau)$=8.8 dex was finally fitted. Reddening agrees with the interstellar extinction model described by Marshall et al. (2006) at the cluster direction. In fact, an extinction of A_{Ks}=0.31 corresponds to a distance of d≈4 kpc. This result also agrees with Neckel and Klare (1980) who found A_V>2 mag for distances >3 kpc. Our results for the cluster show that it is both farther away and older than estimated by Kharchenko et al. (2013) who found d=2569 pc and $log(\tau)$=6.6 dex, but younger than Liu and Pang (2019) with an age of 8.71 Gyr, equivalent to $log(\tau)$=9.9 dex. Distribution of stars sharing the same proper motion (gray dots) and proper motion along with parallax (black dots) are shown in the right panel of the Fig. 5.11. The figure uses intervals of $\pm 0.2\,\mathrm{mas{\cdot}yr^{-1}}$ and ± 0.7 mas around mean values of the parallax and proper motion, respectively. Red circle represents the cluster area, while the red lines, the center. It is possible to notice a group of tight stars emerging from the background within the red circle sharing astrometric parameters, which indicates the presence of a real cluster, although the value for the age found here can be discussed. However, beyond the cluster area, star distribution shows that the field is strongly contaminated. Area northwest of Loden 467 escapes our FOV, but it is completely within the VVV data. More analyzes are required to determine the precise parameters for this cluster.

5.3 Lynga 15

Lynga 15 is an open cluster located near the center of Fig 5.1 (white circle). Density color map for Lynga 15 can be seen in Fig. 5.12. The figures extend to a radius of $5'$, and they are centered at coordinates used by Kharchenko et al. (2013) and Joshi et al. (2016) and reported in Simbad database (see Table 5.1). As can be

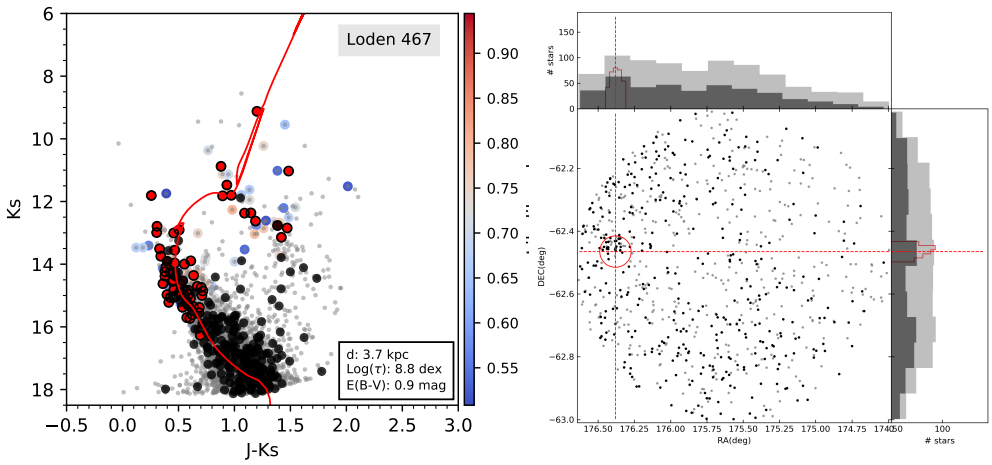

Figure 5.11: *Left panel*: Ks vs (J-Ks) CMD from VVV data for Loden 467. Symbols and colors are the same as in Fig. 5.5 . Black dots within r≤30″ and isochrone of $log(\tau)$=8.8 dex. *right panel*: Spatial distribution of the stars of the OC Loden 467 from Gaia DR2. FOV, symbols and colors are the same as in Fig. 5.7.

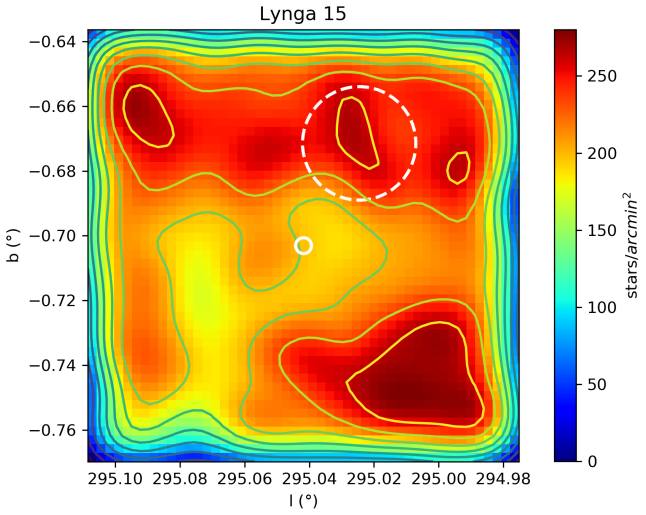

Figure 5.12: Same as in Fig. 5.2, but centered within a radius of 5′ around coordinates of OC Lynga 15. Dashed white circle marks the potential overdensity associated to Lynga 15.

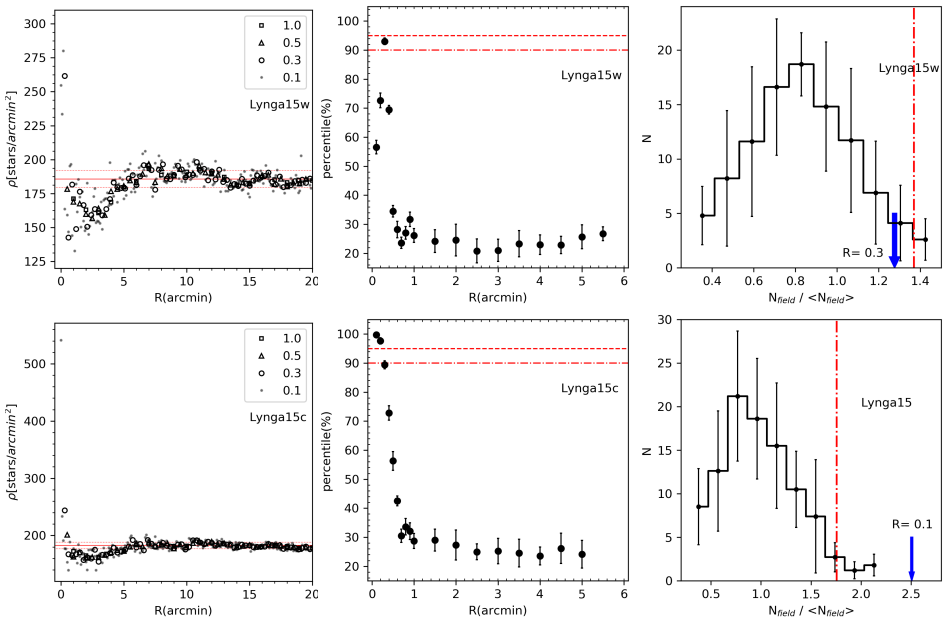

Figure 5.13: Same as in Fig. 5.3 for Lynga 15w and Lynga 15c.

seen in the Figures 5.1 and 5.12, the coordinates fall in a well with a density of stars of ~ 175 stars arcmin^{-2}, producing a miss-identification of the cluster center. However, three extended structures can be seen around it, near the limit of the field of view in Fig. 5.12. Those two that are located to the east (with $b\approx$-0.68° and $b\approx$-0.75°, respectively) are part of larger structures(see Fig. 5.1, for a wider view). The upper one is near to Bica 5, a probable open cluster remnant (Angelo et al., 2019). The third one, located west ($b\approx$-0.66°) is part of a field overdensity studied by Perren et al. (2020). These authors analysed that field in order to establish fundamental parameters for Lynga 15, but they finally concluded there is not a real cluster in that region. Nonetheless, Sampedro et al. (2017) and Dias, W. S. et al. (2014) located Lynga 15 at l=295.053°, b=-0.672°, a hardly noticeable lump above the center of the Fig. 5.12. The coordinates are reported in Webda database and we labeled this point with a 'w' subscript. Another lump is easily located slighty right-top. We marked this cluster candidate within a dashed white circle, and we labeled this point with a 'c' subscript, meaning a possible candidate to OC Lynga 15.

Fig. 5.13 shows final RDPs (left panels) for both lumps. RDP for Lynga 15w looks pretty odd. An overdensity can be noted at small radii, but rapidly falls in a well of about 160 star arcmin^{-2} at r=2′.5, then increases until reaching the field density at 6′. In Fig. 5.1 an under-density can be seen in this region, and Fig. 5.12 reveals that this happens at about 1′ from the selected center coordinates. RDP for Lynga 15c does not seem very different, but it presents a very high density at

r=0′.1. Because the extension of overdensities is just a fraction of arcminutes, they could be just fluctuations of the density field. Middle panels in Fig. 5.13 show the statistical comparison between the overdensities and the field as described in section 3.4.1. Cluster overdensities are statistically significant if, at least within a certain radius, the values of density they get are above the percentile 95^{th} with respect to the density distribution of the field. Only Lynga 15c meets this condition twice within the area of r=0.2′, then decreases rapidly to 28% in $r = 1'$. The right panel shows how $N_{over}/\langle N_{field}\rangle$ in its maximum average percentile, standing out over $N_{field}/\langle N_{field}\rangle$ distribution. In contrast, Lynga 15w lies within the distribution of the field.

We run the algorithm described in section 3.4.2 for a cluster area with radius 2′. The results are shown in Fig. 5.14. Because in the cluster few stars appear, we must be careful with the MLM selection. Increasingly lower probabilities were selected until obtaining a main sequence as defined as possible, as well as sets of tight stars at the parameter space. However, using very low values could select many intruders. We choose stars with likelihood values over 80%. Stars in parallax versus G-magnitude (left panel) and proper motion diagrams (middle panel) appear quite scattered. Despite the fact that the MLM follow an apparent main sequence over G≈17 (right panel), it is surprising that there are not more bright stars with high probability values. In the parallax vs G diagram it is shown that bright stars with 10 mag<G<14 mag) have parallaxes >0.4 mas, implying nearer distances, but more spread proper motions at the same time. The weighted average values for parallax and proper motions of the MLM are $\langle\Delta\varpi\rangle = 0.384 \pm 0.095$ mas, $\langle\Delta\mu_{\alpha^*}\rangle = -6.595 \pm 0.357$ mas·yr^{-1}, and $\langle\Delta\mu_{\delta}\rangle = 1.427 \pm 0.356$ mas·yr^{-1}, respectively, where the uncertainties are the simple standard deviations. No previous values were found in the literature for Lynga 15.

In order to get a deeper CMD and know which path an isochron should follow, we cross-matched the MLM found above with the VVV data. The maximum separation to match both catalogues was of 0.″3. This value was selected because the pixel scale on VVV was 0.″34 and the results were calibrated in the 2MASS astrometric and photometric system (Skrutskie et al., 2006), as detailed in Bidin et al. (2011) and Chené et al. (2012). Only three stars did not match. Two of them were below G=16 mag, and the third one was the variable star V 916 Cen with G≈8 mag. Despite the fact that Mauro et al. (2013) showed that the PSF fit can recover correct magnitudes up to about two magnitudes above saturation, the VVV frames saturate at Ks ≈ 12 mag, therefore that star falls outside the photometric range of VVV. Figure 5.15 (left panel) shows the Ks vs J-Ks diagram for Lynga 15. Gray dots are the stars within the cluster area, while dark dots are

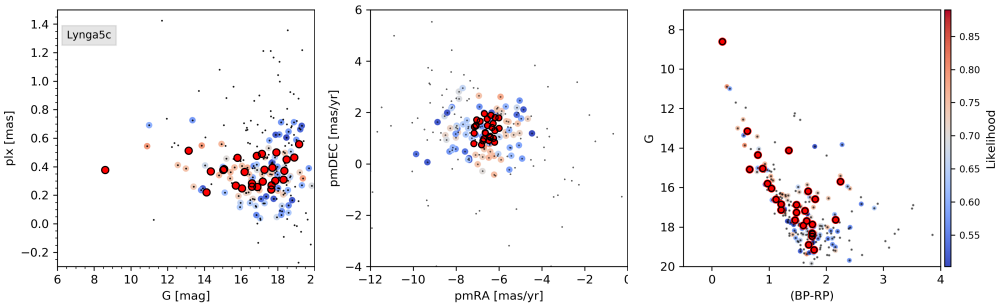

Figure 5.14: Same as in Fig. 5.4 for Lynga 15c.

stars within 30 arcsec. We added the V 916 Cen stars from 2MASS photometry to the diagram as a red square symbol. White squares represent our target star (see Table 3.2). One of our Targets is V 916 Cen. A PARSEC+COLIBRI isochrone of $log(\tau)$=7.0 dex was fit crossing the stars with likelihoods >80% (red circles). Isochrone was fit using the Bailer-Jones distance as first guess for the distance ($2.6^{5.0}_{2.0}$ kpc) and then fitting reddening and age. The isochrone was better fitted with a distance of d=2.8 kpc and E(V-B)=0.55. Because V 916 Cen is a high rotator variable star with v sini=224 ± 15 (Daflon et al., 2007), its position in the CDM is not guaranteed. Our results disagree with values reported by Dib et al. (2018) of d = 1380 pc and $\log(\tau) = 7.4$ dex.

Right panel in Fig 5.15 shows the distribution of stars in an area of 16′ around the center of Lynga 15c from Gaia DR2 data. Light gray color depicts the distribution of stars sharing the same average proper motion found for the cluster, while the dark one the stars sharing both the proper motion and the parallax. Red circle and lines represent the area and the center of the cluster, respectively. The star distribution is quite similar to the field indicating there is not a real cluster in that area. Indeed, in Fig. 5.15 it is shown that MLM (red circles) with Ks<13 do not seem to follow a clear main sequence. The outstanding overdensity in Fig. 5.13 is actually a field fluctuation in spite of the statistical significance. In the Lynga 15 region, blue stars contaminate the cluster area. This can explain the lack of more stars with high likelihoods between $8 < G < 14$ in G vs (BP-RP) diagram. Handful of stars in Ks≈14 mag Fig. 5.15 agree with the distribution of the Galaxy disk stars. We finally conclude the overdensity is not the cluster Lynga 15.

5.4 Bica 5

Bica 5 has been defined as an open cluster remnant (OCR) by Angelo et al. (2019), located 4′.3 northwest from Lynga 15, and just 3′.9 north from PN Hf 69 (see Fig.

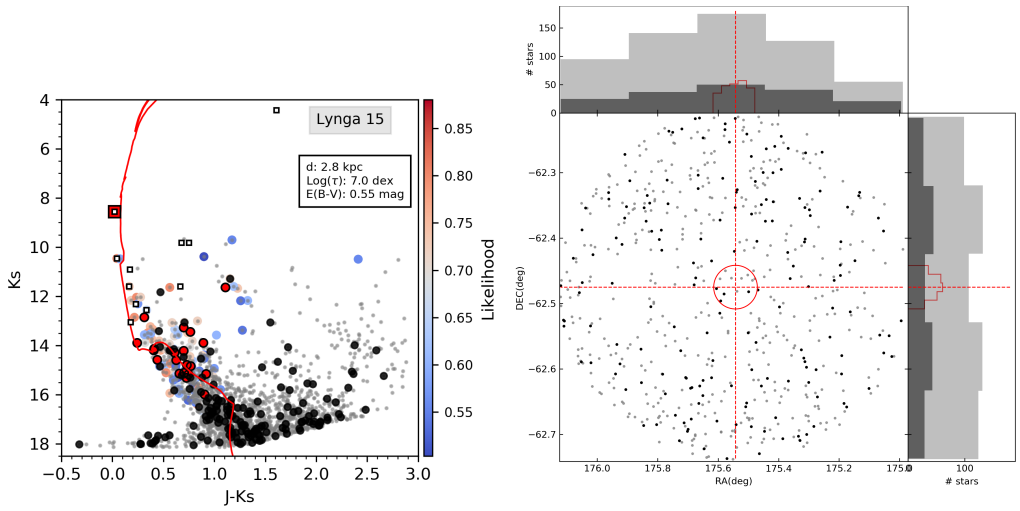

Figure 5.15: Same as in Fig. 5.11 for Lynga 15. *Left panel*: Black dots within r≤30″, and isochrone of $log(\tau) = 7.0$ dex. *Right panel*: FOV of 16′ centered in Lynga 15.

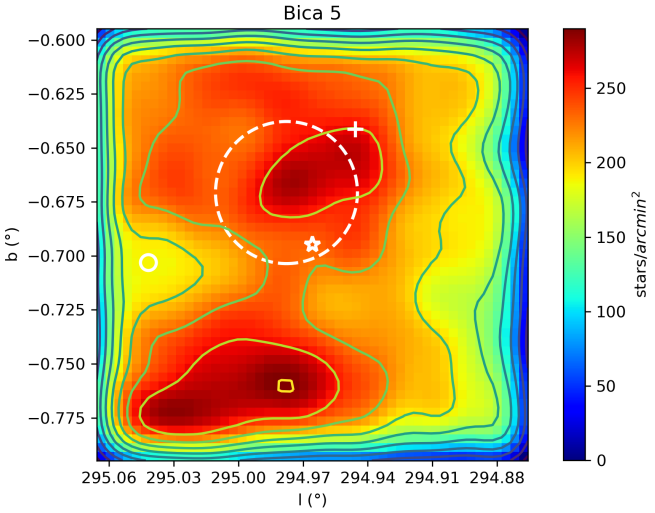

Figure 5.16: Panels and symbols are the same as in Fig. 5.2, but centered within a radius of 7′ around coordinates of PN Hf 69. Dashed white circle marks the potential overdensity associated to OC Bica 5.

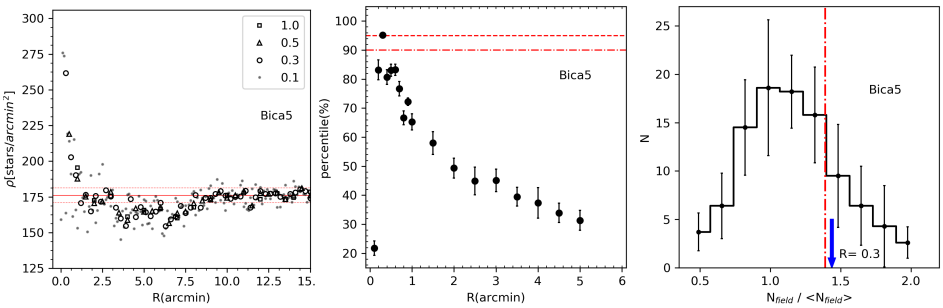

Figure 5.17: Same as in Fig. 5.3 for Bica 5.

5.1). Fig. 5.16 shows the density contour map of VVV data centered in the coordinates for PN Hf 69 (star symbol) within a radius of 6′. Plus symbol is located in the coordinates given by Angelo et al. (2019). Two lumps can be seen north of PN. One of them is slightly towards south of the plus symbol. Another lump is also south of PN, but it is part of a larger structure as can be seen in Fig. 5.1. Dashed circle depicts the area with the largest overdensity found in the that zone.

Figure 5.17 contains the density analysis in the zone of the Bica 5. RDP in left panel shows a center with about 275 $stars \cdot arcmin^{-2}$. A slightly under-density is identified between 3′ -′. The same happened with Lynga 15, and it is because Bica 5 is located in a low density area as can be seen in Fig. 5.1. Average field density was estimated beyond 8′. Middle and right panels in Fig. 5.17 show that the number of stars in the overdensity area is barely statistically significant with respect to the average number of stars in the field with the same radius, exceeding the 95% at a radius of 0′.3 (middle panel) and then, falling until 80% at 0′.4, slightly increasing at 0′.6, falling again until the 50% at 1′.5, and finally falling step by step to 33% at 5′. In the right panel it can be seen that the overdensity could easily be mistaken for field.

Data from Gaia DR2 were drawn within a radius of 2′ for the cluster area. The results of applying the procedure described in sec. 3.4.2 are shown in Fig. 5.18. A disperse group of stars with the largest likelihood over 80% (red circles) can be seen in parallax vs G-magnitude (left panel) and the proper motion (middle panel) diagrams. The procedure returns a weighted average parallax of $\varpi = 0.271 \pm 0.069$ mas, and proper motion of $\mu_{\alpha^*} = -6.495 \pm -0.367$ mas·yr^{-1} and $\mu_\delta = 1.554 \pm 0.476$ mas·yr^{-1}, where the error is the simple standard deviation. Parameters derived for Bica 5 from public data by Angelo et al. (2019) yield values of 0.481 ± 0.028 mas for parallax, and proper motions of -6.216 $\pm$ 0.037 mas·yr^{-1} and 1.070 ± 0.033 mas·yr^{-1}, respectively. Their mean parallax is almost twice as much as ours, while the proper motions agree within 1σ. Right panel in Fig.5.19 represents the CMD of G against (BP-RP), and it shows the MLM occupying a zone

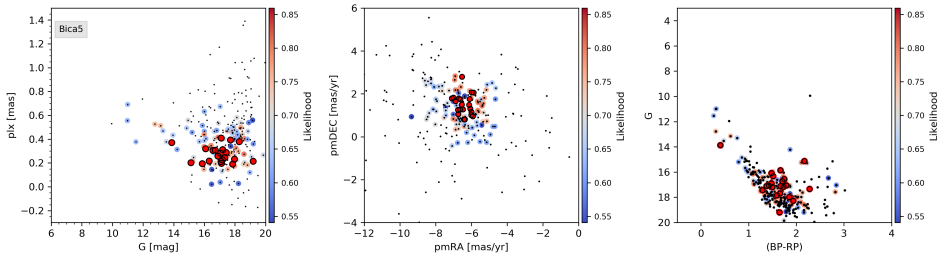

Figure 5.18: Same as in Fig. 5.4 for Bica 5.

under G≈15 mag that, added to the previous results, makes identifying a possible cluster difficult. However, it agrees with a possible old and disperse cluster. Fig. 5.19 shows the Ks vs (J-Ks) diagram. Gray dots are stars within the cluster area, while color circles are MLM found above, cross-matched with VVV data within 1″. Black dots represent stars in cluster within 20″, and it is possible to see a way of stars rise up to Ks≈15.5 mag, then curving until Ks≈14. This sequence of stars connects well with some MLM stars fitting an old isochrone of $log(\tau) = 9.5$ dex, with a distance of d=3 kpc and reddening of E(B-V)=0.9 mag. Isochrone distance roughly agrees with the distance parallax from Bailer-Jones of $3.5^{6.3}_{2.7}$ kpc. Parameters found by Angelo et al. (2019) for Bica 5 disagree with this work. The authors found a closer and younger cluster with d=1.91±0.26 kpc, and an age of τ=0.5±0.17 Gyr equivalent to log(τ)=8.7 dex. Angelo et al. (2019) located Bica 5 about 3′ away from our location. Around that location we could not find any significant density over the 95^{th} percentile, being the maximum $\sim$ 92%. Identification of the Bica 5 as an OCR is however uncertain. Spectral analysis of its potential members is always required and often rejected (de la Fuente Marcos et al., 2013). We prefer to be cautious to confirm its nature.

5.5 Membership of the PN Hf 69

PN Hf 69 lies relatively close to Bica 5 and Lynga 15 which have angular distances of 1′.6 and 3′.8 arcmins, respectively. Our results showed that Lynga 15 is not a real cluster (sec. 5.3). This result, agrees with the result found by Perren et al. (2020), who studied the same field in search of Lynga 15. Nevertheless, proximity with Bica 5 is quite suggestive. In the supplementary data, Frew et al. (2016) computed the reddening for Hf 69 using the Balmer decrement technique, and the distance through H_α SB-r relation, obtaining values of E(B-V) = 0.80 ± 0.14 mag and d = 1.73 ± 0.52 kpc. Reddening of the PN is in agreement with Bica 5 within 1σ. But, even if Bica 5 was a real cluster, and its parameters were equal to those found by us, the distances estimated indicate that the PN is a foreground object,

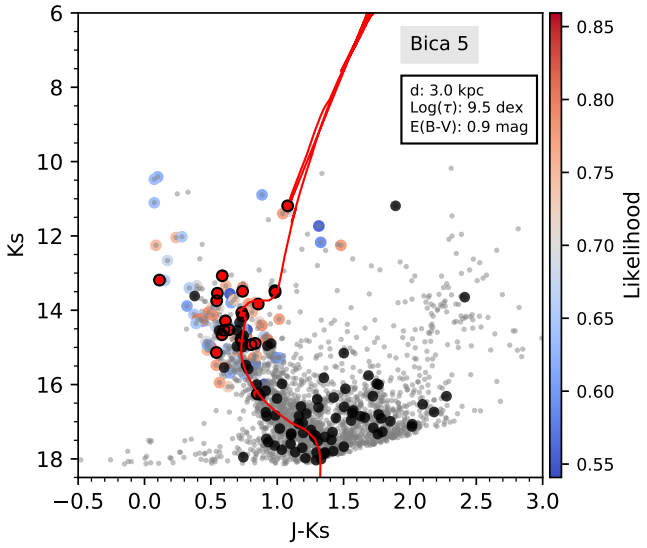

Figure 5.19: Ks vs (J-Ks) CMD from VVV for Bica 5. Symbols and colors are the same as Fig. 5.5.

and then the potential membership is discarded.

On the other hand, histograms in Fig. 5.7 show that OC Stock 14 could be quite extended. Hf 69 lies at ≈15′.7 from the cluster, quite far to be taken into account. Notwithstanding, Majaess et al. (2007) claim that the most potential PNe associated to OCs lie in cluster coronae, which is located beyond 2.5 times the nuclear radius. The cluster radius is 5′, so the Hf 69 would lie in the Stock 14 corona. Fig. 5.20 shows same star distribution as in Fig. 5.7 but we have added location of the PN (red star symbols). Red dots represent the same as the black ones, that is, stars sharing both the proper motion and the parallax of the cluster, but besides those lying in the brightest part of the CMD with G<11 mag. Fig. 5.4 (left and right panels) shows that the Lynga 15 stars dominate the brighter zone of the CMD. Most of the red dot stars are mainly distributed in the center of the cluster, but a few of them reach comparable angular distances to that of Hf 69, and even farther away (∼22′), showing that highly probable cluster members can inhabit areas far removed from the center of the cluster. This result could support the potential membership despite the large angular separation between the OC and the PN.

Additionally, RVs for the OC Stock 14 have been reported in literature with values ranging from $-8.6\,\mathrm{km\,s^{-1}}$ to $-16.4\,\mathrm{km\,s^{-1}}$ (Kharchenko et al., 2007; Loktin and Popova, 2017; Conrad et al., 2017). In sec. 3.3.3 we found RV=-15.23±2 $\mathrm{km\,s^{-1}}$ for Hf 69 (see Table 3.6), too close to be ignored. Furthermore, this value agrees with the RV of the variable star V810 Cen (HD 101947) of RV=-16.44 $\mathrm{km\,s^{-1}}$ (Mermilliod et al., 2008), a confirmed member of Stock 14. The study of RVs has often

been required to confirm real PN/OC associations (see, e.g., Mallik et al. 1995, Majaess et al. 2007). Disagreements in RVs between the PNe and the OCs are used to reject memberships (Kiss et al., 2008; Moni Bidin et al., 2014; González-Díaz et al., 2019). But when parameters such as distance, reddening and age agree, the membership must be analysed (Parker et al., 2011; Moni Bidin et al., 2014; Fragkou et al., 2019). Both the astrometric and the photometric distances found in this work for Stock 14 agree with the distance of 1.73 ± 0.52 kpc for the PN by Frew et al. (2016). However, reddening of the PN disagrees with the cluster in about 0.5 mag, indicating the PN could be located farther away. This fact is not at all conclusive, PN could suffer of internal reddening. Actually, following prescription by Majaess et al. (2007), potential associations can be established with differences in reddening between 0.2-0.6 mag. Furthermore, association between PN He 2-86 and OC NGC 4463 was established by Moni Bidin et al. (2014), despite a discrepancy in reddening of ≈0.9 mag. The authors claim the difference is probably due to high extinction inside the PN.

On the other hand, age is an important parameter to discard membership of PN in young OCs because evolved stars in clusters younger than ∼30 Myr (equivalent to $log(\tau) \sim 7.4$) are thought to end as type-II supernovae rather than forming a PN (Majaess et al., 2007; Moni Bidin et al., 2014). As described in sec. 5.1, we estimate a $\log(\tau)$=7.4 dex for Stock 14, just in the upper limit to forming PN (see Table 1.2). On the other hand, spectrum for Hf 69 in Fig. 3.6 shows emission lines in [NeIII] and HeII lines, that, in addition to spectrum reported in HASH database, show that the emission in [NII]λ 6.584 is remarkably higher than Hα, suggesting a possible type-I PN, i.e., a massive progenitor. However, in spite of all this agreeing factors, the cluster is so young that the mass associated to the progenitor would be very close to the limit to form supernova Type II. Such massive star so far from the cluster center is hard to explain, unless the progenitor is a binary system, as was discussed in sections 1.1 and 1.4.5. In the light of these results, the association is possible, but we do not have enough data to prove it. This case is surely interesting and deserves further study.

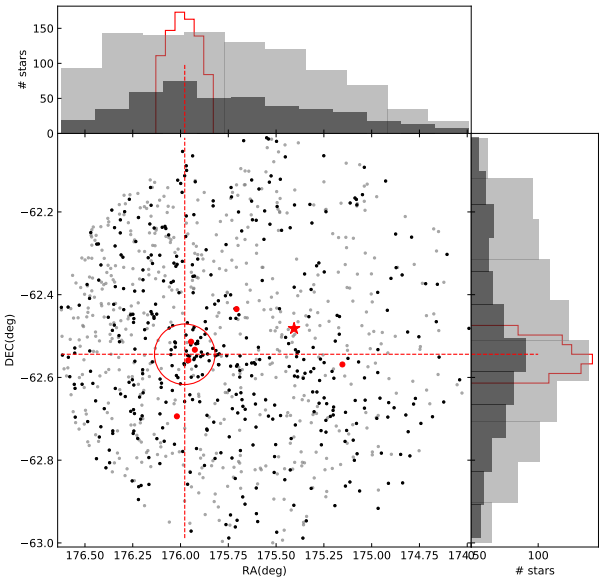

Figure 5.20: Same as in Fig. 5.7. Red star symbol represents location of the PN Hf 69, while the red dots depict the distribution of stars as the black ones, but with G>11.

Chapter 6

Lynga 5 and its distance dichotomy

Lynga 5 is an OC placed inside the Norma constellation in the Galaxy plane (Fig. 2.1). Majaess et al. (2007) studied the potential association between Lynga 5 and the near PN Hen 2-133 lying just 2.6′ from the cluster. The authors estimated a preliminary cluster distance of d = 1950 ± 350 pc, with a reddening of E(B-V) = 1.18 ± 0.11 and log(τ) = 7.7 using 2MASS photometry. Distance and age roughly agreed with a PN membership, but reddening disagreed by a factor of 2, implying a difference in the distance of about 2 kpc (Neckel and Klare, 1980). Thus, the PN would be placed in the background. Nevertheless, because several measures of the PN distance have shown contradictory results, the authors claimed for radial velocities in order to confirm or discard the association. New RVs for nine stars in the cluster and the PN were obtained, as well as JHKs photometric data from VVV, in order to assess the potential association. The methodology used in this chapter is the same as applied in Chap. 5 for the complex field around Lynga 15.

6.1 Results

Left panel at Fig. 6.1 shows the density contour map around Lynga 5 in a field of view of 15′ × 30′ from VVV data. X white symbol shows the center of the coordinates adopted by Kharchenko et al. (2013). PN is represented as a star symbol located northeast of the x-symbol. An extended, dense structure can also be seen east of the x-symbol inside of the white dashed circle. Because this zone is the densest area, we selected it to study the cluster. Center of the circle shows the point with highest density, and it was extended up to a radius of r=6′. Right panel at the Fig. 6.1 depicts the RDP of Lynga 5. Our FOV does not extend far

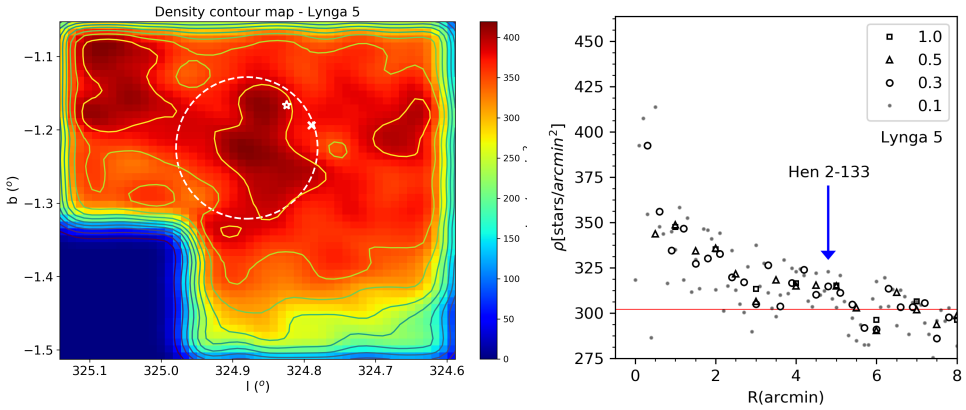

Figure 6.1: *Left panel*: Density contour map of Lynga 5 from VVV data. The field of view covers an area of $15' \times 30'$ centered at Lynga 5. Color bar represents the star density. White x-symbol shows the center reported for the cluster in visible light, while the star symbol marks the position of PN Hen 2-133. White dashed circle depicts the area of the cluster with a radius of r=$6'$ centered at the densest area. *Right panel*: Radial density profile for Lynga 5. Red line represents the star density of the field. Position of PN Hen 2-133 from the OC's center is shown.

enough to allow us to estimate an accurate average density of the field. The plot runs up to $8'$ because in that radius rings building the RDP reach the edge of the FOV (l≈325.0°, b≈-1.3°). However, we estimate the density field in about 300 star per arcmin^2 by eye. Position of the PN is marked with a blue arrow, lying at an angular distance of $4'.8$ from the new center, within the zone with high density. New center is located $5'.7$ from the position of x-symbol.

In order to find the MLMs of the cluster, astrometric and photometric data were extracted from *Gaia* DR2 within the area encompassing 30 arcmin from the point of the highest overdensity in the center of the Fig. 6.1 (left panel). The cluster area was chosen as the area marked with a dashed circle in the same figure, while the comparison field was selected having the same area as the cluster, but from a radius $r_{fld} > 3 \times r_{clu}$. We run the algorithm described in section 3.4 in order to identify the MLMs of the cluster. Results are shown in Fig. 6.2. Left and middle panels show that the algorithm resolved astrometric parameters of the cluster very well. MLM stars having a likelihood over 98% are very tight and they are marked as bright red circles. Plots also show the target stars (see Table 3.3) as white squares with error bars. The procedure returned values of the weighted average of the parallax of $\varpi = 0.336 \pm 0.023$ mas and proper motion of $\mu_{\alpha^*} = -3.625 \pm 0.130$ mas·yr^{-1} and μ_δ = -3.610±0.142 mas·yr^{-1}, where uncertainties are the statistical error on the mean. The values are in good agreement with Cantat-Gaudin et al. (2018a) who found values of 0.305 mas for the parallax and -3.660 mas·yr^{-1} and -3.561 mas·yr^{-1}

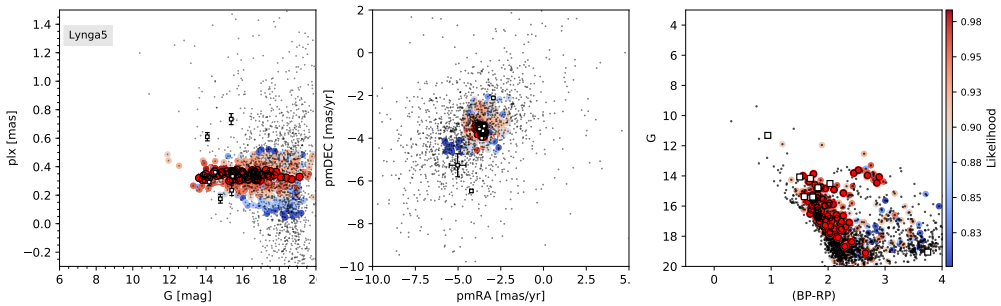

Figure 6.2: Parallax vs apparent magnitude G (left panel), Proper motions (middle panel), and G vs (BP-RP) (right panel) diagrams for stars of the OC Lynga 5. Color circles depict the membership probability of the stars at the clusters. White squares with error bars are the target stars.

for proper motion in right ascension and declination, respectively. Our results also agree within the error bars with Liu and Pang (2019) who reported values of (0.296±0.044 mas, -3.702±0.338 mas·yr^{-1}, -3.544±0.316 mas·yr^{-1}) for the same set of parameters. CMD of G vs (BP-RP) in the right panel of the Fig. 6.2) shows the MLM stars forming a wide main sequence with a turnoff near to G≈16 mag with a handful of red giant stars. Plots suggest Lynga 5 is a probable evolved cluster. White squares in G vs parallax and proper motions plots indicate that only three of the target stars seem probable members of the cluster.

In Table 3.3 the VVV photometry and Gaia astrometry of the target stars can be seen. The measured RVs and membership likelihood are also listed in the table. TYC 8704-1650-1 is the only target star for which RV is reported in Gaia DR2 with a value of -48.76±1.29 km s^{-1}. We obtained a value of -51±8 km s^{-1} for those stars, in good agreement with Gaia. Three target stars are definitely not members of the cluster, namely, TYC 8704-1650-1 which has very different proper motions of the data set, and Gaia DR2 5882736033000609536 and Gaia DR2 5882742144709393792 that have RVs with positive sign. Using only the RVs of the probable members stars whose likelihood values are greater than 50%, we found a weighted average radial velocity of RV=-56±18 km s^{-1}, where the weights are given by the likelihood values, and the error is the standard error on the mean. Results agree with Soubiran et al. (2018), who found RV=-68.12±0.59 km s^{-1} for Lynga 5 based only in radial velocities measured from Gaia DR2, using the most probable members of the cluster.

In order to establish the fundamental parameters of the cluster, data within a radius of 6′ were drawn from VVV, centered in the same point as before. CMD of Ks vs (J-Ks) is showed in Fig. 6.3. We crossmatched the probable stars found with Gaia DR2 with VVV data within 0.3 arcsec (color circles). Color bar represents the

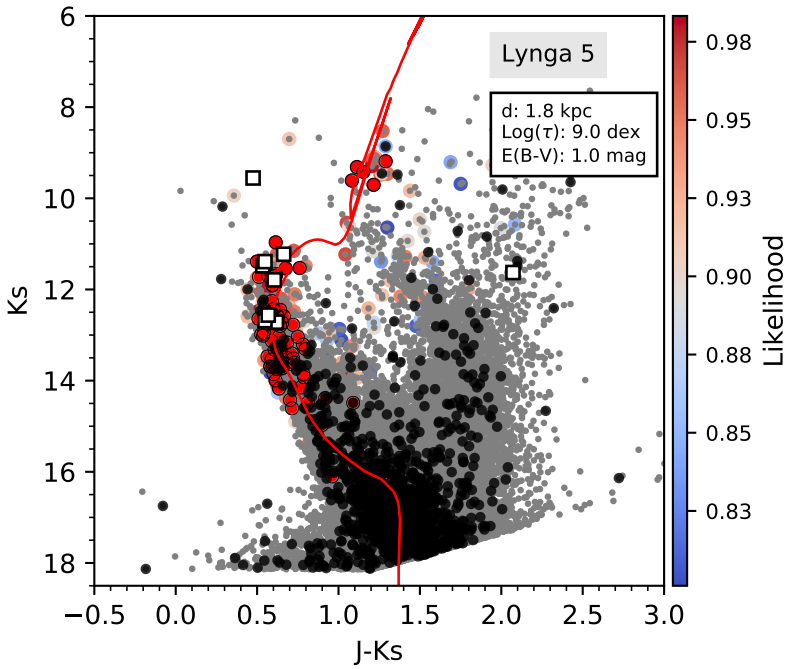

Figure 6.3: Ks vs (J-Ks) CMD for Lynga 5. Symbols are the same as in Fig. 5.15. White squares are the target stars with likelihoods > 90%. PARSEC + COLIBRI isochrone from Marigo et al. (2017) has been fitted to MLM stars.

probabilities of the stars belonging to the cluster as described above, while black points depict stars within 1′ around the highest overdensity. Target stars are shown as white squares. The figure shows how the MLM stars found with Gaia join with black dots at the top of the well defined main sequence with a handful of red giant stars in (J-Ks)≈1.3. A COLIBRI+PARSEC isochrone, with solar metallicity, was fitted using the Bailer-Jones distances computed through the average parallax as our first guess ($2.97^{3.38}_{2.69}$ kpc). An isochrone of d=1.8 kpc, with a reddening of E(B-V)=1.0 mag and a log(τ)=9.0 dex was finally obtained. The fit shows an old cluster with an equivalent age of 1.0 Gyr. This result is the oldest reported in literature for Lynga 5. In fact, Majaess et al. (2007) and Sampedro et al. (2017) reported logarithm of the age of 7.7 dex and 7.45 dex, respectively, possibly overlooking the reddest stars at the red clump, while Dib et al. (2018) found log(τ)=8.975 dex, and Liu and Pang (2019) reported an age of 0.708 Gyr equivalent to a log(τ)=8.85 dex, both in good agreement with us. On the other hand, the reddening we found for Lynga 5 agrees with the mean value of the literature. In fact, Majaess et al. (2007), Kharchenko et al. (2016) and Sampedro et al. (2017) reported color excess of 1.18 mag, 0.874 mag and 1.27 mag, respectively.

More interesting is the distance. Photometric distance noticeably disagrees in 1.2 kpc with the distance estimated from the average parallax using the Bailer-Jones

method. We found a photometric distance of d=1.8 kpc against d=$2.97^{3.38}_{2.69}$ kpc derived from the parallax. This discrepancy is not only ours, it is also found in literature. Our photometric distance is in perfect agreement with Kharchenko et al. (2016) and Sampedro et al. (2017) who reported 1753 pc and 1771 pc, respectively (although a different age). In contrast, our Bailer-Jones's modal distance agrees exactly with that reported by Cantat-Gaudin et al. (2018a) of 2993.4 pc computed through the parallax. Perren et al. (2020) found a discrepancy of 411 pc between the parallax and photometric distance, being the former larger, when no offset was applied to the parallax. The author also found a bias of +0.028 mas which must be added to parallax to correct the difference. This correction is in good agreement with the correction proposed by Bailer-Jones (2015) of +0.029 mas. We applied that correction to all parallax values from the beginning of this work. On the other hand, extinction in Ks fitting the isochrone took a value of A_{Ks}=0.35 mag. For that value, the Galactic interstellar extinction distribution model by Marshall et al. (2006) in Galactic direction l=324.75°, l=-01.25°(that is, very close to the cluster, see Fig. 6.1) returned a value in the distance of d≈3 kpc, in good agreement for the expected value of parallax distance. Moreover, Fig. 6.6 shows that the average RV found for Lynga 5 agrees with the RV expected for the rotation profile of the Galaxy at a distance of ≈3.0 kpc. For all these reasons, we adopt the parallax distance as the actual distance for the OC Lynga 5.

Discrepancy in the distances could be due to a misassignment on the metallicty in the isochrone fitting. In fact, Liu and Pang (2019) reported a metallicity of log(Z/Z⊙)=0.5 for the cluster. In order to assess the effect of metallicity in Lynga 5, a second isochrone was run updating this parameter and keeping the distances in the interval given by the parallax distance. Figure 6.4 shows the new CMD as well as the TCD. The JHKs two-colour diagram shows both the intrinsic theoretical and reddened isochrone with the reddening following the arrow direction. The slope was found in the same way as in sec. 4.1.1. Open square in the intrinsic isochrone corresponds to the points at the same temperature range as the spectroscopic estimates for target stars with likehood > 90% (see Table 6.1 for the results and sec. 3.3.2 for the methodology), that is, log(T_{eff})=[4.00,4.02]. Cluster stars are reddened by E(J-Ks)=0.62, which is equivalent to E(B-V)=1.18. A reddening relation of slope E(J-Ks) = 2.72 E(H-Ks) was obtained. The slope was derived by determining the differences of the average color indexes between the target stars with the same temperatures at the intrinsic and the reddened isochrones (empty and filled squares). Another reddening relation was also obtained with slope E(J-H) = 1.62 E(H-K). This result is in good agreement with the same relation from Dutra et al. (2002) and Bonatto et al. (2006), who found a slope of 1.72. With the Reddening, metallicity, and distance thus determined, a new PARSEC+COLIBRI

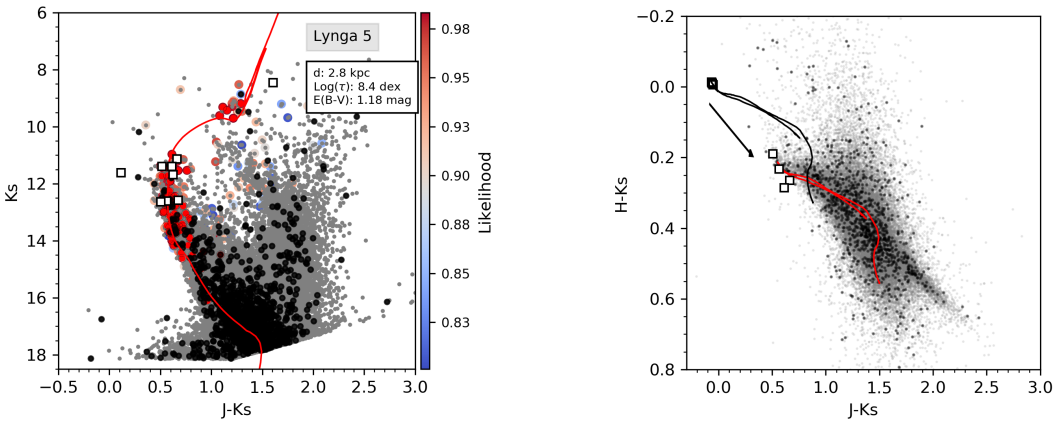

Figure 6.4: JHKs CMD (left panel) and TCD (rigth panel) of Lynga 5. Symbols are the same as Fig. 6.3. Black line in the TCD is the intrinsic isochrone, and the arrow shows the reddening direction. White squares in the same diagram represent the target stars with likelihoods > 90%. PARSEC + COLIBRI isochrone with Z=$10^{0.5}$Z$\odot$ from Marigo et al. (2017) has been fitted to MLM stars.

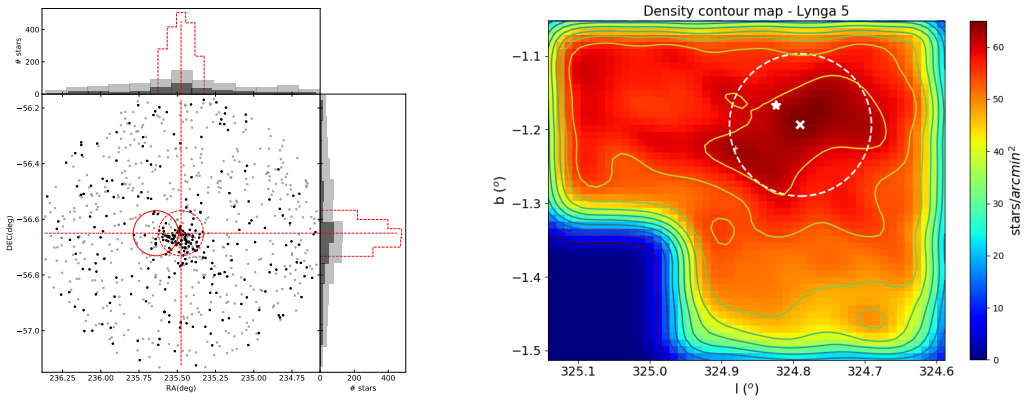

Figure 6.5: *Left panel*: Spatial distribution of the stars of the OC Lynga 5 from Gaia DR2. Symbols are the same as in Fig. 5.7 (see text). *Right panel*: Same as in Fig. 6.1 (left panel) but for stars with Ks<15 mag.

isochrone with Z=$10^{0.5}$Z$\odot$ was fitted with a final distance of d=2.8 kpc and an age of log(τ)=8.4 (left panel in Fig. 6.4)

Left panel in Fig. 6.5 shows the spatial distribution of stars sharing same proper motions (gray dots) and both the proper motion and the parallax (black dots) as Lynga 5. Data were extracted in a radius of 30 arcmin centered in Lynga 5 from Gaia DR2. The solid red circle represents the selected area for the cluster as shown in Fig. 6.1 (white dashed circle). MLM stars found using Gaia data are not distributed inside the zone of overdensity found with the VVV data (Fig. 6.1), but shifted east. Dashed red circle and lines represent the optic center of the distribution of stars in cluster from Gaia. This center is really near to optic center

Table 6.1: Derived parameters of the stars with the highest likelihoods of membership for Lynga 5.

Star	Ks (mag)	J-Ks (mag)	T_{eff} (K)	log(g) (dex)
Gaia DR2 5882742011595850496	11.39±0.03	0.51±0.05	10011±538	3.81±0.35
Gaia DR2 5882741942849715072	12.60±0.03	0.56±0.06	10631±572	4.14±0.32
Gaia DR2 5882742183394557312	11.14±0.05	0.66±0.08	10540±404	4.04±0.20
Gaia DR2 5882741942876369152	12.63±0.02	0.506±0.04	10141±554	3.79±0.17

reported in literature. This shift happens because of the depth of the VVV data, which reaches ∼19 mag in Ks (sec. 3.2.2). In fact, constraining the number of stars for all those with Ks<15 removes the shift of the center, favoring the optical solution (right panel in Fig. 6.5).

6.2 Membership of the PN Hen 2-133

Distance of the PN Hen 2-133 has been strongly contested. Estimates range between 1.30-1.70 kpc for the nearest distances (Maciel, 1984; Cahn et al., 1992; Tajitsu and Tamura, 1998), 2.88-3.18 kpc for middle distances (Zhang, 1995a; Phillips, 2004a) up to 3.866-5.0 kpc for farthest ones (Stanghellini and Haywood, 2010; Frew, 2008). The cluster's distance agrees with the distance by Zhang (1995a) and Phillips (2004a). However, Majaess et al. (2007) derived a reddening of E(B-V)=2.46±0.07 to PN through radio measurements (Cahn et al., 1992; Tylenda et al., 1992) . Such high color excess indicates the PN lies in the cluster background ($E(B-V)_{clu}$=1.18) reinforcing father distances by Stanghellini and Haywood (2010) and Frew (2008). In contrast, we found a RV for the PN of -23.36±2 km s^{-1} (sec. 3.1 and 3.3.3, and Table 3.6). Fig. 6.6 shows that the RV and the distance found in this work for OC Lynga 5 closely matches the distance-RV profile of the Galaxy. The profile was obtained assuming the rotation curve of Brand and Blitz (1993), the solar peculiar motion of Schönrich et al. (2010), R=8.0±0.3 kpc, and V_{LSR} = 220±20 km s^{-1}. In contrast, Radial velocity to the PN Hen 2-133 is consistent with nearer distance by Maciel (1984), Tajitsu and Tamura (1998), and Cahn et al. (1992). Reddening suggesting a background object and RV suggesting a foreground object are in evident contradiction. If the RV agrees with the near distances, that would imply and extremely high internal extinction for the PN. More data is needed to clarify this panorama. In any case, both possibilities rule out the association among the PN and the OC.

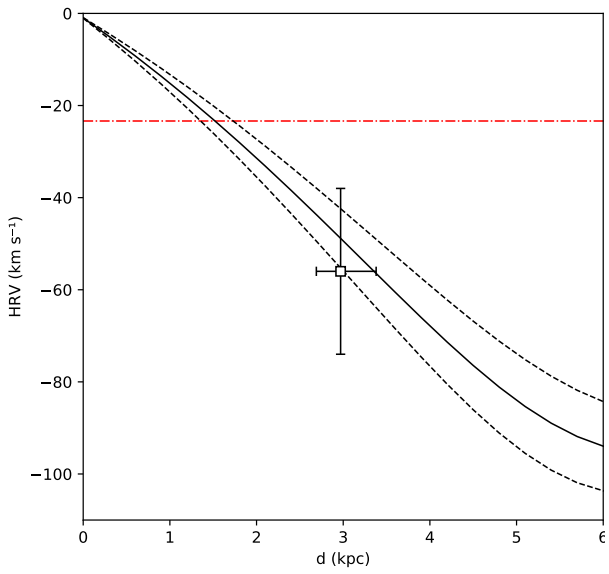

Figure 6.6: Distance-RV plot in the direction of Lynga 5. The solid curve shows simple theoretical model based on Galactic rotation, while the dashed curves indicate the 1σ propagation errors. Square with error bars shows the position of Lynga 5. Horizontal dot-dashed line represents the value of the RV for PN Hen 2-133.

Chapter 7

A beautiful quartet of stars

Surrounding the extended OC IC 2488 are two bright PNe (Wray 17-31 and NGC 2899), but their membership has often been discarded due to the large angular separation. On the other hand, the OC Basel 20 lies just a few arcmins ($\sim 8'$) from the PN Wray 17-31 and its potential association has never been studied. This chapter aims to assess the potential membership of the PNe Wray 17-31 and NGC 2899 in the IC 2488, and the potential membership of the PN Wray 17-31 in the OC Basel 20. We obtained twelve RVs for IC 2488, and eighteen more for Basel 20 as well as for both PNe. JHKs photometry from 2MASS was drawn at a FOV of $3° \times 3°$, covering an area that included all the objects. Additional astrometric data from *Gaia* DR2 was obtained including the same FOV as in 2MASS. Procedure is the same as in the chapters 5 and 6, but using 2MASS instead of VVV.

7.1 IC 2488

OC IC 2488 is an interesting object because several authors have discussed possible relationships with two PNe, namely, PN Wray 17-31 and PN NGC 2899 (Majaess et al., 2007; Frew, 2008, Pedreros, 1987). Nonetheless, the large angular separation between the cluster and the two PNe ($53'$ and $54'$, respectively), has played an important role in dismissing possible associations. IC 2488 is an extended cluster that can reach a nuclear radius of about $20'$ (Majaess et al., 2007). According to the latter authors, the PNe could be lying at the coronae cluster, which is located beyond 2.5 times the nuclear radius. Cluster distance has been established between 1250 ± 120 pc to 1445 ± 120 pc by Clariá et al. (2003) and Pedreros (1987), respectively, with a reddening of E(B-V)=0.24 ± 0.04. These values are consistent with the parameters found for both PNe. Moreover, Pena et al. (1997) derived a distance of d=1200 ± 200 pc and a reddening of E(B-V)=0.38 for the PN Wray 17-31,

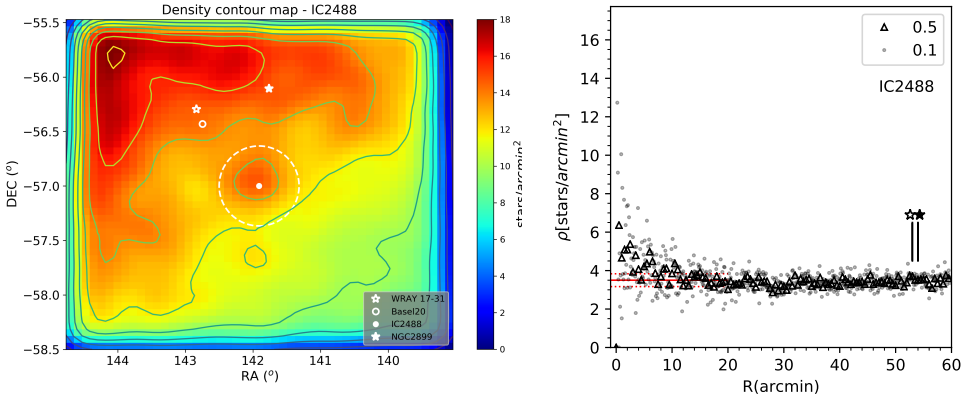

Figure 7.1: *Left*: Density contour map of IC 2488 from 2MASS data. The field of view covers an area of 3°×3° centered at the coordinates for IC 2488. Color bar represents the star density. White circles indicate the location of the clusters IC 2488 and Basel 20. Filled and unfilled star symbols mark the position of the PNe WRAY 17-31 and NGC 2899, respectively. White dashed circle depicts the chosen area for the study of IC 2488 with a radius of 20′. *Right*: Radial density profile for IC 2488. Solid red line represents the star density of the field with its $1\,\sigma$ dispersion (dotted line).

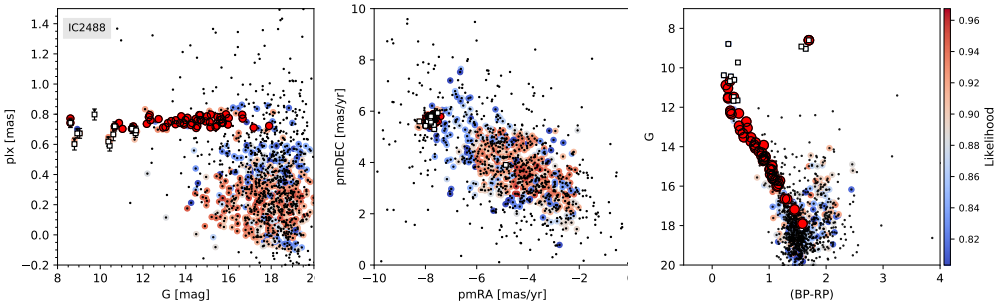

Figure 7.2: Parallax vs apparent magnitude G (left panel), proper motions (middle panel), and G vs (BP-RP) (right panel) diagrams for stars of the OC IC 2488. Color circles depict the membership probability of the stars at the clusters. White squares with error bars are the target stars.

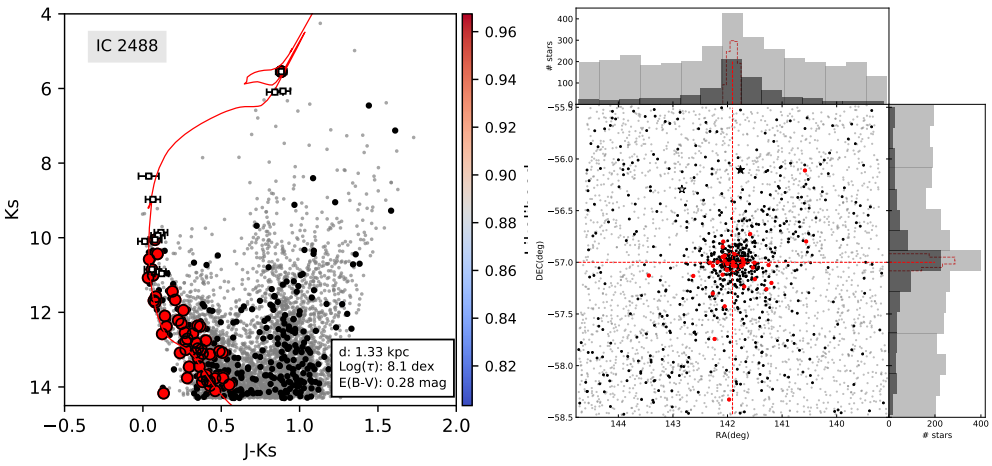

Figure 7.3: *Left*: Ks vs (J-Ks) CMD for OC IC 2488. Symbols are the same as Fig. 5.15. White squares with error bars are the target stars. *Right*: Spatial distribution of the stars of the OC IC 2488 from Gaia DR2. Symbols are the same as Fig. 5.7. The location of the PNe was marked with star symbols.

while values extracted from literature for PN NGC 2899 yield an average distance of d=1480 ± 500 pc and a reddening of E(B-V)=0.32 ± 0.24 (Tylenda et al., 1992; Zhang, 1995a; Frew, 2008). A more precise determination of the parameters, including radial velocities, is mandatory to assess the physical association between the OC and the PNe.

Figure 7.1 shows both the density contour map and the RDP for IC 2488. Data were drawn from 2MASS database for a field of view of 3°×3° around the center of the cluster. Left panel shows relative position of IC 2488 with respect to Wray 17-31 (empty star symbol) and NGC 2899 (filled star symbol). Location of the small cluster Basel 20 is also shown (see sec. 7.2). Data were restricted to stars with J≤15.8 mag, H≤15.1 mag, and Ks≤14.3 mag. These limits correspond to the 99% completeness limit of the 2MASS catalogue. Fig. 7.1 shows a small overdensity in ∼12 stars·arcmin^{-2} at the center, and then falling to reach the field density in ≈20′. Dashed circle in left panel shows the area corresponding to that radius. Right panel also shows that the density of stars increases towards the northwest direction, that is, towards the Galactic disk.

In order to establish the fundamental parameters of the cluster, we extracted both the photometric and the astrometric parameters from Gaia DR2 around the same FOV as in 2MASS. However, due to the fact that the star field contamination increases as we move away from the center, we selected stars within a radius of $r_{clu} < 5'$ in the innermost and densest area of the cluster, to be analyzed. The comparison field was chosen having the same area but in a region $r_{fld} > 10 \times r_{clu}$. Results of applying the procedure described in section 3.4.2 are shown in Fig. 7.2.

The color bar depicts the probability of a set of stars to form a cluster. Plots show two sets of stars with high likelihood of being in clustering. Sets can be clearly seen in the Parallax vs G diagram (left panel) and proper motions (middle panel) diagrams, where red circles represent stars with high likelihoods >75%. Bright red circles depict stars with highest likelihoods (>94%) clustering closely in the parameter space with large values in parallax, and markedly separated from most stars. In contrast, light red circles show a major second set of stars occupying a broader area with smaller parallaxes. CDM in right panel shows how stars with the highest likelihood form a well defined main sequence, while the least likely stars are distributed in the region corresponding to Galactic disk stars. The procedure returned weighted average values for the parallax of $\varpi = 0.751 \pm 0.028$ mas and proper motion of $\mu_{\alpha^*} = -7.767 \pm 0.122\,\mathrm{mas \cdot yr^{-1}}$ and $\mu_\delta = 5.680 \pm 0.122\,\mathrm{mas \cdot yr^{-1}}$ where uncertainties are the simple standard deviations. Our results are in perfect agreement with Cantat-Gaudin et al. (2018a) who reported values of 0.718 mas for the parallax, and -7.761 $\mathrm{mas \cdot yr^{-1}}$ and 5.698 $\mathrm{mas \cdot yr^{-1}}$ for proper motions in right ascension and declination, respectively. Fig. 7.2 also shows our target stars as squares with error bars. Corresponding values of parallaxes, proper motions and likelihoods can be seen in Table 3.4. Most of the target stars seem sharing the same parameters as the cluster, except HD 302213 which, despite sharing almost the same parallax with the cluster, has a very different proper motion. We computed the RV of the cluster using probable member stars whose likelihood values are greater than 50% in Table 3.4. A weighted average radial velocity of RV = -3±2 $\mathrm{km\,s^{-1}}$ was obtained, where the weights are the likelihood values, and the error is the the statistical error on the mean. Our results agree with values obtained by Clariá et al. (2003) of $-2.63 \pm 0.06\,\mathrm{km\,s^{-1}}$, and with the more recent work by Soubiran et al. (2018), who obtained a value of $-1.42 \pm 2.14\,\mathrm{km\,s^{-1}}$ using four selected members of the cluster from Gaia DR2.

Left panel in Fig. 7.3 shows the CMD Ks against (J-Ks) from 2MASS data. Gray dots are stars with $r < 20'$ while black dots are stars with $r < 5'$ centered in the cluster. We crossmatched stars with high likelihoods from Gaia DR2 with 2MASS catalogue within $0''.3$. Target stars are also shown as white squares with error bars. Stars with likelihoods >94% are represented as bright red circles. As expected, they are distributed following a main sequence. A COLIBRI+PARSEC isochrone was fitted by crossing over them, and using the parallax to compute the Balier-Jones distance as our first guess ($1.33^{1.42}_{1.26}$ kpc). We finally obtained a photometric distance of d=1.33 kpc, with a reddening of E(B-V)=0.28 mag and a $\log(\tau)$=8.1 dex. Photometric distances agree with parallax distances exactly. Our distance result also agrees exactly with the distance computed by Soubiran et al. (2018), and it is in good agreement with the previous values of distance, reddening and age obtained

Table 7.1: Literature results for the fundamental parameters of the OC IC 2488.

Literature	d (pc)	E(B-V) (mag)	log(τ) (dex)
Pedreros (1987)	1445±120	0.26±0.02	8.0
Clariá et al. (2003)	1250±120	0.24±0.04	8.25
Kharchenko et al. (2016)	1138	0.208	8.445
Sampedro et al. (2017)	1134	0.23	8.11
Loktin and Popova (2017)	1483	0.324	7.395
This Work	1330^{1420}_{1260}	0.28	8.1

in literature (see Table 7.1).

7.1.1 Membership of the PNe Wray 17-31 and NGC 2899 in OC IC 2488

Two 2D-spectra in middle resolution were obtained for NGC 2899 and one more spectra for Wray 17-31. The final estimate was obtained from the average of these measurements (Details in the procedure can be revised in sec. 3.1 and 3.3.3). RV for PN NGC 2899 was found to be RV =-6±3 km s^{-1}, and RV=35±1 km s^{-1} for Wray 17-31 (Table 3.6).

Wray 17-31: Our results show a distance of d=$1.33^{1.42}_{1.26}$ kpc and E(B-V)=0.28 for IC 2488. Distance agrees with the estimate by Pena et al. (1997) for the PN of 1200±200 pc. In a more recent work, Frew et al. (2016) computed the distances for the PN obtaining d= 1.74 ± 0.49 pc and E(B-V)= 0.24 ± 0.04 via the H_α surface-distance relation and central star of the PN photometry, respectively. Both results roughly agree with the cluster in $\sim 1\sigma$. Measurements of distance have also been tried for Wray 17-31 using Gaia DR2. As shown by Kimeswenger and Barría (2018) Gaia DR2 it is useful to determine distances of the PNe through the parallax only if the photometric colors of central stars are in the range of -0.65 $\leq$ (BP-RP) $\leq$ -0.25. Outside this interval, Gaia DR2 cannot identify the central star correctly due to contamination of the H_α+[NII] emission line of the PN envelope. Chornay and Walton (2020a) reported a color index of (BP-RP) = -0.35, which is within the interval of the right identification of the central star of Wray 17-31. The Bailer-Jones distance computed through the parallax is 1506^{1846}_{1270} pc, also agreeing with the cluster within 1σ.

On the other hand, a RV of 61 ± 8 km s^{-1} for the PN was reported by Frew (2008)

from the Hα line. Our RV measurement for the PN is in disagreement with that value in almost a factor of 2. Despite the great agreement between reddening and distance, our three measurements of the RV (sec. 3.1) were very consistent between them, and therefore we rule out the association between PN Wray 17-31 and the OC IC 2488.

NGC 2899: Several distance measurements for PN NGC 2899 have been attempted. Pedreros (1987), reported a distance of 1450 pc, while later estimates implied distances of d$\approx 1560 \pm 570$ pc with E(B-V)$\approx 0.32 \pm 0.24$ (Tylenda et al., 1992; Zhang, 1995a). Subsequent works have yielded distances of 1.06 kpc (Phillips, 2004a), 1.026 ± 0.205 pc (Stanghellini and Haywood, 2010), and 1.44 ± 0.41 kpc (Frew et al., 2016). More recently, González-Santamaría et al. (2019) computed the Bailer-Jones distance using the parallax from Gaia DR2. The authors found a distance of d=2049^{2215}_{1906} pc, farther than previous estimates. However, this result is unreliable because Gaia DR2 missidentifies the central star of NGC 2899. Indeed, the color index for the PN is (BP-RP) = 0.973, which is highly reddened for a PN central star. Our distances for the cluster (d= $1.33^{1.26}_{1.42}$ kpc) agree perfectly with the mean value from literature for NGC 2899 of d= 1.3 ± 0.2 kpc. Nonetheless, the measures for reddening show higher values than those of the cluster. Using nebular extinction from Balmer decrement and CSPN photometry, Frew et al. (2016) obtained E(B-V)= 0.48 ± 0.06, greater than the one found by Zhang (1995a) and Tylenda et al. (1992) of 0.32 ± 0.24. Notwithstanding, such difference in the reddening between the Cluster and the PN (ΔE(B-V)≤ 0.2) is not enough of a criterion to dismiss the association as claimed by Majaess et al. (2007) (see Tab. 1.2) and discussed by Moni Bidin et al. (2014).

In contrast, RV is a heavier criterion to confirm or reject associations. Durand et al. (1998) obtained a RV=$3.4 \pm 2.8, \mathrm{km\,s^{-1}}$ for the PN, differing by slightly more than 2σ from the cluster value (-3$\pm$2 km/s). On the contrary, we found a RV for the PN of RV = -6 $\pm$3 $\mathrm{km\,s^{-1}}$. Our result is closer to the cluster than the previous one, within 1σ. This similarity among the distance and our RV measurements indicate a potential association.

NGC 2899 is a bipolar PN showing multiple shells with internal complex structure (see Fig. 2.3). Spectrum in Fig. 3.6 shows emission in [NeIII] and HeII lines, that, in addition to spectrum reported in HASH database, show that the emission in [NII]λ6.584 is remarkably higher than Hα, suggesting a possible type-I PN, i.e., a massive progenitor. Cluster age of log(τ)=8.1 is equivalent to a turnoff mass of $\approx$4M$\odot$, which also agrees with the membership.

Nevertheless, as we had anticipated, one of the strongest arguments to dismiss po-

tential association between the PN NGC 2899 and OC IC 2488 is the large angular separation ($\sim$54$'$). Right panel in Fig. 7.3 shows the star distribution of the full sample extracted from Gaia DR2, sharing the same proper motion (gray dots), and proper motion along with parallax (dark dots) as does IC 2488, within the 3σ in their uncertainties. Figure shows that stars sharing only the same proper motions as the cluster's suffer from contamination at large angular distances. In contrast, stars sharing proper motion along with parallax follow the behavior expected only for stars in cluster. Indeed, the highest star field contamination lies in a zone with G$>$12 and $\varpi < 0.60$ mas, as can be seen in Fig. 7.2 (left panel). Additionally to proper motions, choosing stars within a region with $0.66\,\mathrm{mas} < \varpi < 0.83\,\mathrm{mas}$ avoids both the far and foreground star fields. Red dots in Fig. 7.3 are stars as the dark ones, but including those lying in the brightest part of the CMD with G$<$12 mag. These stars are mainly distributed in the center of the cluster, but a few of them reach angular distances similar to that of PN NGC 2899 (filled star), and even farther away (51$'$, 60$'$ and 69$'$), showing that they can inhabit areas far removed from the center of the cluster. This result also supports potential membership despite the large angular separation between the OC and PN. In adittion, Turner and Pedreros (1985) and Usenko et al. (2019) showed that an important fraction of short-period Cepheids, fall within the host coronae clusters. That kind of Cepheids are potential progenitors of planetary nebulae.

7.2 Basel 20

In the previous section it was shown that PN WRAY 17-31 is not associated to IC 2488. Nevertheless, this PN lies only 8.$'$6 away from OC Basel 20. This inconspicuous cluster, located in the Vela constellation ($\alpha = 9^h30^m59.5^s$ and $\delta = -56°25'48''$) was first identified as a physical group by Topaktas and Fenkart (1982). Despite their proximity, Majaess et al. (2007) did not take into account this pair as possibly associated. Fig. 7.4 shows the color magnitude diagram G against (BP-RP) centered in the cluster. Black circles are the cluster stars, while gray circles are field stars. Cluster stars show a well defined main sequence formed by bright stars emerging at G$\approx$18 mag from the usual stellar structure produced by Galactic disk stars, and reaching G$\approx$8 mag. White squares represent the stars at which the radial velocities were measured. CMD also shows a group of less reddened stars most of them being target stars at G$<$14. Only a few of them seem to follow the main sequence and are marked by black circles.

Fundamental parameters of the cluster have been previously measured by various authors. The most recent works locate the cluster at distances ranging fron 1380 pc

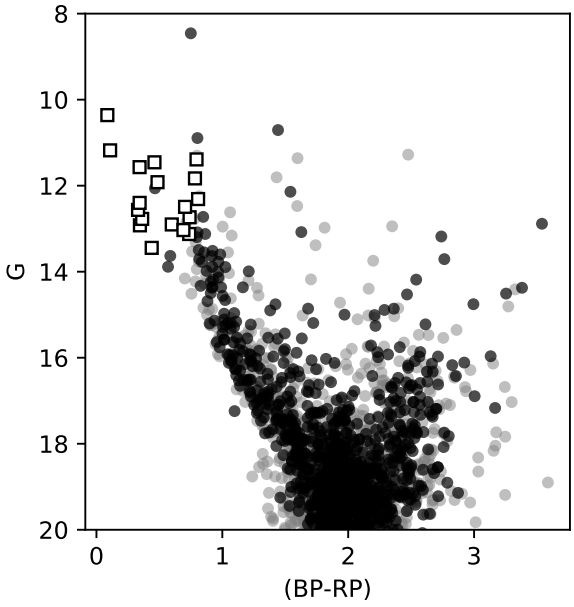

Figure 7.4: Color-magnitude diagram for Gaia DR2. Black circles are the stars within 5′ from the center of Basel 20, while gray circles depict field stars. Squares are the target stars.

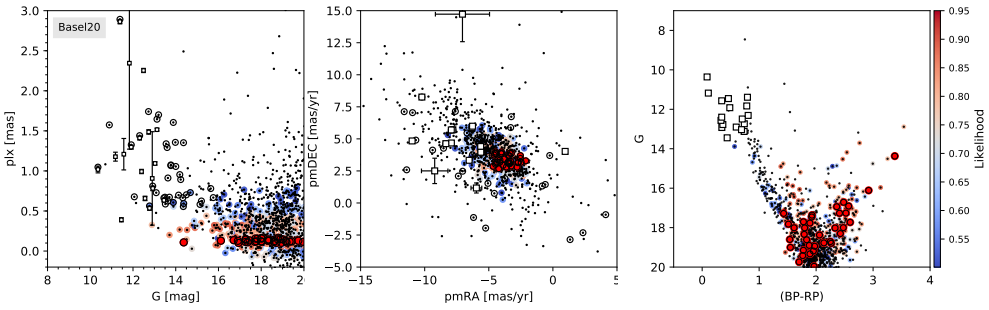

Figure 7.5: Same as in Fig. 7.2 for Basel 20. White squares with error bars are the Target stars.

to 2024 pc (Kharchenko et al., 2016; Loktin and Popova, 2017; Sampedro et al., 2017; Dib et al., 2018). Both age and reddening of the cluster have had less variations with values of log(τ)=7.45 dex and E(B-V)=0.41, except for Kharchenko et al. (2016) who found a more reddened cluster with E(B-V)=0.625. Distances for the PN have also been obtained. Pena et al. (1997) estimated a distance of 1200 ± 200 pc, while Frew et al. (2016) obtained a mean distance of 1.74 ± 0.49 kpc using the $S_{H\alpha}$-r distance relationship. More recently, González-Santamaría et al. (2019) computed a parallax distance for the PN using Gaia data. Parallax measures for PNe are reliable only if the central star at the PN is clearly identified. The color index for the central star of the PN WRAY 17-31 is (BP - RP)=-0.35, easily identifiable to Gaia. The authors obtained a distance of 1506^{1847}_{1270} pc, in good agreement with previous values.

Astrometric and photometric parameters were extracted from *Gaia* DR2 within an area of 25′ from the center of Basel 20. Cluster area was chosen with a radius of 5′, while the comparison field was selected having the same area as the cluster, but from a radius $r_{\rm fld} > 3 \times r_{\rm clu}$. We run the algorithm described in section 3.4.2 in order to identify the MLMs of the cluster. Results are shown in Fig. 7.5. Stars having a likelihood over 90% were marked as bright red circles. Plots also show the target stars as white squares with error bars. Parallax against G magnitude diagram (left panel) shows stars with the highest likelihoods taking up a narrow band in G>14. Target stars are scattered in a wide range of parallaxes values. Same result is found in the proper motions diagram (middle panel). Probable member stars are located in an area with high dispersion in parameter space, while target stars do not appear to be associated at all. At CMD (right panel) stars with higher likelihoods in the structure are surprisingly often associated with the Galactic disk stars despite the outstanding main sequence. Empty circles in left and middle panels show stars with color indexes (BP-RP)<1, that is, brighter stars in the apparent main sequence of Basel 20. The panel shows that stars forming the apparent main sequence are not really associated between them, and consequently we conclude that Basel 20 is not a real cluster. Another possibility is to think of Basel20 as an older or farther cluster. In that case, the procedure returns values of the weighted average for the parallax of $\varpi = 0.128 \pm 0.018$ mas and for proper motion of $\mu_{\alpha^*} = -3.692 \pm 0.687$ mas·yr^{-1} and $\mu_\delta = 3.370 \pm 0.379$ mas·yr^{-1} where uncertainties are the simple standard deviations. Fig. 7.6 presents the star distribution sharing same proper motions (gray dots) and both the proper motions and the parallaxes (black dots) found above. The plot shows clearly that the star distribution is the same as the field, confirming that there is not a cluster in the area.

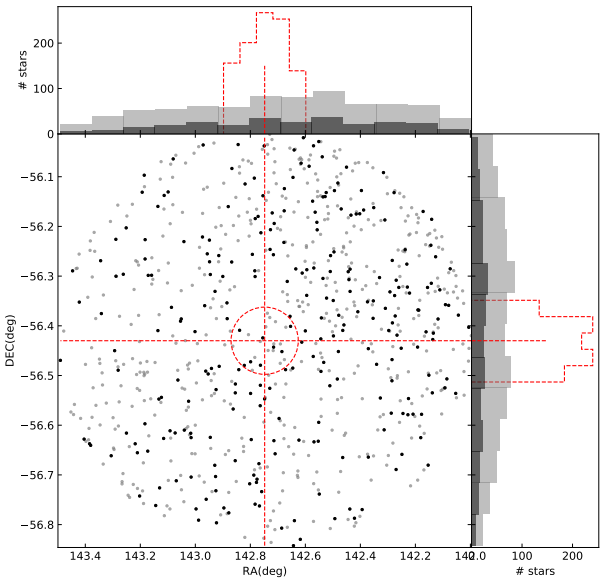

Figure 7.6: Star distribution with the same proper-motion (light dots), and proper motion along with parallax (dark dots) constrained to the same average values found for Basel 20 from Gaia DR2. Field of view covers 25′ centered in the Basel 20 coordinates. Both the red circle and the red line show the area and the center chosen for the cluster, respectively.

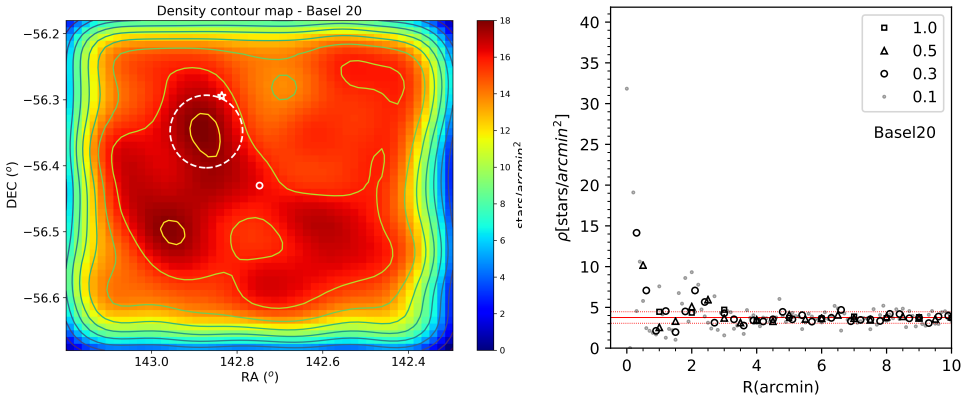

Figure 7.7: *Left*: Density contour map of Basel 20 from 2MASS data. The field of view covers an area of $15' \times 15'$ centered at the coordinates for Basel 20. Color bar represents the star density. The small white circle indicates the previous location of the cluster. White star symbol marks the position of PN WRAY 17-31. White dashed circle depicts the chosen area for the cluster with a radius of r=3′ centered at the densest area. *Right*: Radial density profile for Basel 20. Solid red line represents the star density of the field with its $1\,\sigma$ dispersion (dotted line).

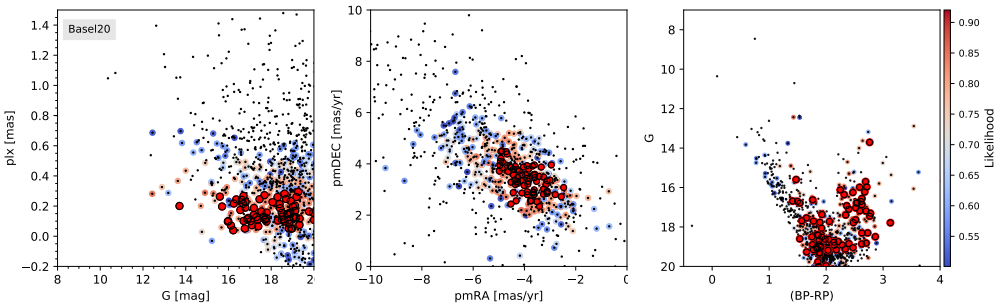

Figure 7.8: Same as in Fig. 7.5 for the new proposed center of Basel 20.

Because of light visible center of the coordinates for a cluster often disagrees with the infrared center (a notorious case was studied in Chapter 6), we extracted photometric data from 2MASS in order to assess the existence of Basel 20 one more time. Data were restricted to stars with $J \leq 15.8$ mag, $H \leq 15.1$ mag, and $Ks \leq 14.3$ mag. These limits correspond to the 99% completeness limit of the 2MASS catalogue. Left panel at Fig. 7.7 shows the density contour map around in a filed of view of $15' \times 15'$ centered in the previous Basel 20 coordinates (small white circle). PN WRAY 17-31 is represented with a white star symbol, while the dashed circle shows the chosen area to study the potential cluster. In this case, the densest area is nearer to PN than the previous location for the cluster. Right panel shows the RDP at the center of the dashed circle. The profile shows an overdensity reaching 32 stars·arcmin^{-2} in the innermost area. We settled for a radius of $\sim 3'$, which seems to contain the most of overdensity.

Figure 7.8 presents the results of applying the algorithm again on the new center, in order to find the MLM of the cluster. The average weighted values are: $\varpi = 0.150 \pm 0.065$ mas; $\mu_{\alpha^*} = -3.894 \pm 0.615$ mas·yr^{-1}; and $\mu_\delta = 3.378 \pm 0.528$ mas·yr^{-1}, where uncertainties are the simple standard deviations. This results are virtually the same as the previous ones, but with highest uncertainties. Only stars at the structure of the Galaxy disk got higher likelihoods. This result confirms that Basel 20 is not a real cluster but a group of bright stars at different distances. We conclude there is no OC in the vicinity of PN WRAY 17-31, to which it can be associated.

Chapter 8

Conclusions and future work

8.1 Conclusions

We began this work aiming to assessing the possible association between five pairs of PNe/OCs. Nevertheless, the field around OCs turned out to be quite complex, so our first efforts were addressed to establish the fundamental parameters of the clusters. Table 8.1 and Table 8.2 summarize the most relevant results for the open clusters and PNe studied in this work, respectively. The left to right columns in 8.1 are: Cluster ID, parallax, proper motion in right ascension, proper motion in declination, cluster Radial velocity, the Balier-Jones distance, isochrone distance, reddening, and logarithm of the age. Gaia DR2 has shown to be very useful in determining astrometric parameters selecting stars in clusters over the field via proper motions and parallaxes with great precision. In addition, JHKs photometry from VVV has shown noticeable improvement in the reduction of uncertainties of the distances for open clusters (Majaess et al., 2012a). Besides, differential reddening in VVV photometry are less harmful than in the optical. Joining together the most likely cluster members obtained from Gaia DR2 and the deeper main sequences from VVV, we aimed to obtain precise determination of the photometric parameters for the known clusters and investigate the nature of those that have still been little studied.

We presented the results of distance analyses solving the long-standing discrepancy regarding the fundamental parameters of the OC NGC 2453 and the debated cluster membership of the PN NGC 2452 (Chapter. 4), which were previously likely affected by the selection of cluster stars contaminated by field objects. The difference in RV between the PN (62±1 km s^{-1}) and the cluster (78±3 km s^{-1}) found in this work is noticeable and highly significant ($\sim 5\sigma$), excluding a physical association between this pair. All photometric diagrams (Fig. 4.3) show the presence

of a robust group of foreground stars located at distances $\leq$3.5 kpc and contaminating the cluster field. According to the theoretical distance-velocity profile of the Galactic disk in the direction of Puppis (Fig. 4.5), the RV we obtained for the PN NGC 2452 is consistent with membership to this foreground population.

The pair Hf 69/Lynga 15 was quite interesting because five more clusters reported in literature lie in the vicinity, namely: Loden 467, Stock 14, Loden 464, Loden 465 and Bica 5 (Fig. 5.1). The PNe membership could be claimed for any of them. The astrometric parameters estimated for the clusters were analyzed using Gaia DR2 through an algorithm developed by Angelo et al. (2019) and slightly modified in order to allow us to study clusters with very different density of stars (sec. 3.4.2). The algorithm works pretty well with proper motion and parallaxes via assigning higher membership probabilities to tighter stars in the astrometric parameter space. Using VVV data, we evaluated RDP and the statistically significance of the overdensities in order to identify if poorly dense areas could correspond to potential star clusters or possible density fluctuation of the star fields (sec. 3.4.1). VVV along with Gaia DR2 data also allowed us to establish photometric parameters for the clusters. We found that only two of the analyzed clusters showed to be real clusters, namely, Loden 467 and Stock 14, and that there is not enough evidence for reporting Loden 464, Loden 466, Lynga 15 and Bica 5 as clusters. We conclude that these are not real clusters, but possibly misidentifications due to random fluctuation of the stellar foreground and background. Additionally, just $5'$ from the Stock 14 lies the cluster candidate LS 007. Stars in the innermost part of the overdensity were shown to be potentially fitted with and very reddened isocrhone of E(B-V) = 3.2 and a distance d > 7 kpc. Fig. 5.4 shows that LS 007 reaches the field density in 1 arcmin, what would imply a minimum physical size of 2 pc. With respect to the PN membership, the potential associations between PN Hf 69 and the OCs lying in the FOV were assessed. Because Lynga 5 is an asterism the membership with this cluster is automatically rejected. On the other hand, the unique OC in the field able to claim the membership is Stock 14. Despite the large angular distance between the PN and this OC, the results of the RV, distances and reddening matched roughly with the planetary. This case is surely interesting and deserves further study.

Lynga 5 presented a distance dichotomy between photometric and astrometric measurements. Isochrone distances reported in literature for the cluster showed a closer distance than those determined by parallax in almost a factor of 2. This discrepancy was also found by us through both the VVV and the Gaia data. The discrepancy was resolved assuming a metallicity of $Z=10^{0.5}Z_{\odot}$ on the isochrone fit (Fig. 6.4), and the distance was finally established at $d=2.97^{3.38}_{2.69}$ kpc. The dichotomies did

Table 8.1: Parameters of the OCs obtained in this work.

Cluster	ϖ (mas)	μ_{α^*} (mas yr^{-1})	μ_δ (mas yr^{-1})	RV (km s^{-1})	d$_{BJ}$ kpc	d$_{Iso}$ kpc	E(B-V) (mag)	log(τ) (dex)
NGC 2453	—	-2.30±0.04	3.47±0.03	78±3	—	4.7	0.42±0.01	7.65
Stock 14	0.386±0.031	-6.290±0.162	0.761±0.148	—	$2.6^{3.0}_{2.3}$	2.1	0.26	7.4
LS007	—	—	—	—	—	>9.0	3.2	∼7.0
Loden 467	0.234±0.076	-6.457±0.444	1.069±0.332	—	$3.9^{7.5}_{2.9}$	3.7	0.9	8.8
Lynga 5	0.336±0.023	-3.625±0.130	-3.610±0.142	-56±18	$3.0^{3.4}_{2.7}$	2.8	1.12	8.4
IC 2488	0.751±0.028	-7.767±0.122	5.680±0.122	-3±2	$1.3^{1.4}_{1.3}$	1.33	0.28	8.1

Table 8.2: RVs and membership for the PNe studied in this work.

PN name	PN identifier	Cluster	PN RV (km s^{-1})	Membership
NGC 2452	G243.3-01.0	NGC 2453	62±2	Non member
Hf 69	G294.9-00.6	Lynga 15	-15±2	Non member
		Stock 14	-15±2	Possible
Hen 2-133	G324.8-01.1	Lynga 5	-23±2	Non member
NGC 2899	G277.1-03.8	IC 2488	-6±3	Likely
WRAY 17-31	G277.7-03.5	Basel 20	35±1	Non member
		IC 2488	35±1	Non member

not stop there. Distances reported in the literature for the PN Hen 2-133 are quite uncertain and they expand over a wide range (sec. 6.2). On the one hand, we have that reddening agrees with the PN being in the background of the OC Lynga 5, and on the other hand, the RV agrees with a foreground object. Both results could be conciliated if the PN suffered from heavy internal extinction. Giammanco et al. (2011) found fourteen nebulae whose reddenings exceed the maximum reddening measured along their line of sight by more than one magnitude. However, the deep difference between Hen 2-133 and Lynga 5 of about $\Delta E(B-V)$=1.28 would imply an extreme internal reddening > 1.28 mag. This discrepancy must be studied in future works. Nonetheless, our measure of the RV was very consistent in agreeing with the closer distances, and it disagrees with that for the cluster in ΔRV≈33 km s^{-1}. This implies that the membership must be ruled out.

Finally, the case of IC 2488 and NGC 2899 is very suggestive. The distance found in this work for the cluster matches perfectly with the reported for the PN, while the difference in reddening is small ΔE(B-V)≤0.2. Moreover, the RVs between both objects agree within 0.9σ. Both the morphology and spectrum suggest NGC 2899 is a Type I PN, with a massive progenitor. The turn-off mass for IC 2488 ($\approx 4M_\odot$) agrees with the PN. As discussed in section 7.1.1 the large angular separation has played an important role to dismiss the membership. Despite this we found

stars with the same astrometric and photometric solutions as the cluster at similar angular distances as the PN, suggesting a potential membership between the PN NGC 2899 and OC IC 2488. We conclude that NGC 2899 is a strong candidate to be member of the OC IC 2488.

8.2 Future Work

The search for PNe in star clusters is still far from complete. Table 1.1 shows at least a dozen of potential associations between PNe and OCs, and Table 1.3 four more for GCs. Many questions still remain unsolved about the PNe formation, and the evolution of stars in their last stages. PNe membership to stellar clusters would allow the theoretical models to be tested. Two cases draw our attention. The first one is the PN Sa 2-4 in the OC Berkeley 76. The pair is separated just by 2 arcmin. Berkeley 76 is an elusive cluster which distance is uncertain ranging between 2300-12600 pc with $\log(\tau)$ between $\sim$8.8 to $\sim$9.2 (Carraro et al., 2013; Kharchenko et al., 2016; Sampedro et al., 2017). However, no relevant information has been reported about the RVs required for assessing association of Sa 2-4 to the cluster. The second one is the pair PN PHR J1429-6043 in OC NGC 5617. PHR J1429-6043 is located within the core of the OC NGC 5617, separated only $1'$ from it. The OC is a widely studied, bright cluster. The average cluster distance is $\sim$2000 pc (see, for instance, Kharchenko et al., 2016; Sampedro et al., 2017; Cantat-Gaudin et al., 2018a), with a RV $\sim$-35 km/s (Wu et al., 2009; De Silva et al., 2015). On the contrary, PHR J1429-6043 is a faint circular nebula classified as a possible PN. More data is necessary to elucidate its nature.

On the other hand, the case of Stock 14 and PNe Hf 6 analyzed here deserves further research. New RV measurements are needed to establish a more accurate value for the cluster. The results of our work allow us to choose the most probable member stars both within and around the cluster core. With these measures it would be possible to assess the final membership of the PNe, studying its possible origin. This work was done using astrometric solution from *Gaia* DR2. However, while this thesis was being completed, the Gaia Early Data Release 3 (EDR3) was published. *Gaia* EDR3 has shown significant improvements in parallax and especially proper motion uncertainties (Lindegren et al., 2021). This surely will help to improve the precision in the determination of the clusters' parameters, and also the distances for those PNe with well identified central star (González-Santamaría et al., 2019).

Similarly with IC 2488 and NGC 2899. Although the results obtained here show the PN as a strong candidate to be a cluster member, a more accurate measure of the RV of the PN is mandatory to finally confirm the membership. This would be

possible to achieve with high resolution spectra of both the PN and stars marked as red points in left panel in Fig. 7.3. IC 2488 is very interesting because besides of the two PNe studied here, there are two additional PNe at its vicinity, namely, PHR J0930-5716 and WRAY 16-49. Both objects have been poorly studied, and they lie 30′ and 45′ from IC 2488, respectively. Spectral data for these PNe are also required.

Bibliography

A. Acker. A new synthetic distance scale for planetary nebulae. *Astronomy and Astrophysics Supplement Series*, 33:367–381, 1978.

J. Alonso-Santiago, I. Negueruela, A. Marco, H. M. Tabernero, C. González-Fernández, and N. Castro. Ngc 6067: a young and massive open cluster with high metallicity. *Monthly Notices of the Royal Astronomical Society*, 469(2): 1330–1353, 2017.

D. R. Alves, H. E. Bond, and M. Livio. Hubble space telescope observations of the planetary nebula k648 in the globular cluster m15. *The Astronomical Journal*, 120(4):2044, 2000.

M. Angelo, J. Santos, W. Corradi, and F. Maia. Investigating dynamical properties of evolved galactic open clusters. *Astronomy & Astrophysics*, 624:A8, 2019.

F. Arenou, X. Luri, C. Babusiaux, C. Fabricius, A. Helmi, T. Muraveva, A. Robin, F. Spoto, A. Vallenari, T. Antoja, et al. Gaia data release 2-catalogue validation. *Astronomy & Astrophysics*, 616:A17, 2018a.

F. Arenou, X. Luri, C. Babusiaux, C. Fabricius, A. Helmi, T. Muraveva, A. Robin, F. Spoto, A. Vallenari, T. Antoja, et al. Gaia data release 2-catalogue validation. *Astronomy & Astrophysics*, 616:A17, 2018b.

T. L. Astraatmadja and C. A. Bailer-Jones. Estimating distances from parallaxes. iii. distances of two million stars in the gaia dr1 catalogue. *The Astrophysical Journal*, 833(1):119, 2016.

C. Badenes, D. Maoz, and R. Ciardullo. The progenitors and lifetimes of planetary nebulae. *The Astrophysical Journal Letters*, 804(1):L25, 2015.

C. A. Bailer-Jones. Estimating distances from parallaxes. *Publications of the Astronomical Society of the Pacific*, 127(956):994, 2015.

R. Barbá, A. Roman-Lopes, J. N. Castellón, V. Firpo, D. Minniti, P. Lucas, J. Emerson, M. Hempel, M. Soto, and R. Saito. Hundreds of new cluster candidates in the vista variables in the vía láctea survey dr1. *Astronomy & Astrophysics*, 581:A120, 2015.

H. Barker, A. Zijlstra, O. De Marco, D. J. Frew, J. E. Drew, R. L. Corradi, J. Eislöffel, and Q. A. Parker. The binary fraction of planetary nebula central stars-iii. the promise of vphas+. *Monthly Notices of the Royal Astronomical Society*, 475 (4):4504–4523, 2018.

N. Bastian and S. De Mink. The effect of stellar rotation on colour–magnitude diagrams: on the apparent presence of multiple populations in intermediate age stellar clusters. *Monthly Notices of the Royal Astronomical Society: Letters*, 398 (1):L11–L15, 2009.

H. Baumgardt, M. Hilker, A. Sollima, and A. Bellini. Mean proper motions, space orbits, and velocity dispersion profiles of galactic globular clusters derived from gaia dr2 data. *Monthly Notices of the Royal Astronomical Society*, 482(4):5138–5155, 2019.

G. F. Benedict, B. E. McArthur, R. Napiwotzki, T. E. Harrison, H. C. Harris, E. Nelan, H. E. Bond, R. J. Patterson, and R. Ciardullo. Astrometry with the hubble space telescope: Trigonometric parallaxes of planetary nebula nuclei ngc 6853, ngc 7293, abell 31, and deht 5. *The Astronomical Journal*, 138(6):1969, 2009.

P. Bergeron, R. A. Saffer, and J. Liebert. A spectroscopic determination of the mass distribution of da white dwarfs. *The Astrophysical Journal*, 394:228–247, 1992.

M. M. M. Bertolami. New models for the evolution of post-asymptotic giant branch stars and central stars of planetary nebulae. *Astronomy & Astrophysics*, 588:A25, 2016.

S. Bhattacharya, M. Arnaboldi, J. Hartke, O. Gerhard, V. Comte, A. McConnachie, and N. Caldwell. The survey of planetary nebulae in andromeda (m 31)-i. imaging the disc and halo with megacam at the cfht. *Astronomy & Astrophysics*, 624: A132, 2019.

L. Bianchi, R. Bohlin, G. Catanzaro, H. Ford, and A. Manchado. Hubble space telescope and ground-based spectroscopy of k648 in m15. *The Astronomical Journal*, 122(3):1538, 2001.

C. M. Bidin, S. Villanova, G. Piotto, and Y. Momany. A lack of close binaries among hot horizontal branch stars in globular clusters-ii. ngc 2808. *Astronomy & Astrophysics*, 528:A127, 2011.

H. M. Boffin and D. Jones. *The Importance of Binaries in the Formation and Evolution of Planetary Nebulae*. Springer, 2019.

C. Bonatto, E. Bica, S. Ortolani, and B. Barbuy. Detection of ks-excess stars in the 14 myr open cluster ngc 4755. *Astronomy & Astrophysics*, 453(1):121–132, 2006.

C. Bonatto, E. Bica, and J. F. Santos Jr. Discovery of an open cluster with a possible physical association with a planetary nebula. *Monthly Notices of the Royal Astronomical Society*, 386(1):324–336, 2008.

H. E. Bond. Hubble space telescope snapshot search for planetary nebulae in globular clusters of the local group. *The Astronomical Journal*, 149(4):132, 2015.

D. Bossini, A. Vallenari, A. Bragaglia, T. Cantat-Gaudin, R. Sordo, L. Balaguer-Núñez, C. Jordi, A. Moitinho, C. Soubiran, L. Casamiquela, et al. Age determination for 269 gaia dr2 open clusters. *Astronomy & Astrophysics*, 623:A108, 2019.

J. Brand and L. Blitz. The velocity field of the outer galaxy. *Astronomy and Astrophysics*, 275:67, 1993.

A. Brown, A. Vallenari, T. Prusti, J. De Bruijne, C. Babusiaux, C. Bailer-Jones, M. Biermann, D. W. Evans, L. Eyer, F. Jansen, et al. Gaia data release 2-summary of the contents and survey properties. *Astronomy & astrophysics*, 616: A1, 2018.

J. Buell, R. Henry, E. Baron, and K. Kwitter. On the origin of planetary nebula k648 in globular cluster m15. *The Astrophysical Journal*, 483(2):837, 1997.

J. Cahn, J. Kaler, and L. Stanghellini. A catalogue of absolute fluxes and distances of planetary nebulae. *Astronomy and Astrophysics Supplement Series*, 94:399–452, 1992.

W. Campbell and J. Moore. The spectrographic velocities of the bright-line nebulae. *Publications of Lick Observatory*, 13:75–186, 1918.

T. Cantat-Gaudin, C. Jordi, A. Vallenari, A. Bragaglia, L. Balaguer-Núñez, C. Soubiran, D. Bossini, A. Moitinho, A. Castro-Ginard, A. Krone-Martins, et al. A gaia dr2 view of the open cluster population in the milky way. *Astronomy & Astrophysics*, 618:A93, 2018a.

T. Cantat-Gaudin, C. Jordi, A. Vallenari, A. Bragaglia, L. Balaguer-Núñez, C. Soubiran, D. Bossini, A. Moitinho, A. Castro-Ginard, A. Krone-Martins, et al. A gaia dr2 view of the open cluster population in the milky way. *Astronomy & Astrophysics*, 618:A93, 2018b.

G. Carraro, R. A. Vázquez, A. Moitinho, and G. Baume. Detection of a young stellar population in the background of open clusters in the third galactic quadrant. *The Astrophysical Journal*, 630(2):L153–L156, aug 2005. doi: 10.1086/491787. URL `https://doi.org/10.1086%2F491787`.

G. Carraro, Y. Beletsky, and G. Marconi. Five old open clusters more in the outer galactic disc. *Monthly Notices of the Royal Astronomical Society*, 428(1):502–517, 2013.

G. Carraro, A. F. Seleznev, G. Baume, and D. G. Turner. The complex stellar populations in the background of open clusters in the third galactic quadrant. *Monthly Notices of the Royal Astronomical Society*, 455(4):4031–4045, 2015.

J. O. Cazetta and W. J. Maciel. Distances of galactic planetary nebulae based on a relationship between the central star mass and the n/o abundance. *Revista Mexicana de Astronomía y Astrofísica*, 36:3–11, 2000.

A.-N. Chené, J. Borissova, J. Clarke, C. Bonatto, D. J. Majaess, C. M. Bidin, S. E. Sale, F. Mauro, R. Kurtev, G. Baume, et al. Massive open star clusters using the vvv survey-i. presentation of the data and description of the approach. *Astronomy & Astrophysics*, 545:A54, 2012.

N. Chornay and N. Walton. Searching for central stars of planetary nebulae in gaia dr2. *Astronomy & Astrophysics*, 638:A103, 2020a.

N. Chornay and N. Walton. Searching for central stars of planetary nebulae in gaia dr2. *Astronomy & Astrophysics*, 638:A103, 2020b.

N. Chornay, N. Walton, D. Jones, H. Boffin, M. Rejkuba, and R. Wesson. Towards a more complete sample of binary central stars of planetary nebulae with gaia. *Astronomy & Astrophysics*, 648:A95, 2021.

C. Chubak, G. Marcy, D. A. Fischer, A. W. Howard, H. Isaacson, J. A. Johnson, and J. T. Wright. Precise radial velocities of 2046 nearby fgkm stars and 131 standards. *arXiv preprint arXiv:1207.6212*, 2012.

R. Ciardullo and H. E. Bond. A survey for pulsations in o vi nuclei of planetary nebulae. *The Astronomical Journal*, 111:2332, 1996.

R. Ciardullo, H. E. Bond, M. S. Sipior, L. K. Fullton, C.-Y. Zhang, and K. G. Schaefer. A hubble space telescope survey for resolved companions of planetary nebula nuclei. *The Astronomical Journal*, 118(1):488, 1999.

R. Ciardullo, S. Sigurdsson, J. J. Feldmeier, and G. H. Jacoby. Close binaries as the progenitors of the brightest planetary nebulae. *The Astrophysical Journal*, 629(1):499, 2005.

J. Clariá, A. Piatti, E. Lapasset, and J.-C. Mermilliod. Multicolour photometry and coravel observations of stars in the southern open cluster ic 2488. *Astronomy & Astrophysics*, 399(2):543–551, 2003.

P. R. T. Coelho. A new library of theoretical stellar spectra with scaled-solar and α-enhanced mixtures. *Monthly Notices of the Royal Astronomical Society*, 440 (2):1027–1043, 2014.

J. Cohen and F. Gillett. The peculiar planetary nebula in m22. *The Astrophysical Journal*, 346:803–807, 1989.

M. Cohen, Q. A. Parker, and J. Chapman. A circular planetary nebula around the oh/ir star oh 354.88–0.54 (v1018 sco). *Monthly Notices of the Royal Astronomical Society*, 357(4):1189–1196, 2005.

C. Conrad, R.-D. Scholz, N. Kharchenko, A. Piskunov, S. Röser, E. Schilbach, R. De Jong, O. Schnurr, M. Steinmetz, E. Grebel, et al. A rave investigation on galactic open clusters-ii. open cluster pairs, groups and complexes. *Astronomy & Astrophysics*, 600:A106, 2017.

H. D. Curtis. Descriptions of 762 nebulae and clusters photographed with the crossley reflector. *Publications of Lick Observatory*, 13:9–42, 1918.

S. Daflon, K. Cunha, F. X. De Araujo, S. Wolff, and N. Przybilla. The projected rotational velocity distribution of a sample of ob stars from a calibration based on synthetic he i lines. *The Astronomical Journal*, 134(4):1570, 2007.

V. M. Danilov, S. I. Putkov, and A. F. Seleznev. Dynamics of the coronas of open star clusters. *Astronomy Reports*, 58(12):906–921, Dec. 2014. doi: 10.1134/S1063772914120038.

C. Daub. A statistical survey of local planetary nebulae. *The Astrophysical Journal*, 260:612–624, 1982.

B. D. Davis, H. E. Bond, R. Ciardullo, and G. H. Jacoby. Hubble space telescope spectroscopy of a planetary nebula in an m31 open cluster: Hot-bottom burning at 3.4 $m_{\odot}$. *The Astrophysical Journal*, 884(2):115, 2019.

R. de la Fuente Marcos, C. de la Fuente Marcos, C. Moni Bidin, G. Carraro, and E. Costa. Ngc 1252: a high altitude, metal poor open cluster remnant. *Monthly Notices of the Royal Astronomical Society*, 434(1):194–208, 2013.

O. De Marco. Binary central stars. *Proceedings of the International Astronomical Union*, 2(S234):111–118, 2006.

O. De Marco. The origin and shaping of planetary nebulae: putting the binary hypothesis to the test. *Publications of the Astronomical Society of the Pacific*, 121(878):316, 2009.

G. De Silva, G. Carraro, V. D'Orazi, V. Efremova, H. Macpherson, S. Martell, and L. Rizzo. Binary open clusters in the milky way: photometric and spectroscopic analysis of ngc 5617 and trumpler 22. *Monthly Notices of the Royal Astronomical Society*, 453(1):106–112, 2015.

L. Decin. Evolution and mass loss of cool aging stars: A daedalean story. *Annual Review of Astronomy and Astrophysics*, 59, 2021.

X. Delfosse, C. Kahane, and T. Forveille. Superwind in evolved oh/ir stars. *Astronomy and Astrophysics*, 320:249–256, 1997.

W. Dias, B. Alessi, A. Moitinho, and J. Lépine. New catalogue of optically visible open clusters and candidates. *Astronomy & Astrophysics*, 389(3):871–873, 2002.

W. S. Dias, H. Monteiro, J. R. D. Lépine, R. Prates, C. D. Gneiding, and M. Sacchi. Astrometric and photometric study of Dias 4, Dias 6, and other five open clusters using ground-based and Gaia DR2 data. *Monthly Notices of the Royal Astronomical Society*, 481(3):3887–3901, Dec. 2018. doi: 10.1093/mnras/sty2341.

Dias, W. S., Monteiro, H., Caetano, T. C., Lépine, J. R. D., Assafin, M., and Oliveira, A. F. Proper motions of the optically visible open clusters based on the ucac4 catalog. *A&A*, 564:A79, 2014. doi: 10.1051/0004-6361/201323226. URL `https://doi.org/10.1051/0004-6361/201323226`.

S. Dib, S. Schmeja, and R. J. Parker. Structure and mass segregation in galactic stellar clusters. *Monthly Notices of the Royal Astronomical Society*, 473(1):849–859, 2018.

D. Douchin, O. De Marco, D. Frew, G. Jacoby, G. Jasniewicz, M. Fitzgerald, J.-C. Passy, D. Harmer, T. Hillwig, and M. Moe. The binary fraction of planetary nebula central stars–ii. a larger sample and improved technique for the infrared excess search. *Monthly Notices of the Royal Astronomical Society*, 448(4):3132–3155, 2015.

S. Durand, A. Acker, and A. Zijlstra. The kinematics of 867 galactic planetary nebulae. *Astronomy and Astrophysics Supplement Series*, 132(1):13–20, 1998.

C. M. Dutra, B. X. Santiago, and E. Bica. Low-extinction windows in the inner galactic bulge. *Astronomy & Astrophysics*, 381(1):219–226, 2002.

G. M. Eadie and W. E. Harris. Bayesian mass estimates of the milky way: the dark and light sides of parameter assumptions. *The Astrophysical Journal*, 829 (2):108, 2016.

J. Emerson and W. Sutherland. The visible and infrared survey telescope for astronomy (vista): Looking back at commissioning. *The Messenger*, 139:2–5, 2010.

V. Fragkou, Q. Parker, A. Zijlstra, L. Crause, and H. Barker. A high-mass planetary nebula in a galactic open cluster. *Nature Astronomy*, 3(9):851–857, 2019.

D. J. Frew. *Planetary Nebulae in the Solar Neighbourhood: Statistics, Distance Scale and Luminosity Function*. PhD thesis, Macquarie University NSW 2109, Australia, 2008.

D. J. Frew, I. S. Bojičić, and Q. A. Parker. The hα surface brightness — radius plane as a diagnostic tool for photoionized nebulae. *Journal of Physics: Conference Series*, 728:032015, jul 2016.

G. García-Segura, N. Langer, M. Różyczka, and J. Franco. Shaping bipolar and elliptical planetary nebulae: effects of stellar rotation, photoionization heating, and magnetic fields. *The Astrophysical Journal*, 517(2):767, 1999.

G. García-Segura, J. A. López, and J. Franco. Magnetically driven winds from post-asymptotic giant branch stars: solutions for high-speed winds and extreme collimation. *The Astrophysical Journal*, 618(2):919, 2005.

R. Gathier. Vbluw-photometry of stars in small fields around 13 planetary nebulae. *Astronomy and Astrophysics Supplement Series*, 60:399–423, 1985.

R. Gathier, S. Pottasch, and J. Pel. Distances to planetary nebulae. i-the reddening-distance method. *Astronomy and Astrophysics*, 157:171–190, 1986.

C. Giammanco, S. E. Sale, R. L. Corradi, M. J. Barlow, K. Viironen, L. Sabin, M. Santander-García, D. J. Frew, R. Greimel, B. Miszalski, et al. Iphas extinction distances to planetary nebulae. *Astronomy & Astrophysics*, 525:A58, 2011.

F. Gillett, G. Neugebauer, J. Emerson, and W. Rice. Iras 18333-2357-an unusual source in m22. *The Astrophysical Journal*, 300:722–728, 1986.

E. Glushkova, M. Zabolotskikh, A. Rastorguev, I. Uglova, and A. Fedorova. Absolute proper motions of 181 young open clusters. *Astronomy Letters*, 23:71–78, 1997.

D. González-Díaz, C. M. Bidin, E. Silva-Villa, G. Carraro, D. Majaess, A. Moitinho, C. Orquera-Rojas, C. M. Marín, and E. Morales-Campaña. Solving the distance discrepancy for the open cluster ngc 2453-the planetary nebula ngc 2452 is not a cluster member. *Astronomy & Astrophysics*, 626:A10, 2019.

I. González-Santamaría, M. Manteiga, A. Manchado, A. Ulla, and C. Dafonte. Properties of central stars of planetary nebulae with distances in gaia dr2. *Astronomy & Astrophysics*, 630:A150, 2019.

G. M. Green, E. F. Schlafly, D. P. Finkbeiner, M. Jurić, H.-W. Rix, W. Burgett, K. C. Chambers, P. W. Draper, H. Flewelling, R. P. Kudritzki, et al. Measuring distances and reddenings for a billion stars: Toward a 3d dust map from pan-starrs 1. *The Astrophysical Journal*, 783(2):114, 2014.

G. M. Green, E. F. Schlafly, D. Finkbeiner, H.-W. Rix, N. Martin, W. Burgett, N. Metcalfe, P. W. Draper, C. Waters, E. A. Magnier, H. Flewelling, J. L. Tonry, K. Hodapp, N. Kaiser, R. Wainscoat, and R.-P. Kudritzki. Galactic reddening in 3D from stellar photometry – an improved map. *Monthly Notices of the Royal Astronomical Society*, 478(1):651–666, 06 2018. ISSN 0035-8711. doi: 10.1093/mnras/sty1008. URL `https://doi.org/10.1093/mnras/sty1008`.

W. Greig. The morphological classification of symmetrical nebulae. *Astronomy and Astrophysics*, 10:161–174, 1971.

H. C. Harris, C. C. Dahn, B. Canzian, H. H. Guetter, S. Leggett, S. E. Levine, C. B. Luginbuhl, A. K. Monet, D. G. Monet, J. R. Pier, et al. Trigonometric parallaxes of central stars of planetary nebulae. *The Astronomical Journal*, 133 (2):631, 2007.

P. Hasan, G. Kilambi, and S. Hasan. Evolutionary studies of the young star clusters: Ngc 1960, ngc 2453 and ngc 2384. *Astrophysics and Space Science*, 313(4):363–371, 2008.

M. Hempel, D. Minniti, I. Dékány, R. Saito, P. Lucas, J. Emerson, A. Ahumada, S. Aigrain, M. Alonso, J. Alonso-García, et al. Vista variables in the vía láctea (vvv): Halfway status and results. *ESO Messenger 155,(2014), 29-32*, 2014.

T. C. Hillwig, D. Jones, O. De Marco, H. E. Bond, S. Margheim, and D. Frew. Observational confirmation of a link between common envelope binary interaction and planetary nebula shaping. *The Astrophysical Journal*, 832(2):125, 2016.

K. Horne. An optimal extraction algorithm for ccd spectroscopy. *Publications of the Astronomical Society of the Pacific*, 98(604):609, 1986.

I. Iben Jr. Planetary nebulae and their central stars—origin and evolution. *Physics Reports*, 250(1-2):1–94, 1995.

M. J. Irwin, J. Lewis, S. Hodgkin, P. Bunclark, D. Evans, R. McMahon, J. P. Emerson, M. Stewart, and S. Beard. VISTA data flow system: pipeline processing for WFCAM and VISTA. In P. J. Quinn and A. Bridger, editors, *Optimizing Scientific Return for Astronomy through Information Technologies*, volume 5493 of *Society of Photo-Optical Instrumentation Engineers (SPIE) Conference Series*, pages 411–422, Sept. 2004. doi: 10.1117/12.551449.

G. H. Jacoby, J. A. Morse, L. K. Fullton, K. Kwitter, and R. Henry. Planetary nebulae in the globular cluster pal 6 and ngc 6441. *The Astronomical Journal*, 114:2611, 1997.

G. H. Jacoby, O. De Marco, J. Davies, I. Lotarevich, H. E. Bond, J. P. Harrington, and T. Lanz. Masses of the planetary nebula central stars in the galactic globular cluster system from hst imaging and spectroscopy. *The Astrophysical Journal*, 836(1):93, 2017.

D. Jones and H. M. Boffin. Binary stars as the key to understanding planetary nebulae. *Nature Astronomy*, 1(5):1–6, 2017.

Y. C. Joshi, A. Dambis, A. K. Pandey, and S. Joshi. Study of open clusters within 1.8 kpc and understanding the galactic structure. *Astronomy & Astrophysics*, 593:A116, 2016.

J. B. Kaler, R. A. Shaw, and K. B. Kwitter. Large planetary nebulae and their significance to the late stages of stellar evolution. *The Astrophysical Journal*, 359:392–418, 1990.

J. S. Kalirai, D. S. Davis, H. B. Richer, P. Bergeron, M. Catelan, B. M. Hansen, and R. M. Rich. The masses of population ii white dwarfs. *The Astrophysical Journal*, 705(1):408, 2009.

N. Kharchenko, R.-D. Scholz, A. Piskunov, S. Röser, and E. Schilbach. Astrophysical supplements to the ascc-2.5: Ia. radial velocities of 55000 stars and mean radial velocities of 516 galactic open clusters and associations, 2007.

N. Kharchenko, A. Piskunov, E. Schilbach, S. Röser, and R.-D. Scholz. Global survey of star clusters in the milky way-ii. the catalogue of basic parameters. *Astronomy & Astrophysics*, 558:A53, 2013.

N. Kharchenko, A. Piskunov, E. Schilbach, S. Röser, and R.-D. Scholz. Global survey of star clusters in the milky way-v. integrated jhks magnitudes and luminosity functions. *Astronomy & Astrophysics*, 585:A101, 2016.

P. Kholopov. The unity in the structure of star clusters. *Soviet Astronomy*, 12:625, 1969.

G. Khromov. Distances and galactic distribution of planetary nebulae. *Astrophysics*, 15(2):179–187, 1979.

S. Kimeswenger and D. Barría. Planetary nebula distances in gaia dr2. *Astronomy & Astrophysics*, 616:L2, 2018.

R. L. Kingsburgh and M. Barlow. Elemental abundances for a sample of southern galactic planetary nebulae. *Monthly Notices of the Royal Astronomical Society*, 271:257–299, 1994.

L. L. Kiss, G. M. Szabó, Z. Balog, Q. A. Parker, and D. J. Frew. Aaomega radial velocities rule out current membership of the planetary nebula ngc 2438 in the open cluster m46. *Monthly Notices of the Royal Astronomical Society*, 391(1): 399–404, 2008.

L. Kohoutek. Version 2000 of the catalogue of galactic planetary nebulae. *Astronomy & Astrophysics*, 378(3):843–846, 2001.

J. Köppen and A. Acker. Planetary nebulae in clusters. In *Massive Stellar Clusters*, volume 211, page 151, 2000.

P. Kroupa. Unification of the nearby and photometric stellar luminosity functions. *The Astrophysical Journal*, 453, 1995.

R. Kurucz. ATLAS9 Stellar Atmosphere Programs and 2 km/s grid. *ATLAS9 Stellar Atmosphere Programs and 2 km/s grid. Kurucz CD-ROM No. 13. Cambridge, Mass.: Smithsonian Astrophysical Observatory, 1993.*, 13, 1993.

S. Kwok. *The origin and evolution of planetary nebulae.* Cambridge University Press, 2007a.

S. Kwok. *The origin and evolution of planetary nebulae*. Cambridge University Press, 2007b.

S. Larsen and T. Richtler. Planetary nebula candidates in extragalactic young star clusters. *Astronomy & Astrophysics*, 459(1):103–111, 2006.

L. Lindegren, J. Hernández, A. Bombrun, S. Klioner, U. Bastian, M. Ramos-Lerate, A. De Torres, H. Steidelmüller, C. Stephenson, D. Hobbs, et al. Gaia data release 2-the astrometric solution. *Astronomy & astrophysics*, 616:A2, 2018.

L. Lindegren, S. Klioner, J. Hernández, A. Bombrun, M. Ramos-Lerate, H. Steidelmüller, U. Bastian, M. Biermann, A. de Torres, E. Gerlach, et al. Gaia early data release 3-the astrometric solution. *Astronomy & Astrophysics*, 649:A2, 2021.

L. Liu and X. Pang. A catalog of newly identified star clusters in gaia dr2. *The Astrophysical Journal Supplement Series*, 245(2):32, 2019.

L. Lodén. A list of suspected clusters in the southern milky way. *Astronomy and Astrophysics Supplement Series*, 10:125, 1973.

A. Loktin and M. Popova. Updated version of the 'homogeneous catalog of open cluster parameters'. *Astrophysical Bulletin*, 72(3):257–265, 2017.

J. Lopez, L. Falcon, M. Ruiz, and M. Roth. The evolved bipolar planetary nebula ngc 2899. *Astronomy and Astrophysics*, 241:526–536, 1991.

X. Luri, A. Brown, L. Sarro, F. Arenou, C. Bailer-Jones, A. Castro-Ginard, J. de Bruijne, T. Prusti, C. Babusiaux, and H. Delgado. Gaia data release 2-using gaia parallaxes. *Astronomy & Astrophysics*, 616:A9, 2018.

W. Maciel. A catalogue of distances of planetary nebulae. *Astronomy and Astrophysics Supplement Series*, 55:253–258, 1984.

W. Maciel and S. Pottasch. Distances of planetary nebulae. *Astronomy and Astrophysics*, 88:1–7, 1980.

F. Maia, W. Corradi, and J. Santos. Characterization and photometric membership of the open cluster ngc 1981. *Monthly Notices of the Royal Astronomical Society*, 407(3):1875–1886, 2010.

D. Majaess, D. Turner, C. M. Bidin, D. Geisler, J. Borissova, D. Minniti, C. Bonatto, W. Gieren, G. Carraro, R. Kurtev, et al. Strengthening the open cluster distance scale via vvv photometry. *Astronomy & Astrophysics*, 537:L4, 2012a.

D. Majaess, D. Turner, C. M. Bidin, D. Geisler, J. Borissova, D. Minniti, C. Bonatto, W. Gieren, G. Carraro, R. Kurtev, et al. Strengthening the open cluster distance scale via vvv photometry. *Astronomy & Astrophysics*, 537:L4, 2012b.

D. Majaess, G. Carraro, C. M. Bidin, C. Bonatto, D. Turner, M. Moyano, L. Berdnikov, and E. Giorgi. On the crucial cluster andrews-lindsay 1 and a 4% distance solution for its planetary nebula. *Astronomy & Astrophysics*, 567:A1, 2014.

D. J. Majaess, D. G. Turner, and D. J. Lane. In search of possible associations between planetary nebulae and open clusters. *Publications of the Astronomical Society of the Pacific*, 119(862):1349, 2007.

D. J. Majaess, D. G. Turner, and D. J. Lane. Assessing potential cluster cepheids from a new distance and reddening parametrization and two micron all sky survey photometry. *Monthly Notices of the Royal Astronomical Society*, 390(4):1539–1548, 2008.

D. Mallik, R. Sagar, and A. Pati. A deep bvi photometric study of the open cluster ngc 2453. *Astronomy and Astrophysics Supplement Series*, 114:537–548, 1995.

A. Manchado, L. Stanghellini, and M. A. Guerrero. Quadrupolar planetary nebulae: A new morphological class. *The Astrophysical Journal Letters*, 466(2):L95, 1996.

P. Marigo, L. Girardi, A. Bressan, P. Rosenfield, B. Aringer, Y. Chen, M. Dussin, A. Nanni, G. Pastorelli, T. S. Rodrigues, et al. A new generation of parsec-colibri stellar isochrones including the tp-agb phase. *The Astrophysical Journal*, 835(1): 77, 2017.

D. J. Marshall, A. Robin, C. Reylé, M. Schultheis, and S. Picaud. Modelling the galactic interstellar extinction distribution in three dimensions. *Astronomy & Astrophysics*, 453(2):635–651, 2006.

F. Mauro, C. Moni Bidin, A.-N. Chené, D. Geisler, J. Alonso-García, J. Borissova, and G. Carraro. The vvv-skz_pipeline: an automatic psf-fitting photometric pipeline for the vvv survey. *Revista mexicana de astronomía y astrofísica*, 49(2): 189–207, 2013.

W. McCrea. Extended main-sequence of some stellar clusters. *Monthly Notices of the Royal Astronomical Society*, 128(2):147–155, 1964.

S. J. Meatheringham, P. Wood, and D. Faulkner. A study of some southern planetary nebulae. *The Astrophysical Journal*, 334:862–874, 1988.

A. M. Meisner and D. P. Finkbeiner. A full-sky, high-resolution atlas of galactic 12 μm dust emission with wise. *The Astrophysical Journal*, 781(1):5, 2013.

A. Mel'nik, P. Rautiainen, L. Berdnikov, A. Dambis, and A. Rastorguev. Classical cepheids in the galactic outer ring r1r2. *Astronomische Nachrichten*, 336(1): 70–83, 2015.

J. Mermilliod, M. Mayor, and S. Udry. Red giants in open clusters-xiv. mean radial velocities for 1309 stars and 166 open clusters. *Astronomy & Astrophysics*, 485 (1):303–314, 2008.

J.-C. Mermilliod, J. Clariá, J. Andersen, A. Piatti, and M. Mayor. Red giants in open clusters-ix. ngc 2324, 2818, 3960 and 6259. *Astronomy & Astrophysics*, 375 (1):30–39, 2001.

D. Minniti. Abundances and velocities for open and globular cluster giants: The data. *Astronomy and Astrophysics Supplement Series*, 113:299, 1995.

D. Minniti and M. Rejkuba. Extragalactic globular cluster planetary nebulae: Discovery of a planetary nebula in the ngc 5128 globular cluster g169 using the magellan i baade telescope. *The Astrophysical Journal Letters*, 575(2):L59, 2002.

D. Minniti, P. Lucas, J. Emerson, R. Saito, M. Hempel, P. Pietrukowicz, A. Ahumada, M. Alonso, J. Alonso-Garcia, J. I. Arias, et al. Vista variables in the via lactea (vvv): The public eso near-ir variability survey of the milky way. *New Astronomy*, 15(5):433–443, 2010.

D. Minniti, B. Dias, M. Gómez, T. Palma, and J. B. Pullen. New candidate planetary nebulae in galactic globular clusters from the vvv survey. *The Astrophysical Journal Letters*, 884(1):L15, 2019.

Minniti, Dante, Fernández-Trincado, José G., Gómez, Matías, Smith, Leigh C., Lucas, Philip W., and Contreras Ramos, Rodrigo. Discovery of a new nearby globular cluster with extreme kinematics located in the extension of a halo stream. *A&A*, 650:L11, 2021. doi: 10.1051/0004-6361/202141129. URL `https://doi.org/10.1051/0004-6361/202141129`.

A. Moffat and M. Fitzgerald. Ngc 2453, a moderately young open cluster in puppis. *Astronomy and Astrophysics Supplement Series*, 18:19, 1974.

A. Moitinho. Open clusters in the third galactic quadrant-i. photometry. *Astronomy & Astrophysics*, 370(2):436–446, 2001.

A. Moitinho, R. A. Vázquez, G. Carraro, G. Baume, E. Giorgi, and W. Lyra. Spiral structure of the third galactic quadrant and the solution to the canis major debate. *Monthly Notices of the Royal Astronomical Society: Letters*, 368 (1):L77–L81, 2006.

C. Moni Bidin, D. Majaess, C. Bonatto, F. Mauro, D. Turner, D. Geisler, A.-N. Chené, A. C. Gormaz-Matamala, J. Borissova, R. G. Kurtev, et al. Investigating potential planetary nebula/cluster pairs. *Astronomy & Astrophysics*, 561:A119, 2014.

C. Moni Bidin, D. Casetti-Dinescu, T. Girard, L. Zhang, R. Méndez, K. Vieira, V. Korchagin, and W. van Altena. Young stars in the periphery of the large magellanic cloud. *Monthly Notices of the Royal Astronomical Society*, 466(3): 3077–3087, 2017.

J. A. Morse, R. D. Mathieu, and S. E. Levine. The measurement of precise radial velocities of early type stars. *The Astronomical Journal*, 101:1495–1510, 1991.

R. Napiwotzki, P. J. Green, and R. A. Saffer. A comparative study of the mass distribution of extreme-ultraviolet-selected white dwarfs. *The Astrophysical Journal*, 517(1):399, 1999.

T. Neckel and G. Klare. The spatial distribution of the interstellar extinction. *Astronomy and Astrophysics Supplement Series*, 42:251–281, 1980.

J. Nordhaus, E. Blackman, and A. Frank. Isolated versus common envelope dynamos in planetary nebula progenitors. *Monthly Notices of the Royal Astronomical Society*, 376(2):599–608, 2007.

Q. A. Parker, D. J. Frew, B. Miszalski, A. V. Kovacevic, P. M. Frinchaboy, P. D. Dobbie, and J. Köppen. Phr 1315- 6555: a bipolar planetary nebula in the compact hyades-age open cluster eso 96-sc04. *Monthly Notices of the Royal Astronomical Society*, 413(3):1835–1844, 2011.

Q. A. Parker, I. S. Bojičić, and D. J. Frew. Hash: the hong kong/aao/strasbourg hα planetary nebula database. In *Journal of Physics: Conference Series*, volume 728, page 032008. IOP Publishing, 2016.

J.-C. Passy, O. De Marco, C. L. Fryer, F. Herwig, S. Diehl, J. S. Oishi, M.-M. Mac Low, G. L. Bryan, and G. Rockefeller. Simulating the common envelope phase of a red giant using smoothed-particle hydrodynamics and uniform-grid codes. *The Astrophysical Journal*, 744(1):52, 2011a.

J.-C. Passy, O. De Marco, C. L. Fryer, F. Herwig, S. Diehl, J. S. Oishi, M.-M. Mac Low, G. L. Bryan, and G. Rockefeller. Simulating the common envelope phase of a red giant using smoothed-particle hydrodynamics and uniform-grid codes. *The Astrophysical Journal*, 744(1):52, 2011b.

D. B. Pavani, L. O. Kerber, E. Bica, and W. J. Maciel. Diagnostic tool to analyse colour-magnitude diagrams of poorly populated stellar concentrations. *Monthly Notices of the Royal Astronomical Society*, 412(3):1611–1626, Apr. 2011. doi: 10.1111/j.1365-2966.2010.17999.x.

F. Pease. A planetary nebula in the globular cluster messier 15. *Publications of the Astronomical Society of the Pacific*, 40:342–342, 1928.

M. Pedreros. Photometric study of the southern open cluster ic 2488. *The Astronomical Journal*, 94:92–98, 1987.

M. Pedreros. The open cluster ngc 2818 and its associated planetary nebula. *The Astronomical Journal*, 98:2146–2155, 1989.

M. Peimbert. Chemical abundances in planetary nebulae. In *Symposium-International Astronomical Union*, volume 76, pages 215–224. Cambridge University Press, 1978.

M. Pena, M. Ruiz, P. Bergeron, S. Torres-Peimbert, and S. Heathcote. The evolved central star of the planetary nebula eso 166-pn 21. *Astronomy and Astrophysics*, 317:911–918, 1997.

G. Perren, E. Giorgi, A. Moitinho, G. Carraro, M. Pera, and R. Vázquez. Sixteen overlooked open clusters in the fourth galactic quadrant-a combined analysis of ubvi photometry and gaia dr2 with asteca. *Astronomy & Astrophysics*, 637:A95, 2020.

D. Peton-Jonas. A study of galactic structure in a region of puppis. *Astronomy and Astrophysics Supplement Series*, 45:193–205, 1981.

J. Phillips. Planetary nebula distances re-examined: an improved statistical scale. *Monthly Notices of the Royal Astronomical Society*, 353(2):589–600, 2004a.

J. Phillips. Planetary nebula distances re-examined: an improved statistical scale. *Monthly Notices of the Royal Astronomical Society*, 353(2):589–600, 2004b.

A. Piskunov, E. Schilbach, N. Kharchenko, S. Röser, and R.-D. Scholz. Tidal radii and masses of open clusters. *Astronomy & Astrophysics*, 477(1):165–172, 2008.

G. Rieke and M. Lebofsky. The interstellar extinction law from 1 to 13 microns. *The Astrophysical Journal*, 288:618–621, 1985.

S. Roeser, M. Demleitner, and E. Schilbach. The ppmxl catalog of positions and proper motions on the icrs. combining usno-b1. 0 and the two micron all sky survey (2mass). *The Astronomical Journal*, 139(6):2440, 2010.

R. A. Saffer, P. Bergeron, D. Koester, and J. Liebert. Atmospheric parameters of field subdwarf b stars. *The Astrophysical Journal*, 432:351–366, 1994.

R. K. Saito, M. Hempel, D. Minniti, P. W. Lucas, M. Rejkuba, I. Toledo, O. Gonzalez, J. Alonso-García, M. J. Irwin, E. Gonzalez-Solares, et al. Vvv dr1: The first data release of the milky way bulge and southern plane from the near-infrared eso public survey vista variables in the vía láctea. *Astronomy & Astrophysics*, 537:A107, 2012.

L. Sampedro, W. Dias, E. J. Alfaro, H. Monteiro, and A. Molino. A multimembership catalogue for 1876 open clusters using ucac4 data. *Monthly Notices of the Royal Astronomical Society*, 470(4):3937–3945, 2017.

E. L. Sandquist, R. E. Taam, X. Chen, P. Bodenheimer, and A. Burkert. Double core evolution. x. through the envelope ejection phase. *The Astrophysical Journal*, 500(2):909, 1998.

E. F. Schlafly and D. P. Finkbeiner. Measuring reddening with sloan digital sky survey stellar spectra and recalibrating sfd. *The Astrophysical Journal*, 737(2): 103, 2011.

D. J. Schlegel, D. P. Finkbeiner, and M. Davis. Maps of dust infrared emission for use in estimation of reddening and cosmic microwave background radiation foregrounds. *The Astrophysical Journal*, 500(2):525, 1998.

D. Schönberner. Late stages of stellar evolution. ii-mass loss and the transition of asymptotic giant branch stars into hot remnants. *The Astrophysical Journal*, 272:708–714, 1983.

D. Schönberner and T. Blöcker. Structure and evolution of central stars of planetary nebulae. *Astrophysics and Space Science*, 245(2):201–217, 1996.

D. Schönberner and J. Drilling. On the ultraviolet iron spectrum of pre-white dwarfs. *The Astrophysical Journal*, 290:L49–L53, 1985.

R. Schönrich, J. Binney, and W. Dehnen. Local kinematics and the local standard of rest. *Monthly Notices of the Royal Astronomical Society*, 403(4):1829–1833, 2010.

W. Seggewiss. Photoelectric observations of stars in the southern open clusters. ngc 2335, 2343, 2453, 4439 and h5. *Veroeffentlichungen des Astronomisches Institute der Universitaet Bonn*, 83, 1971.

R. Sharples. A complete sample of globular clusters in ngc 5128. In *Symposium-International Astronomical Union*, volume 126, pages 545–546. Cambridge University Press, 1988.

R. Silvotti, C. Bartolini, and L. Stanghellini. Search for new pulsating o vi central stars of planetary nebulae. *arXiv preprint astro-ph/9506046*, 1995.

M. Skrutskie, R. Cutri, R. Stiening, M. Weinberg, S. Schneider, J. Carpenter, C. Beichman, R. Capps, T. Chester, J. Elias, et al. The two micron all sky survey (2mass). *The Astronomical Journal*, 131(2):1163, 2006.

H. Smith Jr. On the distances of planetary nebulae. *Monthly Notices of the Royal Astronomical Society*, 449(3):2980–3005, 2015.

N. Soker. Why magnetic fields cannot be the main agent shaping planetary nebulae. *Publications of the Astronomical Society of the Pacific*, 118(840):260, 2006.

M. Soto, R. Barbá, G. Gunthardt, D. Minniti, P. Lucas, D. Majaess, M. Irwin, J. Emerson, E. Gonzalez-Solares, M. Hempel, et al. Milky way demographics with the vvv survey-ii. color transformations and near-infrared photometry for 136 million stars in the southern galactic disk. *Astronomy & Astrophysics*, 552: A101, 2013.

C. Soubiran, T. Cantat-Gaudin, M. Romero-Gómez, L. Casamiquela, C. Jordi, A. Vallenari, T. Antoja, L. Balaguer-Núñez, D. Bossini, A. Bragaglia, et al. Open cluster kinematics with gaia dr2. *Astronomy & Astrophysics*, 619:A155, 2018.

L. Stanghellini and M. Haywood. The galactic structure and chemical evolution traced by the population of planetary nebulae. *The Astrophysical Journal*, 714 (2):1096, 2010.

L. Stanghellini, R. L. Corradi, and H. E. Schwarz. The correlations between planetary nebula morphology and central star evolution. *Astronomy and astrophysics*, 279:521–528, 1993.

L. Stanghellini, R. A. Shaw, and E. Villaver. The magellanic cloud calibration of the galactic planetary nebula distance scale. *The Astrophysical Journal*, 689(1): 194, 2008.

P. B. Stetson, L. E. Davis, and D. R. Crabtree. Future development of the DAOPHOT crowded-field photometry package. In G. H. Jacoby, editor, *CCDs in astronomy*, volume 8 of *Astronomical Society of the Pacific Conference Series*, pages 289–304, 1990.

A. Tajitsu and S. Tamura. A new distance indicator to galactic planetary nebulae based upon iras fluxes. *The Astronomical Journal*, 115(5):1989, 1998.

W. Tifft, L. Conolly, and D. Webb. Ngc 2818, an open cluster containing a planetary nebula. *Monthly Notices of the Royal Astronomical Society*, 158(1):47–62, 1972.

J. Tonry and M. Davis. A survey of galaxy redshifts. i-data reduction techniques. *The Astronomical Journal*, 84:1511–1525, 1979.

L. Topaktas and R. Fenkart. Photographic rgu photometry of five southern open clusters in vela ii. *Astronomy and Astrophysics Supplement Series*, 49:475–482, 1982.

D. Turner. Cluster membership of the cepheid uy persei. *Publications of the Astronomical Society of the Pacific*, 89(529):277, 1977.

D. G. Turner. The color-magnitude diagram of ngc 2264. *Astronomische Nachrichten*, 333(2):174–181, 2012.

D. G. Turner and J. F. Burke. The distance scale for classical cepheid variables. *The Astronomical Journal*, 124(5):2931, 2002.

D. G. Turner and M. Pedreros. A photometric investigation of cluster membership for the cepheid bb sagittarii. 1985.

D. G. Turner, D. J. Majaess, and D. D. Balam. Testing new ideas regarding the nature of interstellar extinction. *Canadian Journal of Physics*, 92(12):1696–1702, 2014.

R. Tylenda, A. Acker, B. Stenholm, and J. Koeppen. The extinction constants for galactic planetary nebulae. *Astronomy and Astrophysics Supplement Series*, 95: 337–354, 1992.

I. Usenko, A. Y. Kniazev, I. Y. Katkov, V. V. Kovtyukh, T. Mishenina, A. Miroshnichenko, and D. Turner. Spectroscopic investigations of galactic clusters with associated cepheid variables. iii. collinder 394 and bb sgr. 2019.

S. Vásquez, I. Saviane, E. V. Held, G. Da Costa, B. Dias, M. Gullieuszik, B. Barbuy, S. Ortolani, and M. Zoccali. Homogeneous metallicities and radial velocities for galactic globular clusters-ii. new cat metallicities for 28 distant and reddened globular clusters. *Astronomy & Astrophysics*, 619:A13, 2018.

R. Vázquez. Bubbles and knots in the kinematical structure of the bipolar planetary nebula ngc 2818. *The Astrophysical Journal*, 751(2):116, 2012.

R. A. Vazquez, J. May, G. Carraro, L. Bronfman, A. Moitinho, and G. Baume. Spiral structure in the outer galactic disk. i. the third galactic quadrant. *The Astrophysical Journal*, 672(2):930–939, jan 2008. doi: 10.1086/524003. URL `https://doi.org/10.1086%2F524003`.

M. J. Veyette, B. F. Williams, J. J. Dalcanton, B. Balick, N. Caldwell, M. Fouesneau, L. Girardi, K. D. Gordon, J. Kalirai, P. Rosenfield, et al. Panchromatic hubble andromeda treasury. ix. a photometric survey of planetary nebulae in m31. *The Astrophysical Journal*, 792(2):121, 2014.

A. Wachter, K.-P. Schröder, J. Winters, T. Arndt, and E. Sedlmayr. An improved mass-loss description for dust-driven superwinds and tip-agb evolution models. *Astronomy & Astrophysics*, 384(2):452–459, 2002.

W. A. Weidmann, R. Gamen, P. Van Hoof, A. Zijlstra, D. Minniti, and M. G. Volpe. Near-infrared photometry of galactic planetary nebulae with the vvv survey. *Astronomy & Astrophysics*, 552:A74, 2013.

R. E. Wilson. *General catalogue of stellar radial velocities*, volume 601. Carnegie Institution of Washington Washington, 1953.

Z.-Y. Wu, X. Zhou, J. Ma, and C.-H. Du. The orbits of open clusters in the galaxy. *Monthly Notices of the Royal Astronomical Society*, 399(4):2146–2164, 2009.

W. Yang, X. Meng, S. Bi, Z. Tian, T. Li, and K. Liu. The contributions of interactive binary stars to double main-sequence turnoffs and dual red clump of intermediate-age star clusters. *The Astrophysical Journal Letters*, 731(2):L37, 2011.

C. Zhang. A statistical distance scale for galactic planetary nebulae. *The Astrophysical Journal Supplement Series*, 98:659–678, 1995a.

C. Zhang. A statistical distance scale for galactic planetary nebulae. *The Astrophysical Journal Supplement Series*, 98:659–678, 1995b.

L. Zhang, C. M. Bidin, D. I. Casetti-Dinescu, R. A. Méndez, T. M. Girard, V. I. Korchagin, K. Vieira, W. F. Van Altena, and G. Zhao. Chemical composition of young stars in the leading arm of the magellanic system. *The Astrophysical Journal*, 835(2):285, 2017.

A. A. Zijlstra. Binary central stars of planetary nebulae. *Baltic Astronomy*, 16: 79–86, 2007.

A. A. Zijlstra, P. te Lintel Hekkert, S. R. Pottasch, J. Caswell, M. Ratag, and H. J. Habing. Oh maser emission from young planetary nebulae. *Astronomy and Astrophysics*, 217:157–178, 1989.

Colophon

This thesis is based on a template developed by Matthew Townson and Andrew Reeves. It was typeset with LaTeX 2_ε. It was created using the *memoir* package, maintained by Lars Madsen, with the *madsen* chapter style. The font used is Latin Modern, derived from fonts designed by Donald E. Kunith.